IntechOpen

Fractal Analysis

Edited by Sid-Ali Ouadfeul

Fractal Analysis

Edited by Sid-Ali Ouadfeul

IntechOpen

Supporting open minds since 2005

We are IntechOpen,
the world's leading publisher of
Open Access books
Built by scientists, for scientists

4,100+

Open access books available

116,000+

International authors and editors

120M+

Downloads

151

Countries delivered to

Our authors are among the

Top 1%

most cited scientists

12.2%

Contributors from top 500 universities

Interested in publishing with us?
Contact book.department@intechopen.com

Numbers displayed above are based on latest data collected.
For more information visit www.intechopen.com

Meet the editor

Dr. Sid-Ali Ouadfeul is currently an Associate Professor of geophysics at Khemis Miliana University. He received an Engineer diploma from the University of Boumerdes, Algeria, a Magister and PhD in Geophysics from the University of Sciences and Technology, Houari Boumedienne, Algeria. During these last two decades, Dr. Ouadfeul has published many papers to understand the earth's underlying system using nonlinear analysis such as the artificial intelligence and fractal analysis. Dr. Ouadfeul is the organizer of many international conferences throughout the world on the understanding of chaotic systems in geophysics.

Contents

Preface

Fractal analysis has proven its ability to resolve many problems and ambiguities in the full spectrum of sciences such as physics, chemistry, human biology, and geosciences. The aim of this book is to show some applications of fractal analysis in the fields of sciences authored by Dr. Sid-Ali Ouadfeul, an Associate Professor of geophysics at Khemis Miliana University. The first chapter introduces the readers to the book, while the second chapter shows the methods and challenges of fractal analysis of time-series data sets. The third chapter demonstrates fractal geometry as an attractive choice for miniaturized planar microwave filter design. The fourth chapter presents fractal antennas for wearable applications. The objective of the fifth chapter is to show some Parrondian games in discrete dynamic systems, while the last chapter reveals fractal structures of carbon nanotube system arrays.

Sid-Ali Ouadfeul
University of Khemis Miliana,
Algeria

Introductory Chapter: Fractal in Sciences

Sid-Ali Ouadfeul

1. Introduction

The notion of fractal was introduced for the first time in 1975 by the mathematician Benoit Mandelbrot in his book entitled *Fractal Objects* which marked the beginning of his fame. The first definitions of the adjective fractal (from the Latin adjective fractus) come from the word "frangere" which means to break.

The irregularities of nature, of chaotic appearance, such as the irregularities of the seacoasts and the shape of the clouds, a tree, and a fern leaf, are in fact the expression of a very complex geometry of the sea. 'infinitely small. It can be said, however, that a fractal object is an invariant object by dilations, translations, and rotations [1].

The fractal analysis has been widely used in sciences, for example, in physics, the fractal analysis is used in thermodynamics, particularly for the study of fully developed turbulence [1], in image segmentation and processing [2, 3], in astrophysics for the study of hydrogen distribution [4], in physical medicine for tumor localization from mammograms [3], and in cardiology, for the study of the electrocardiograms [5].

In geoscience, the fractal analysis has been used in petrophysics for the segmentation or classification of geological formations [6–9]. It has also been used in geomagnetism to characterize the outer part of the geomagnetic field [10–14]. In environmental sciences, Burrough [15] used the semivariogram method to estimate the fractal dimension D for various environmental transects (e.g., soil factors, vegetation cover, iron ore content in rocks, rainfall levels, crop yields). In medicine and human biology, the fractal analysis has been applied in cell, protein, and chromosome structures, for example, Takahashi [16] supposed that the basic design of a chromosome has a tree-like pattern. Xu et al. [17] assumed that the twistings of DNA-binding proteins have fractal properties. Self-similarity has recently demonstrated in DNA sequences (see Stanley [18]; see also papers in Nonnenmacher et al. [19]). Glazier et al. [20] used the multifractal spectrum approach to rebuild the evolutionary history of organisms from mDNA sequences.

The aim of this book is to gather advance researches in the field of fractal analysis; the book contains seven chapters: one chapter is discussing the Parrondian games in discrete dynamic systems, two chapters are debating the application of the fractal analysis in microwave and antennas, and another chapter is showing some applications in medicine, while another one is talking about the fractal structures of the carbon nanotube system arrays and another chapter discuss the methods and challenges of the fractal analysis of the time-series data sets.

Author details

Sid-Ali Ouadfeul
University of Khemis Miliana, Algeria

*Address all correspondence to: souadfeul@ymail.com

IntechOpen

References

[1] Arneodo A, Bacry E. Ondelettes, multifractal et turbulence de l'ADN aux croissances cristallines. Paris New York, Amsterdam: Diderot éditeur arts et sciences; 1995

[2] Arneodo A, Decoster N, Kestener P, Roux SG. A wavelet-based method for multi- fractal image analysis: From theoretical concepts to experimental applications. Advances in Imaging and Electron Physics. 2003;**126**:1-92

[3] Kestener P. Analyse multifractale 2D et 3D à l'aide de la transformée en ondelettes: Application en mammographie et en turbelence déveleoppée [Thèse de doctorat]. Université de paris sud; 2003

[4] Saritha C, Sukanya, Narasimha Murthy Y. ECG signal analysis using wavelet transforms. Bulgarian Journal de Physique. 2008;**35**:68-77

[5] Khalil A, Joncas G, Nekka F, Kestener P, Arneodo A. Morphological analysis of HI features. II. Wavelet-based multifractal formalism. Astrophysical Journal. 2008;**165**:512-550

[6] Ouadfeul S. Automatic lithofacies segmentation using the Wavelet Transform Modulus Maxima lines (WTMM) combined with the Detrended Fluctuation Analysis(DFA). In: 17th International Geophysical Congress and Exhibition of Turkey; 2006

[7] Ouadfeul S, Zaourar N, Boudella A, Hamoudi M. Modeling and classification of lithofacies using the continuous wavelet transform and neural network: A case study from the Berkine Basin (Algeria). Bulletin du service géologique National-Algérie. 2011;**22**:n°1

[8] Pilkington M, Tudoeschuck JP. Naturally smooth inversions with a priori information from well logs. Geophysics. 1991;**56**:1811-1818

[9] Pilkington M, Tudoeschuck JP. Stochastic inversion for scaling geology. Geophysical Journal International. 1990;**102**:205-217

[10] Sridharan M, Rarnasamy AMS. Multidimensional scaling technique for analysis of magnetic storms at Indian observatories. Proceedings of the Indian Academy of Sciences—Earth & Planetary Sciences. 2002;**111**(4):459-465

[11] Sridharan M, Ramasamy AMS. Fractal analysis for geomagnetic secular variations. Journal of Indian Geophysical Union. 2006;**10**(3);175-185

[12] Kabin K, Papitashvili VO. Fractal properties of the IMF and the Earth's magnetotail field. Earth, Planets and Space. 1998;**50**(1):87-90

[13] Lakhina GS. Solar wind-magnetosphere-ionosphere coupling and chaotic dynamics. Surveys in Geophysics Netherland: Kluwer Academic Publishers. 1994;**15**:703-754

[14] Warden PE. Nonlinear Phenomena and Chaos in Magnetic Materials. Singapore: Worod Scientific Pub.Co.1993. p. p141

[15] Burrough PA. Fractal dimensions of landscapes and other environmental data. Nature. 1981;**294**:240-242

[16] Takahashi M. A fractal model of chromosomes and chromosomal DNA replication. Journal of Theoretical Biology. 1989;**141**:117-136

[17] Xu J, Chao Y, Chen R. Fractal geometry study of DNA binding proteins. Journal of Theoretical Biology. 1994;**171**:239-249

[18] Stanley HE. Fractal landscapes in physics and biology. Physica A. 1992;**186**:1-32

[19] Nonnenmacher TF, Losa GA, Weibel ER. Fractals in Biology and Medicine. Cambridge: Birkhäuser; 1994

[20] Glazier JA, Raghavachari S, Berthlesen CL, Skolnick MH. Reconstructing phylogeny from the multifractal spectrum of mitochondrial DNA. Physical Review E. 1995;**51**:2665-2668

Chapter 2

Fractal Analysis of Time-Series Data Sets: Methods and Challenges

Ian Pilgrim and Richard P. Taylor

Abstract

Many methods exist for quantifying the fractal characteristics of a structure via a fractal dimension. As a traditional example, a fractal dimension of a spatial fractal structure may be quantified via a box-counting fractal analysis that probes a manner in which the structure fills space. However, such spatial analyses generally are not well-suited for the analysis of so-called "time-series" fractals, which may exhibit exact or statistical self-affinity but which inherently lack well-defined spatial characteristics. In this chapter, we introduce and investigate a variety of fractal analysis techniques directed to time-series structures. We investigate the fidelity of such techniques by applying each technique to sets of computer-generated time-series data sets with well-defined fractal characteristics. Additionally, we investigate the inherent challenges in quantifying fractal characteristics (and indeed of verifying the presence of such fractal characteristics) in time-series traces modeled to resemble physical data sets.

Keywords: fractal, spatial fractal, time-series fractal, fractal analysis, fractal dimension, self-similarity, self-affinity, topological dimension, embedding dimension, similarity dimension, box-counting dimension, covering dimension, variational box-counting, Hurst exponent, variance method, Dubuc variation method, adaptive fractal analysis, power-law noise, Brownian motion, fractional Brownian motion

1. Introduction

In this chapter, we explore a species of fractals known as "time-series" fractals. Such structures generally may be conceived (and visualized) as functions of independent variables whose plots exhibit shapes and patterns that are evocative of the more familiar spatial fractals. However, lacking well-defined spatial characteristics, time-series fractals call for analytical tools that depart from those of the world of spatial fractals. To lay the foundation for a discussion of such analytical tools, we begin with an overview of fractal structures and traditional fractal analysis techniques. We then introduce time-series fractals and investigate the unique analytical tools necessitated by such structures. Finally, we investigate the relative fidelity of these analytical tools, as well as the shortcomings inherent in performing fractal analysis on time-series fractals of limited length and/or fine-scale detail.

2. Motivating the fractal dimension

Mathematician Benoit B. Mandelbrot often is credited with introducing the notion of a fractional, or fractal, dimension in his 1967 paper, "How long is the coast of Britain?" [1]. In fact, however, the curious nature of coastline measurements had been discussed by Lewis Fry Richardson 6 years prior in the *General Systems Yearbook* [2]. Richardson, a pacifist and mathematician, sought to investigate the hypothesis that the likelihood that war would erupt between a pair of neighboring nations is related to the length of the nations' shared border. As Richardson and Mandelbrot note, such a hypothesis is difficult to evaluate, since individual records of the length of Britain's west coast varied by up to a factor of three. Indeed, as the precision of such measurements increases—that is, by decreasing the length of the "ruler" used to trace the profile—the measured total length appears to increase as well. This quality reflects the fact that the outline of the British coastline is an example of a "self-similar" structure—that is, a structure that exhibits the same statistical qualities, or even the exact details, across a wide range of length scales. In light of this apparent fundamental indeterminacy, Mandelbrot posits that familiar geometrical metrics such as length are inadequate for describing the complexity found in nature.

Recognizing Richardson's prior investigations, Mandelbrot notes that Richardson had indeed produced an empirical relation between a measured coast length L and the smallest unit of measurement G: $L(G) = MG^{1-D}$, where M is a positive constant and $D \geq 1$—but observes that "unfortunately it attracted no attention" [1]. In Ref. [1], building upon Richardson's observations, Mandelbrot introduces the formalism of a fractional, or fractal[1], dimension to quantify the nature of such shapes.

Following Mandelbrot's example, to generalize the concept of a geometrical dimension, we may begin by examining the scaling behavior of such trivially self-similar objects as a line, a square, and a cube. For example, consider a line segment of length L, which can be separated into N non-overlapping subsets of length L/N, each of which is identical to the whole segment but for a scaling factor $r(N) = 1/N$. Analogously, a square with side length L may be decomposed into N^2 facsimiles of side length L/N, each of which is scaled down from the original by a factor $r(N) = N^{-1/2}$, and a cube of side length L can be decomposed into N^3 facsimiles of side length L/N with corresponding scaling ratio $r(N) = N^{-1/3}$; see **Figure 1**. To generalize this pattern, we may observe that the scaling ratio $r(N)$ follows the relationship $r(N) = N^{-1/D}$. In this relationship, $D = -\log(N)/\log(r(N))$ is known as the *similarity dimension* of the structure in question.

Applying the concept of a similarity dimension to less trivial shapes is straightforward in the case of exactly self-similar structures, such as structures that are constructed via iteration of a generating pattern. As an example, consider the Koch curve, illustrated in **Figure 2**. The Koch curve is constructed as follows: Beginning with a line segment of unity length, replace the middle third of the segment with an equilateral triangle whose base has a length of 1/3 and overlies the original line segment, then remove this overlapping base segment. The resulting figure thus consists of four line segments, each of which has a length of 1/3. Iterating this process for each new line segment yields a sequence of figures that exhibit increasingly fine structure, with the limiting state of this series exhibiting exact self-similarity, in the sense that a nontrivial subset of the shape is exactly identical to the

---

[1] Though Mandelbrot discusses the concept of fractional dimension in this 1967 paper, he did not introduce the term "fractal" until 1975 [3].
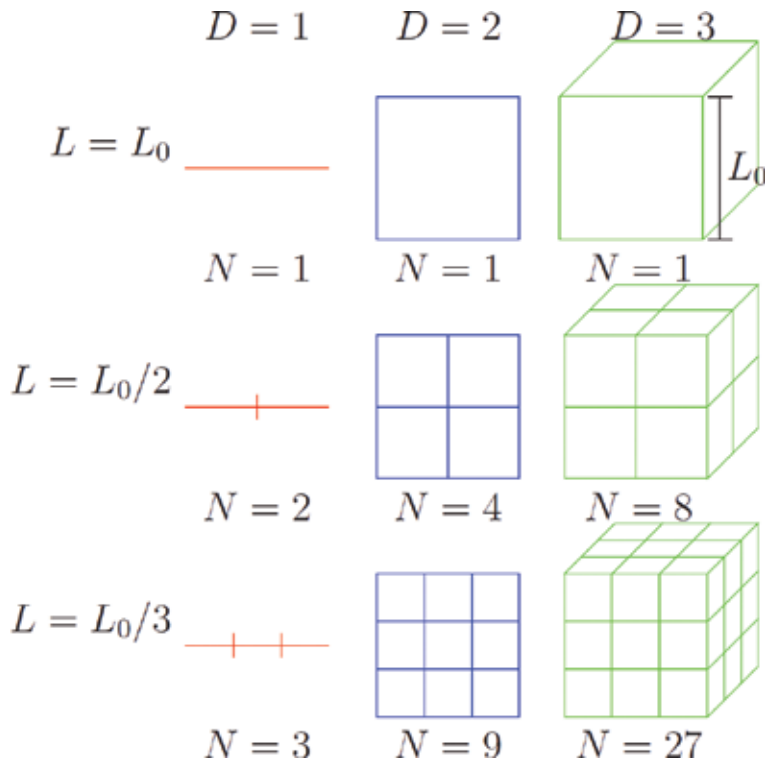
Figure 1.
A line, a square, and a cube are examples of trivially self-similar Euclidian shapes. A Euclidian shape in D dimensions may be said to contain $N = (L/L_0)^{-D}$ exact copies of itself scaled by a factor of L/L_0. Image provided by R.D. Montgomery.
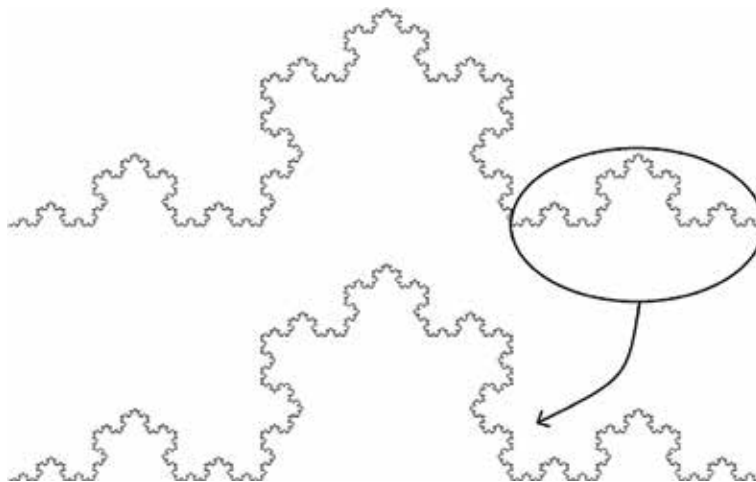
Figure 2.
The Koch curve is an example of an exact self-similar figure with a non-integer similarity dimension.

whole. This exact self-similarity is illustrated in **Figure 2**, which shows that the full Koch curve may be described as being formed from four exact copies of itself, each scaled down by a factor of 1/3. Thus, we can apply the above relation to find that the Koch curve has a similarity dimension of $D = -\log(4)/\log(1/3) \approx 1.26$.

The similarity dimension described above represents but one example of a plurality of dimensions that can be defined and calculated for a given figure.

Indeed, the utility of the similarity dimension is limited by the fact that it applies only to figures that exhibit exact self-similarity; by contrast, the complexity witnessed in natural systems such as coastlines generally exhibits self-similarity only in the statistical sense. As an example, **Figure 3** illustrates a structure that exhibits statistical self-similarity. Specifically, **Figure 3** illustrates an example of a modified Koch curve formed by randomizing the orientations of the line segments as the structure is generated.

As a tool for quantifying the nature of such fractal structures that do not exhibit exact self-similarity, we now turn to the (roughly self-explanatory) "box-counting dimension," also known as the "covering dimension." Given a structure that extends in two dimensions[2], the box-counting dimension may be determined as follows: First, superimpose a square grid with individual boxes of size $\ell \times \ell$ over the figure in question, and count the number of boxes $N(\ell)$ within which some portion of the figure in question is present (see **Figure 4**). Next, repeat this procedure while varying the box size ℓ and construct a plot of $\log(N(\ell))$ vs $\log(1/\ell)$; for a self-similar structure, the data should follow a linear trend with a gradient equal to the box-counting dimension D. Such a plot is generally known as a scaling plot.

The box-counting method also may be described in more geometrically intuitive terms. For example, and as shown in **Figure 4**, one may observe that the set of all occupied boxes at a given length scale ℓ collectively serves as an approximation of the total structure as "observed" at the length scale ℓ. Stated differently, the set of $\ell \times \ell$ boxes that overlap some portion of the base structure may be seen as representing a snapshot of the base structure as viewed at a resolution corresponding to the length ℓ. In general, however, the set of boxes covering the base structure cannot be expected to represent the geometric details of the structure at any length scale. For example, as shown in **Figure 4**, is evident that the incompatibility of the straight edges of the square boxes and the jagged boundary of the Koch curve leads to a markedly crude representation of the structure at all length scales, as each occupied box will always contain details that cannot be fully represented by that box.

While the box-counting method of estimating fractal dimension is conceptually straightforward, some care must be taken to preserve the utility of the method. For example, one must select an appropriate range of box sizes ℓ over which to examine the scaling trend, given that any observed fractal scaling trend will not persist over all possible length scales. That is, for any finite structure, it is possible to encompass the structure in a box of size $L \times L$, for an appropriate value of L. In such a case, applying the box-counting method with boxes of size $\ell \geq L$ will always return a
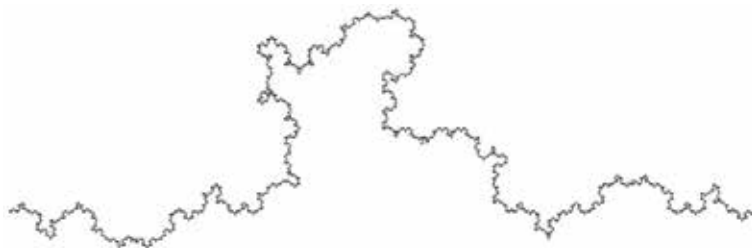
Figure 3.
Introducing randomness into the generating algorithm of the Koch curve produces a statistically self-similar fractal structure.

---

[2] While the box-counting method is typically applied to structures embedded in two dimensions, it is straightforward to generalize the technique to higher- or lower-dimensional systems.
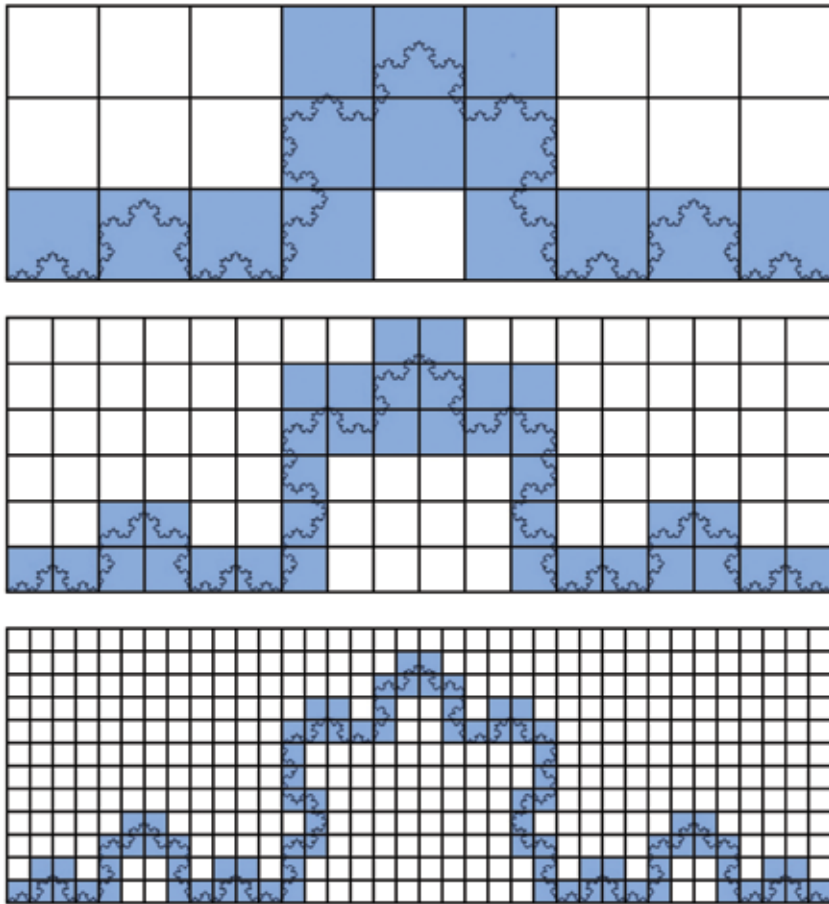
Figure 4.
Applying the box-counting method to the Koch curve. The number of boxes of side length ℓ occupied by some portion of the curve follows $N(\ell) \propto \ell^{-D}$, where D is the box-counting dimension of the curve.

value $N(\ell) = 1$—only one box can be filled when the box size contains the entire structure—thus resulting in an apparent fractal dimension of zero. As another example, when considering a range of box sizes $\ell \lesssim L$, nearly all such boxes will be counted as filled, and the box count $N(\ell)$ will scale as the square of the inverse box size $1/\ell$. In this case, the box-counting method will return an apparent fractal dimension of $D = 2$, and we may say that the pattern "looks two-dimensional" when examined at this coarse scale. When dealing with patterns found in nature, the opposite extreme of possible length scales merits consideration as well. For a mathematically-generated fractal figure, such as a figure that exhibits structure at arbitrarily fine length scales, the box-counting method may be applied with arbitrarily small box sizes ℓ. However, naturally occurring fractal structures invariably exhibit a smallest length scale to which a scaling trend may extend. For example, while the scaling trend certainly must cease at the molecular and atomic scales, such fractal scaling behavior generally diverges at length scales many times larger than this. In such cases, applying the box-counting method at length scales ℓ smaller than a smallest feature size observed in the structure yields a number of filled boxes $N(\ell)$ that scales linearly with the inverse box size $1/\ell$; thus, the figure "looks one-dimensional" to the box-counting analysis at these scales.

Such conditions necessitate careful determination of the appropriate range of length scales over which to assess fractal scaling behavior. This determination may

be made empirically, such as by observing the range of length scales over which the scaling plot is sufficiently linear. Alternatively, this determination may be made by convention, such as may be based on statistical arguments. In practice, it is generally not known *a priori* whether a structure under consideration should even be expected to *be* a fractal, and hence whether it should be expected to produce a scaling plot with a linear trend between cutoffs defined by appropriate physical and/or measurement limitations. Accordingly, it is preferred to adopt conventions with some degree of universality and that do not presuppose the existence of the fractal scaling behavior under investigation. More specifically, it is common to adopt the following conventions, noting that the ranges may be bounded by physical and/or measurement limitations. The coarse-scale analysis cutoff generally corresponds to a limit of the range of length scales measured, which in turn generally is related to the coarse-scale size of the structure itself. This limit is conventionally set at $\ell = L/5$, where L is the side length of the smallest square that may circumscribe the structure, thus guaranteeing that the grid includes no fewer than 25 boxes. Turning to the fine scale, the physical limit is determined by the smallest (nontrivial) feature size that is observed in the structure, while the fine-scale measurement limit is conventionally chosen to satisfy the requirement that each box contains no fewer than five data points. In practice, the more restrictive of these two limits is chosen (i.e., the larger of the physical fine-scale limit and the fine-scale measurement limit).

As a further consideration in optimizing the performance of the box-counting method, one must select the position and orientation of the box grid relative to the structure in question. To the extent that the box-counting method seeks to probe an inherent quality of a structure, the observed fractal dimension should not be affected by a spatial translation or rotation of the grid with respect to the structure, since the structure itself has no preferred orientation. However, consider the case shown in **Figure 5**, in which the box-counting method is applied to a fractal profile. In the box-counting scheme discussed above, all boxes that contain any portion of the structure under examination are counted toward the total; applying this to the structure of **Figure 5**, we find that 35 boxes are filled using this box size ℓ. Suppose, however, that one is able to reposition the boxes semi-independently of one another, by translating a set of adjacent $\ell \times \ell$ boxes within each column of width ℓ. Doing so, we find that a careful repositioning of the boxes within these columns
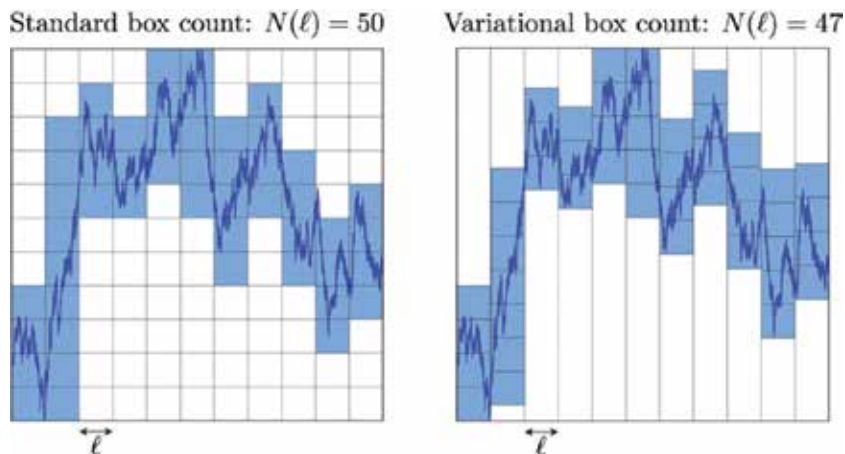

Figure 5.
An example of applying the variational box-counting method. When the boxes are constrained in a grid (left), we find a box count $N(\ell) = 50$; however, when the $\ell \times \ell$ boxes are allowed to shift vertically within columns of width ℓ (right), the measured box count $N(\ell)$ drops to 47.

results in the box count $N(\ell)$ dropping to 29. This apparent inconsistency serves to motivate a refinement of the box-counting analysis as described above. Specifically, the "variational box-counting method" includes shifting the boxes in columns as described above so as to minimize the number of $\ell \times \ell$ boxes needed to entirely cover the figure in question. The variational box-counting method thus serves to eliminate some of the apparent ambiguity of the traditional box-counting method. Of course, some ambiguity still remains in this amended method, given that the rotational orientation of the columns relative to the examined structure remains arbitrary. To eliminate this residual ambiguity, one may repeat the above-described variational method at a variety of rotational orientations of the grid with respect to the figure and choose the angle that minimizes $N(\ell)$ for each value of ℓ. However, in practical applications, incorporating this additional variation does not significantly affect the measured dimensions.

3. Time-series fractal structures

The fractal structures discussed above generally represent examples of spatial fractal structures—that is, structures with spatial extent and whose fractal characteristics are embodied in their spatial form. However, many observable structures and phenomena exhibit fractal behavior while lacking spatial form. Another important class of structures to which fractal analysis may be directed is that of "time-series" structures—that is, structures that may be represented as a single-valued function of a single independent variable. As suggested by their name, a time-series structure may refer to some variable quantity—say, stock market prices, or atmospheric pressure—that fluctuates in time, but for the purposes of this work we intend for the term to refer to any data set or plot consisting of a dependent variable that may be represented as a single-valued function of an independent variable.

As with the spatial structures considered above, a time-series structure may exhibit fractal scaling properties in either a statistical or an exact sense, which may be quantified using the formalism of fractal dimensions. Unfortunately, the box-counting methods described above for measuring a fractal dimension are ill-suited to time-series structures. Simply put, this limitation arises from the fact that box-counting methods assess the fractal dimension of shapes that extend in space, while the spatial "shape" of a time-series structure is inherently undefined. That is, since the two axes of a plot representing a time-series data set generally represent variables with distinct units, the geometric aspect ratio of such a plot is fundamentally undefined.

As an example, consider the data set displayed in **Figure 6**, which plots the daily closing price of a certain technology stock over a period of roughly 16 years. Specifically, **Figure 6** illustrates three representations of the same data set, with the respective y-axis of each illustration scaled by a distinct factor. In qualitative terms, one may be tempted to conclude that the data in the top panel appear the most linear and that the data in the bottom panel appear the most space-filling. Accordingly, given that a box-counting fractal analysis technique essentially assesses the space-filling properties of a structure, applying a box-counting analysis to each plot would yield distinct results for each plot.

The difficulty here lies in the fact that a box-counting fractal analysis necessarily treats a figure as a spatial entity whose orthogonal dimensions have the same units. By contrast, a time-series trace such as the one displayed in **Figure 6** lacks this property, but may still exhibit fractal characteristics in the form of either statistical or exact self-affinity. As discussed above, exact and statistical self-similarity describe structures whose precise details or statistical properties (respectively) are

Figure 6.
Daily closing prices for a single stock from December 1980 to October 1996. Each of the three plots displays the same data, but the y-axis of each plot is scaled by a distinct factor. A box-counting fractal analysis would return unique results for each plot, despite each plot representing the same data set.

repeated as its orthogonal dimensions are rescaled by a similar factor. By contrast, exact and statistical self-affinity refer to structures whose precise details or statistical properties (respectively) are repeated as its two orthogonal dimensions are resized by independent quantities [4].

Due to the incommensurability of the orthogonal axes defining a time-series trace, such structures cannot exhibit self-similarity, only self-affinity. As an example, **Figure 7** displays the data set shown in **Figure 6** alongside a subset of the data set. When this subset is appropriately rescaled in each of the x- and y-axis, the resulting plot shares the general statistical properties of the original trace, and hence exhibits statistical self-affinity.

It also is possible, albeit less common, for a time-series trace to exhibit *exact* self-affinity. As an example, **Figure 8** illustrates three experimentally measured data sets in which rescaling the x- and y-axes of the traces by carefully chosen factors produces structures that share the characteristics of the original traces [5].

4. Fractal analysis of time-series traces: beyond box-counting

As discussed above, when applying a box-counting method to a time-series structure, the measured scaling properties of the structure will depend on the aspect ratio with which the data are presented, which is in turn an arbitrary choice. Accordingly, applying a box-counting method to a time-series trace will return a fractal dimension that is essentially arbitrary. Thus, it is necessary to develop fractal analysis techniques that are insensitive to such artificial geometric parameters. In the following, we survey a sampling of such techniques proposed in the literature.

Returning to the example of **Figure 5**, above, this figure in fact illustrates the variational box-counting method as applied to fractal profile in the form of a time-series fractal. Indeed, fractal analyses of such time-series fractal structures have traditionally been performed using the variational box-counting method [6, 7], which does offer performance improvements over the traditional fixed-grid box-counting method. Nonetheless, the variational box-counting method still suffers from a fatal flaw. To see why this is so, consider the plots shown in **Figure 9**.

Figure 9 illustrates the stock price data of **Figures 6** and 7 represented in two plots with the price axes respectively scaled by two different factors, as well as a visualization of a variational box-count method applied at a "length" scale $\ell = 200$
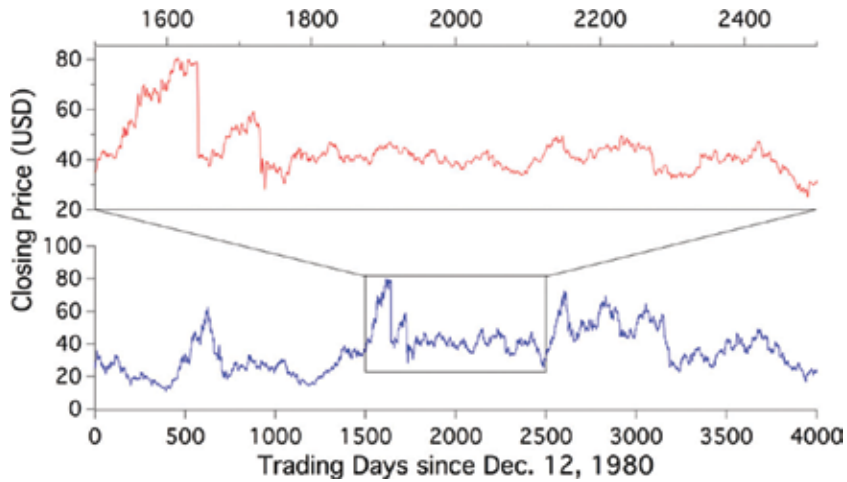
Figure 7.
*Statistical self-affinity in a fractal time-series trace. Choosing a subset of the stock price data shown in **Figure 6** and rescaling the x- and y-axes yields a trace that shares statistical properties with the original.*

trading days. When the prices shown range from 0–100 USD (top of **Figure 9**), we find that a minimum of 37 boxes are needed to entirely cover the trace. However, when the price range is expanded to 0–1000 USD (effectively increasing the domain: range aspect ratio of the data; bottom of **Figure 9**), the number of boxes needed to cover the trace falls to 20. Indeed, the number of boxes $N(\ell)$ needed to cover the "compressed" plot will be proportional to $1/\ell$ for all values of ℓ such that the boxes are "taller" than the range of values found within any of its L/ℓ columns. That is, as long as each box is "taller" than the vertical extent of the trace within each column, the trace will "look" one-dimensional.

Of course, the fundamental issue is that the concept of an $\ell \times \ell$ "box" on a time-series trace is meaningless, since the enclosed "area" has units of (in this case) days times dollars. While it is entirely reasonable to overlay a spatial figure with boxes of a well-defined area in the case of a box-counting analysis

Figure 8.
Magnetoresistance fluctuations (MCF) recorded in an electron billiard device can represent examples of exact self-affinity in time-series structures. Each of the three columns in this figure represents a single MCF observed at a coarse scale (bottom) and a fine scale (top). From [5].

Figure 9.
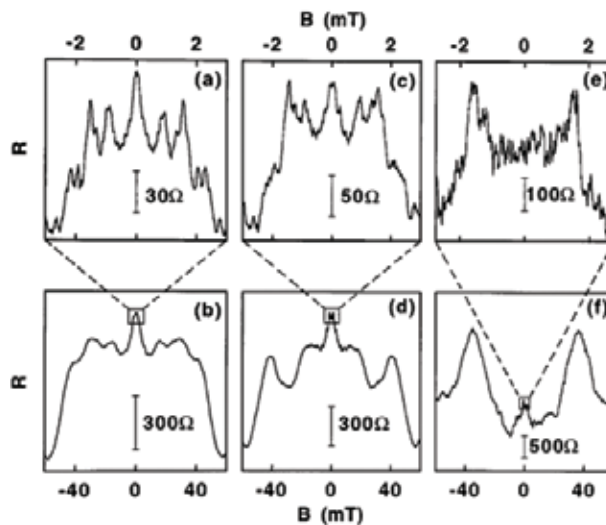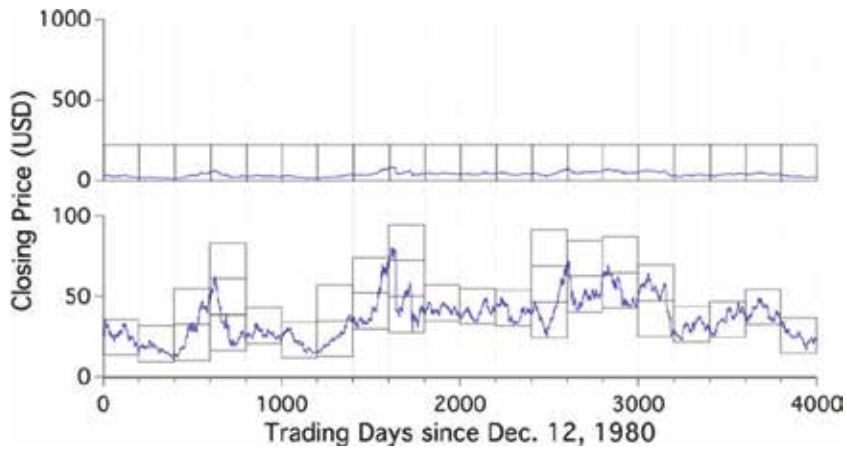*Visualizing a variational box-counting method applied to the stock price data of **Figures 6** and **7** with a "resolution" of $\ell = 200$ trading days. Displaying the data with a price range of 0–100 USD yields a box count of 37. Displaying the data with a price range of 0–1000 USD yields a box count of 20.*

of a spatial fractal, the concept of a square drawn on a plot with incompatible and independently scalable axes is ill-defined. In some cases, this inadequacy is resolved by adopting conventions that eliminate such ambiguity. For example, a time-series trace may be normalized in its *x*- and *y*-axes such that the domain and range of the plot each run from 0 to 1, and the structure may be analyzed via a box-counting analysis that utilizes a square grid that just circumscribes the trace. While such a normalization convention may provide a consistent method for investigating the relative scaling properties among a set of related time-series traces, the absolute values of the dimensions produced by such analyses would remain essentially arbitrary.

Developing a fractal analysis technique that is appropriate for time-series structures generally amounts to taking one of two approaches: (1) to treat the time-series structure as a geometric figure without a well-defined aspect ratio, or (2) to treat the time-series structure as an ordered record of a process that exhibits a quantifiable degree of randomness. Following the latter approach, Harold Edwin Hurst
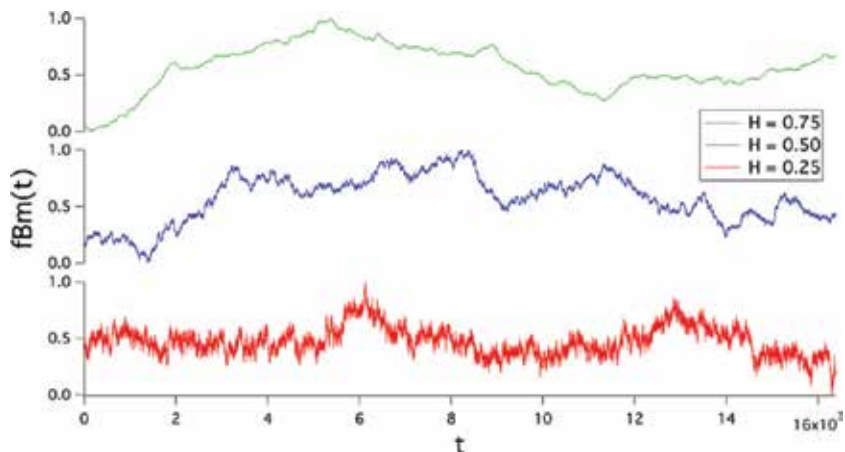

Figure 10.
Examples of time-series traces characterized by Hurst exponents of (bottom to top) $H = 0.25$, 0.50, and 0.75. A trace with $H = 0.5$ represents purely random process, whereas traces with $H = 0.25$ and $H = 0.75$ represent processes whose subsequent increments are negatively and positively correlated, respectively.

introduced a formalism for quantifying the nature of self-affine time-series structures in a 1951 paper on the long-term storage capacity of water reservoirs [8].

In Ref. [8], Hurst introduces the concept of the "Hurst exponent" H, which may be understood as quantifying the character of the randomness exhibited in a time-series structure via an autocorrelation measurement. Specifically, a Hurst exponent of $H = 0.5$ describes a process that is purely random, such that the value of the trace at time t_i is entirely independent of the value at time t_j, $i \neq j$. By contrast, Hurst exponents in the range $0.5 < H < 1$ represent traces exhibiting positive autocorrelations, while Hurst exponents in the range $0 < H < 0.5$ represent traces exhibiting negative autocorrelations. Intuitively speaking, a positive autocorrelation may be understood as representing a trace in which a "high" value (say, relative to the mean) is more likely than not to be followed by additional "high" values, while a negative autocorrelation may be understood as representing a trace in which "high" and "low" values alternate at short time scales; see **Figure 10**.

The Hurst exponent of a data set may be calculated by examining the scaling properties of a "rescaled range" of the data, as follows. Consider a data set $\{x_t\}$ ($t = 1, 2, 3, ..., T$), and let $\{x_i, x_{i+1}, ..., x_{i+\tau}\}$, $\tau \leq T$, $i = 1, 2, 3, ..., T - \tau$ represent any sequence of $\tau + 1$ points within the data set. The rescaled range (R/S) statistic is then defined as:

$$\left(\frac{R}{S}\right)_\tau = \frac{1}{s_\tau}\left[\sup_{i \leq t \leq i+\tau}\sum_{k=i}^{t}(x_k - \overline{x}_{i,\tau}) - \inf_{i \leq t \leq i+\tau}\sum_{k=i}^{t}(x_k - \overline{x}_{i,\tau})\right], \tag{1}$$

where

$$\overline{x}_{i,\tau} = (1/\tau)\sum_{t=i}^{\tau}x_t \tag{2}$$

is the sample mean and

$$s_{i,\tau} = \left[(1/\tau)\sum_{t=i}^{\tau}(x_t - \overline{x}_{i,\tau})^2\right]^{1/2} \tag{3}$$

is the sample standard deviation. The quantity

$$\left\langle\left(\frac{R}{S}\right)_\tau\right\rangle_i \tag{4}$$

is then proportional to τ^H, such that the gradient of a plot of $\log\left(\langle(R/S)_\tau\rangle_i\right)$ vs $\log(\tau)$ is equal to the Hurst exponent H.

The Hurst exponent also may be described as a measure of long-range correlations within a data set, such that measuring these correlations as a function of interval width may provide another measurement of the Hurst exponent. As an example of such an analysis, the "variance method"[3] calculates the scaling properties of the trace's autocorrelation as a function of time interval[4] via calculation of the quantity

---

[3] Not to be confused with the variational box-counting method.

[4] In all discussions of time-series traces, we refer to the independent variable as "time" as a matter of convention unless otherwise specified. Additionally, as a matter of convention, we refer to an interval of the independent variable as a "length" unless otherwise specified.

$$V(\Delta t) = \left\langle [x_{t+\Delta t} - x_t]^2 \right\rangle_t \tag{5}$$

for a range of values of Δt. This quantity is then related to the Hurst exponent as $V(\Delta t) \propto \Delta t^{2H}$ such that a plot of $\log(V(\Delta t))$ vs $\log(\Delta t)$ is expected to be linear (within an appropriate range of values of Δt) with slope. $2H$. In practice, however, the variance method is found to produce a poor estimate of Hurst exponent.

As another means of quantifying the fractal properties of time-series traces, we now turn our attention to a method proposed by Benoit Dubuc in a 1989 paper [9] on the fractal dimension of profiles. Dubuc's proposed "variation method"[5] is conceptually similar to the variational box-counting method described above, but improves upon this method by resolving the fundamental arbitrariness of drawings boxes on a time-series trace. In short, Dubuc's variation method probes the "space-filling" characteristics of a time-series trace through measurement of the scaling behavior of the amplitude of the trace within an ϵ neighborhood as ϵ is varied.

In practical terms, Dubuc's variation method may be implemented is as follows: Consider a time-series data set $\{x_t\}$ ($t = 1, 2, 3, ..., T$). For a given value of ϵ, define the functions $u_\epsilon(t)$ and $b_\epsilon(t)$ as follows:

$$
\begin{aligned}
u_\epsilon(t) &= \sup_{t' \in R_\epsilon(t)} x_{t'}, \\
b_\epsilon(t) &= \inf_{t' \in R_\epsilon(t)} x_{t'},
\end{aligned}
\tag{6}
$$

where

$$R_\epsilon(t) = \{s : |t - s| \leq \epsilon \text{ and } s \in [1, T]\}. \tag{7}$$

That is, for a given value of ϵ and for each point t_i in the trace, examine the set of points $\{x_{t'}\}$ within ϵ data points of t_i, and let $u_\epsilon(t_i)$ and $b_\epsilon(t_i)$ be (respectively) the maximum and minimum values of $x_{t'}$ found in this range. Thus, $u_\epsilon(t)$ and $b_\epsilon(t)$ may be understood as traces that represent (respectively) the upper and lower envelopes of oscillation of a trace at a particular scale set by ϵ. At large values of ϵ, the traces $u_\epsilon(t)$ and $b_\epsilon(t)$ will be slowly varying relative to the variation present in the original data set; reducing the value of ϵ will produce traces $u_\epsilon(t)$ and $b_\epsilon(t)$ that each resemble the original data set with increasing fidelity (see **Figure 11**).

Having constructed the traces $u_\epsilon(t)$ and $b_\epsilon(t)$, we then define $v_\epsilon(t) = u_\epsilon(t) - b_\epsilon(t)$ and calculate

$$V(\epsilon) = \frac{1}{\epsilon^2} \sum_t v_\epsilon(t). \tag{8}$$

Conceptually, $V(\epsilon)$ may be regarded as representing the (crucially, not necessarily integer) number of $\epsilon \times \epsilon$ "boxes" whose total "area" would be equal to that of the envelope bounded by $u_\epsilon(t)$ and $b_\epsilon(t)$. Of course, the concept of "area" is ill-defined in this context, but this is of no concern, given that we have not implied a geometrical relationship between the x and y dimensions. In continued analogy with spatial box-counting analyses, the fractal dimension of the trace is then determined via the relationship $V(\epsilon) \propto (1/\epsilon)^D$, such that a plot of $\log(V(\epsilon))$ vs $\log(1/\epsilon)$ is expected to follow a linear trend (within an appropriate range of values of ϵ) with a slope corresponding to the fractal dimension D.

---

[5] Not to be confused with the variational box-counting method or the variance method.
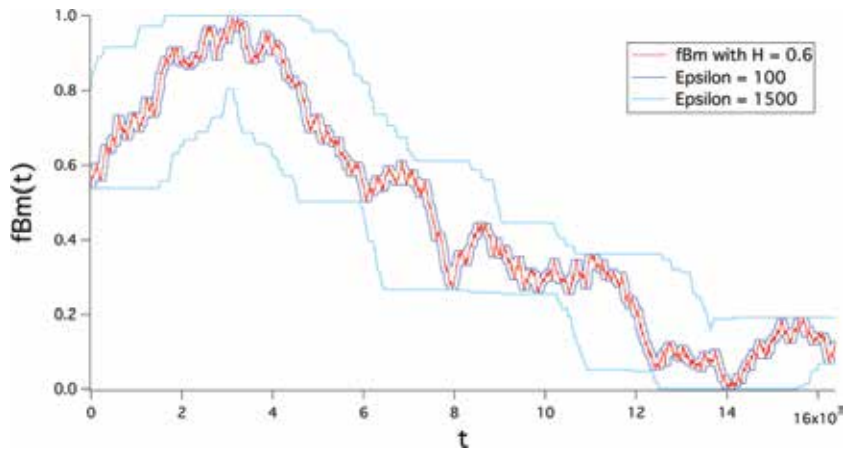
Figure 11.
Visualizing the application of Dubuc's variation method at two distinct values of ϵ. The trace under consideration is a fractional Brownian motion (fBm), whose properties are discussed below.

As a final means of quantifying the fractal properties of time-series traces, we consider a technique known as "adaptive fractal analysis" (AFA) [10]. Similar to Dubuc's variation method, AFA may be broadly described as investigating the geometrical properties of a time-series trace (in contrast to the aforementioned analyses that are best understood as probing numerical correlations). For example, and as discussed above, Dubuc's variation method may be described as quantifying the generalized "area" needed to cover a time-series trace as analyzed at different characteristic time scales; in the case of AFA, approximations to the time-series trace are generated at varying resolutions, and the fidelity of such approximations is recorded as the resolution is varied. The AFA algorithm may be executed as follows: Again, consider a time-series data set $x(t)$ $(t = 1, 2, 3, ..., T)$. Next, choose a window with a width equal to an odd integer $w = 2n + 1$, $w < T$, and partition the data set into overlapping subsets of length w such that each pair of adjacent subsets overlap by $n + 1$ data points. Within each window, the linear best-fit line to the data within that window is calculated, resulting in a series of disconnected straight lines. That is, the series of disconnected best-fit lines overlap in pairs such that each index in the domain of the original data set is matched with respective points on each of two subset fit lines (with the exception of the n data points at either end of the trace). Next, these best-fit lines are "stitched" together to form a single, smoothly continuous curve in the following manner: Label the windows that span the trace with consecutive integers, and label the windows' corresponding best-fit lines as $y^{(j)}(l)$ $(l = 1, 2, ..., n + 1)$. Then, within each window j, construct the curve

$$y^{(w)}(l) = w_1 y^{(j)}(l + n) + w_2 y^{(j+1)}(l), \qquad (9)$$

$l = 1, 2, ..., n + 1$, where $w_1 = (1 - (l - 1)/n)$ and $w_2 = (l - 1)/n$. Conceptually, each value $y^{(w)}(l)$ may be thought of as representing the weighted average of the values of the two best-fit lines with values at that index, weighted so as to be inversely proportional to the distance between that index and the midpoint of the window. Repeating this procedure across all windows produces a trace $y^{(w)}(t)$ that is continuous and differentiable, and that may be understood as representing an approximation to the trace $x(t)$ at a length scale, or "resolution," defined by w (see **Figure 12**).
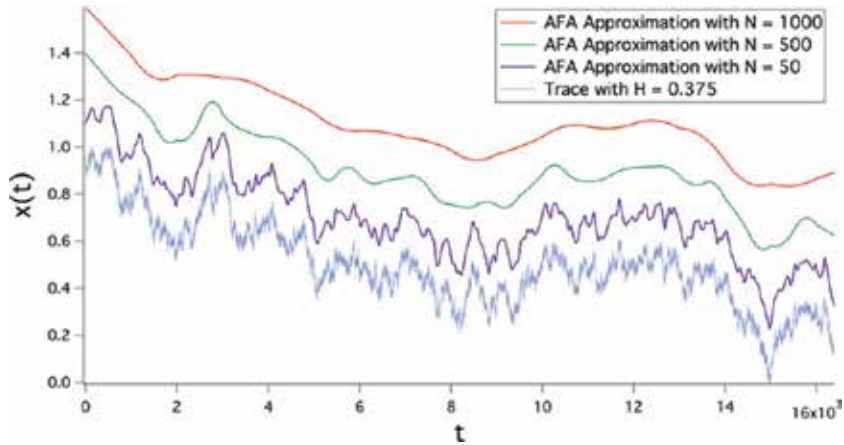
Figure 12.
Examples of applying the procedure of AFA at several values of N (corresponding to the window width w discussed in the text). The light blue trace (bottom) is a 16,384-point fractal trace with H = 0.375, while the red (top), green (second from top), and purple (third from top) traces represent approximations produced by the AFA technique at N = 1000, N = 500, and N = 50, respectively. Traces are vertically offset for clarity. Note that smaller values of N yield approximations that are increasingly similar to the trace under consideration.

As w is decreased, $y^{(w)}(t)$ becomes a better approximation to $x(t)$; the scaling behavior of this fidelity as w is varied is used to determine the Hurst exponent. Specifically,

$$F(w) = \left[\frac{1}{T} \sum_{i=1}^{T} \left(y^{(w)}(t_i) - x(t_i)\right)^2\right]^{1/2} \propto w^H,$$ (10)

such that a plot of $\log(F(w))$ vs $\log(w)$ will be linear (over an appropriate range) with slope H.

5. Evaluating fractal analysis techniques

Each of the fractal analysis techniques discussed above is best understood as providing an *estimate* of the fractal dimension or Hurst exponent that characterizes a given time-series data set. The sections that follow present a method for evaluating the fidelity of these estimates that was developed and applied by the authors to the fractal analysis techniques under consideration. To objectively and quantifiably evaluate the fidelity of each of these techniques, it is desirable to investigate the accuracy of each technique when applied to traces with known Hurst exponents/fractal dimensions. To introduce a method for producing such "control" traces, we begin with a general discussion of noise traces.

A noise trace, as an example of a time-series structure, may be described as a single-valued function of a single independent variable. A variety of methods exist for quantifying the statistical properties of noise traces. For example, in addition to the aforementioned measurements of space-filling characteristics and long-range correlations, a spectral analysis of a noise trace may offer a natural quantification of the trace's statistical properties.

Power-law noise represents a significant and broad class of noise traces. Specifically, a power-law noise trace has a power spectral density given by $P(f) \propto 1/f^{\beta}$. A noise trace characterized by $\beta = 0$ thus represents noise whose spectral power

density is a constant across all frequencies, while $\beta = 1$ corresponds to the "$1/f$ noise" that characterizes many natural systems, and $\beta = 2$ is known as "brown noise." In principle, β can assume any value; however, we begin our investigation by considering the $\beta = 2$ case.

A "brown noise" trace characterized by $\beta = 2$ is so termed owing to its relation to Brownian motion, which describes the net motion of a particle whose individual steps are random and independent. Brownian motion generally may refer to a process extending in any number of dimensions; however, we restrict our attention to brown noises that may be understood as a time-dependent plot of the position of a particle undergoing Brownian motion along one dimension. (As used herein, "Brownian motion" and "brown noise" will be used interchangeably to describe a Brownian motion in one dimension.) Given that a Brownian motion may be described as the cumulative sum of a series of random, independent steps, it is straightforward to generate a Brownian motion trace as a cumulative integral of a white noise trace. For our purposes, we define a white noise trace as a series of values with zero mean taken from a normal distribution (i.e., a Gaussian noise trace; see **Figure 13**). As a result, a brown noise trace is characterized by a Hurst exponent of $H = 0.5$.

Relaxing the restriction that the Gaussian noise trace consists of statistically independent increments permits consecutive increments to be positively or negatively correlated, such that the plot formed by the cumulative sum of the noise trace may be characterized by a Hurst exponent that deviates from $H = 0.5$. Such a trace is termed a "fractional Brownian motion" (fBm). Mandelbrot and Van Ness [11] provide a formalism for quantifying the properties of such structures as follows: Consider a conventional Brownian motion trace $B(t, \omega)$, where t denotes time and ω represents the particular realization of the random function that generated the specific Brownian motion. The data set $B(t, \omega)$ is thus a function whose increments $B(t_2, \omega) - B(t_1, \omega)$ have a mean of zero and a variance of $|t_2 - t_1|$, and whose non-overlapping increments $B(t_2, \omega) - B(t_1, \omega)$ and $B(t_4, \omega) - B(t_3, \omega)$ are statistically independent. A "reduced fractional Brownian motion" $B_H(t, \omega)$, then, is further characterized by the parameter H, $0 < H < 1$, and satisfies

$$B_H(0, \omega) = b_0,$$

$$B_H(t, \omega) - B_H(0, \omega) = \frac{1}{\Gamma\left(H + \frac{1}{2}\right)} \left\{ \int_{-\infty}^{0} \left[(t-s)^{H-1/2} - (-s)^{H-1/2} \right] dB(s, \omega) \right.$$

$$\left. + \int_{0}^{t} (t-s)^{H-1/2} dB(s\omega) \right\}. \tag{11}$$

A fractional Brownian motion trace is thus self-affine in the sense that

$$\{B_H(t_0 + \tau, \omega) - B_H(t_0, \omega)\} \triangleq \{h^{-H}[B_H(t_0 + h\tau, \omega) - B_H(t_0, \omega)]\}, \tag{12}$$

where

$$\{X(t, \omega)\} \triangleq \{Y(t, \omega)\} \tag{13}$$

denotes that the two random functions $X(t, \omega)$ and $Y(t, \omega)$ have identical finite joint distribution functions [11]. Thus, on average, when an interval on an fBm trace is expanded by a factor of h, the difference of the values at the endpoints of the interval $B_H(t_0 + h\tau, \omega) - B_H(t_0, \omega)$ increases by a factor of h^H. This property represents an example of statistical self-affinity, in which the observed statistical properties within the intervals are preserved when the x and y axes are scaled by distinct factors (specifically, h and h^H, respectively).
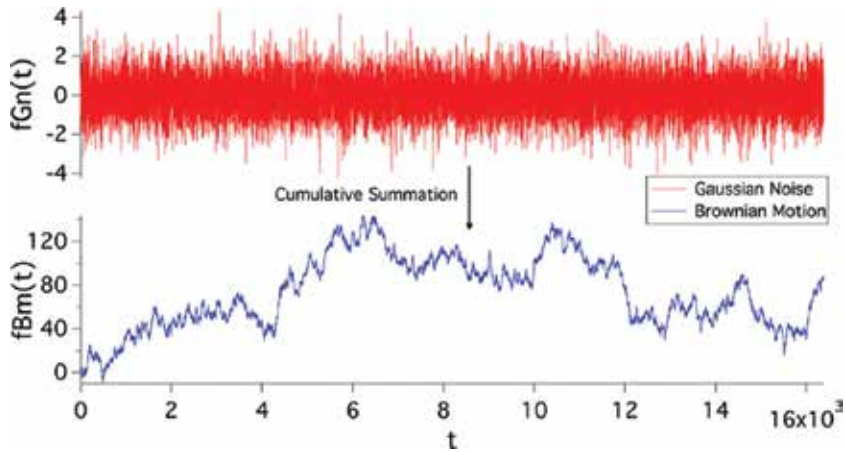
Figure 13.
The cumulative sum of Gaussian white noise results in Brownian motion.

Quantifying self-affinity using the formalism of the Hurst exponent motivates drawing a parallel between the Hurst exponent and the fractal dimension, as follows. Following the argument of Ref. [4], consider an fBm trace $V_H(t)$ that extends over a total time span $\Delta t = 1$ and a total vertical range $\Delta V_H = 1$. Dividing the time span into n increments of width $1/n$, we expect the vertical range of the portion of the trace within each interval to scale as $\Delta t^H = 1/n^H$ (see **Figure 14**). Accordingly, on average, the portion of $V_H(t)$ present in a given interval may be covered by $\Delta V_H/\Delta t = (1/n^H)/(1/n) = n/n^H$ square boxes of side length $1/n$. Thus, the total number of square boxes of side length $1/n$ needed in order to cover the entire trace is expected to be $n(n/n^H) = n^{2-H}$. If we recall that the spatial box-counting method
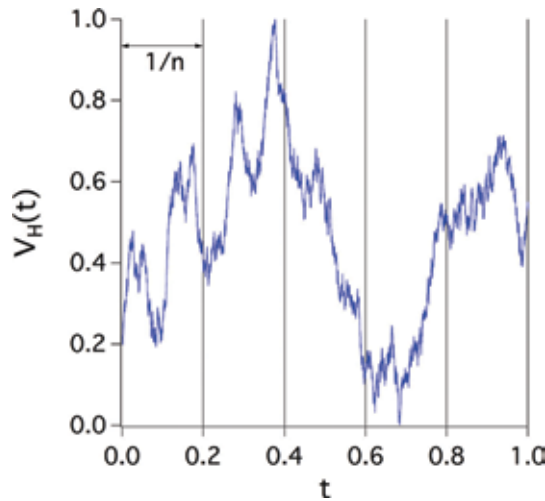
Figure 14.
Deriving a relationship between the Hurst exponent and fractal dimension. A Brownian motion trace $V_H(t)$ ($H = 0.5$) is normalized in both dimensions to be circumscribed inside a unit square, and subsequently is divided into n intervals of width 1/n. The self-affinity of an fBm trace leads to an estimation of the number of square boxes needed to cover the trace at a given length scale, motivating a relationship between H and D_F. See text for details.

relates number of square boxes of side length ℓ needed to cover a trace to the fractal dimension of the trace as $N(\ell) \propto (1/\ell)^{D_F}$, we may conclude that[6] $D_F = 2 - H$.

The relationship $D_F = 2 - H$ is appealing in its simplicity, and indeed is frequently found in the literature; however, Ref. [4] is quick to acknowledge the inherent difficulty in assigning a fractal dimension to a self-affine structure, given that such a construction is predicated upon assigning an arbitrary rescaling relationship between incompatible coordinates. Mandelbrot, too, notes the apparent relation $D_F = 2 - H$ [12] and clarifies that this relation holds in the fine-scale limit. This disparity serves to highlight a general distinction between the Hurst exponent and the fractal dimension as descriptors of a time-series trace. Specifically, the Hurst exponent may be understood as a descriptor of *global* correlations, while the fractal dimension may be understood as describing a trace's *local fine-scale structure* [13].

6. Relationship between fractal dimension and spectral exponent

We may continue this exercise of comparing our various statistical parameters by considering the spectral exponent β as a means of quantifying the nature of a fractal trace. In practice, it is impractical to utilize a spectral analysis to evaluate the fractal properties of a time-series structure, due to the imprecision (relative to the aforementioned fractal analysis techniques) of applying a power law best-fit curve to characterize a spectral decomposition of a trace. Nevertheless, we may investigate the relationship that exists between the spectral exponent β, the fractal dimension D_F, and the Hurst exponent H, so long as we recognize the imprecisions of these comparisons. In particular, the spectral exponent β typically is said to relate to the Hurst exponent as $\beta = 2H + 1$, implying the relationship $D_F = (5 - \beta)/2$. This relationship may be derived by observing that the two-point autocorrelation function

$$G_V(\tau) = \langle V(t)V(t+\tau) \rangle - \langle V(t) \rangle^2 \propto \tau^{\beta - 1} \tag{14}$$

for a trace $V(t)$ is related to the quantity $\left\langle |V(t_\tau) - V(t)|^2 \right\rangle$ as

$$\left\langle |V(t_\tau) - V(t)|^2 \right\rangle = 2\left[\langle V^2 \rangle - G_V(\tau) \right]; \tag{15}$$

comparing this result to the aforementioned relationship

$$\left\langle |V(t+\tau) - V(t)|^2 \right\rangle \propto \tau^{2H} \tag{16}$$

leads to the expression $\beta - 1 = 2H$ [14]. However, systematic study [15] demonstrates that such a relationship is generally not very robust. Indeed, it is straightforward to test this robustness: In analogy to the investigation performed in Ref. [15], we investigated the relationship between spectral exponent and fractal dimension by generating a set of 20 noise traces, each with a length of 16,384 points and with a β value between 0 and 2. Applying each of the previously discussed time-series fractal analysis techniques to each of these traces produced a corresponding set of fractal dimensions (for the variational box-counting analysis and Dubuc's variation analysis) or Hurst exponents (for the variance analysis); these data are shown in **Figure 15**, with the Hurst exponents "converted" to fractal dimensions via

---

[6] Note that this relation only applies to time-series fractals, since the notion of a Hurst exponent is undefined for spatial fractals.
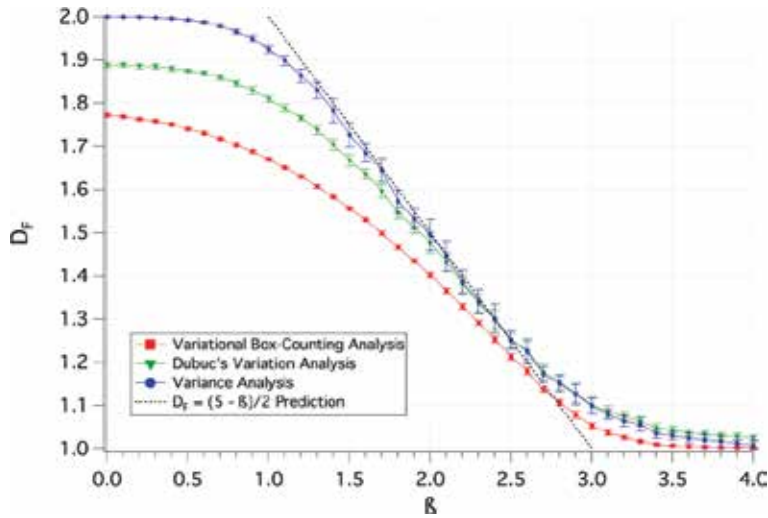
Figure 15.
Measured fractal dimensions of colored noise traces generated with well-defined power spectral densities β. Each data point represents the average value of D_F measured with the respective fractal analysis method for the set of 20 traces at the corresponding value of β. Each error bar represents one standard deviation from the mean value of D_F recorded for each set of 20 traces. Lines connecting the data points are provided as a guide to the eye. The dashed line corresponds to the relationship $D_F = (5 - \beta)/2$.

$D_F = 2 - H$. Plotting these measured parameters as a function of the well-defined spectral exponent used to generate each trace, we see that the relationship $D_F = (5 - \beta)/2$ breaks down for D_F close to 1 or 2.

7. Generating fractional Brownian motions and characterizing fractal analysis techniques

The framework of the investigation summarized in **Figure 15** may be applied to a more thorough investigation of the fidelity of each fractal analysis technique discussed above. That is, if we generate a fBm trace with a well-defined Hurst exponent and subject such a trace to the analysis techniques under consideration, we may evaluate the robustness of each analysis technique. In so doing, we may evaluate not only the fidelity of each analysis method, but also may explore how the analysis methods (individually and/or collectively) respond to less-idealized data sets. That is, by generating fBm traces with well-defined Hurst exponents and modifying the traces to better resemble real-world data sets, we may gain insight into how best to interpret our analytical results of experimentally derived data. Specifically, in addition to testing these analysis techniques on "full-size" 16,384-point fBm traces (with 16,384 arbitrarily chosen as a "sufficiently large" number), we additionally tested these analyses on traces of reduced length and/or reduced spectral content, which may better represent experimentally measured data sets.

A variety of methods exist for generating a fractional Brownian motion trace that exhibits a well-defined predetermined Hurst exponent. Examples of such methods include random midpoint displacement, Fourier filtering of white noise traces, and the summation of independent jumps [14]. This chapter considers randomly generated fBm traces that were created using a MATLAB program that generates a fractional Gaussian noise trace with the desired Hurst exponent via a

Fourier transform and subsequently computes the cumulative sum of the noise trace to yield a fractional Brownian motion trace with a specified well-defined Hurst exponent.

While such computer-generated fBm traces are accurately described as exhibiting a well-defined Hurst exponent, the inherently finite nature of these traces precludes the traces from being fully "fractal." That is, as with any natural structure with finite extent, the generated fBm traces necessarily exhibit a fine-scale resolution limit (owing to the point-wise granularity of the traces) as well as a coarse-scale size limit (owing to the finite total length of the traces). With this in mind, we must be content to forge ahead with the simplifying assumption that the effects of these particular limitations on our estimates of the underlying fractal scaling properties are negligible when considering a computer-generated fBm trace whose total length exceeds its step increment by several orders of magnitude. Accordingly, for the purposes of this analysis, we assume that an fBm trace generated with a predetermined Hurst exponent "H_{in}" and with a total length well in excess of its resolution limit is a suitable representative of a pure fractal structure characterized by H_{in}. Thus, we assume that such a trace may fairly be used as a control against which the fidelity of the above-mentioned analysis techniques may be evaluated.

The procedure for evaluating each of these analysis techniques is thus as follows: We first generated a set of 50 16,384-point fBm traces as well as 50 512-point fBm traces at each of 39 input Hurst exponents H_{in} between 0.025 and 0.975. In this manner, we sought to evaluate not only the fidelity of each fractal analysis technique in returning the expected results for the longer 16,384-point traces, but also the effect of performing the same analyses on data sets of limited length. Next, we applied each analysis technique under consideration to each of these traces, returning either a measured Hurst exponent H_{out} or a measured fractal dimension D_{out}. In the case of the Dubuc variation analysis, which returns a measured fractal dimension, this value was "converted"[7] to a Hurst exponent via the relation $H_{out} = 2 - D_{out}$. Having extracted these values of H_{out} for each sample fBm trace and for each analysis technique, we produced a plot of H_{out} vs H_{in} representing all fBm traces analyzed with each analysis technique; these results are displayed in **Figures 16** and **17** for randomly-generated fBm traces with lengths of 16,384 points and 512 points, respectively. In each of **Figures 16** and **17**, each data point represents the average H_{out} value measured via the corresponding analysis method. Each corresponding logarithmic scaling plot was fit to a straight line between a fine-scale cutoff of five data points and a coarse-scale cutoff of 1/5 of the full length of the trace. Each error bar represents one standard deviation in the measured values averaged to yield the corresponding data point. The dashed black line represents the ideal relationship $H_{out} = H_{in}$; that is, data points representing traces whose measured H_{out} values exactly match their generating H_{in} values would fall on this line.

In the ideal case of a perfectly fractal fBm trace subjected to an analysis technique that produces a precise and accurate value of the Hurst exponent, a plot of H_{out} vs. H_{in} is expected to be linear with unity slope. Based on the results of the analyses summarized in **Figures 16** and **17**, our results may be summarized as follows: the variational box-counting method tends to over-estimate H except in the case of high H values; the variance analysis tends to under-estimate H; the Dubuc

---

[7] As discussed above, such a conversion is at best an approximation. Nonetheless, utilizing this conversion serves as a self-consistent means of evaluating the response of this analysis technique when applied to fBm traces of a known Hurst exponent, as well as deviations from this behavior.
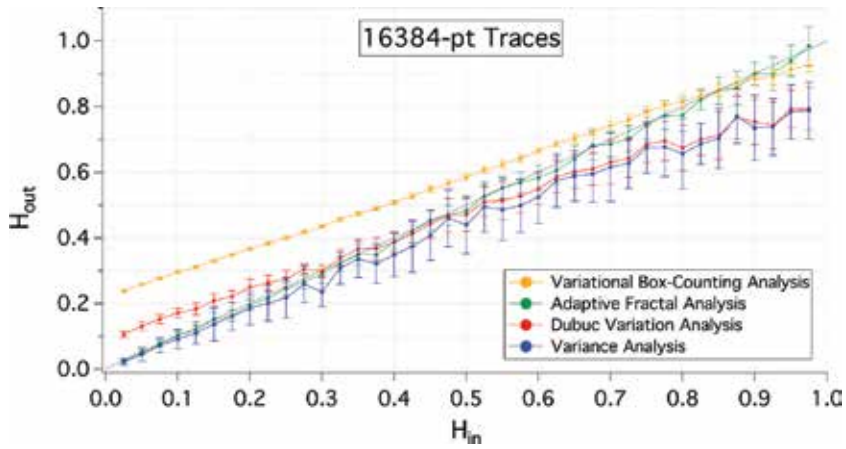
Figure 16.
Plotting H_{out} vs. H_{in} for randomly-generated-16,384-point fBm traces as measured by the variational box-counting method (yellow), adaptive fractal analysis (green), Dubuc's variation analysis (red), and the variance analysis (blue).

Figure 17.
Plotting H_{out} vs. H_{in} for randomly-generated 512-point fBm traces as measured by the variational box-counting method (yellow), adaptive fractal analysis (green), Dubuc's variation analysis (red), and the variance analysis (blue).
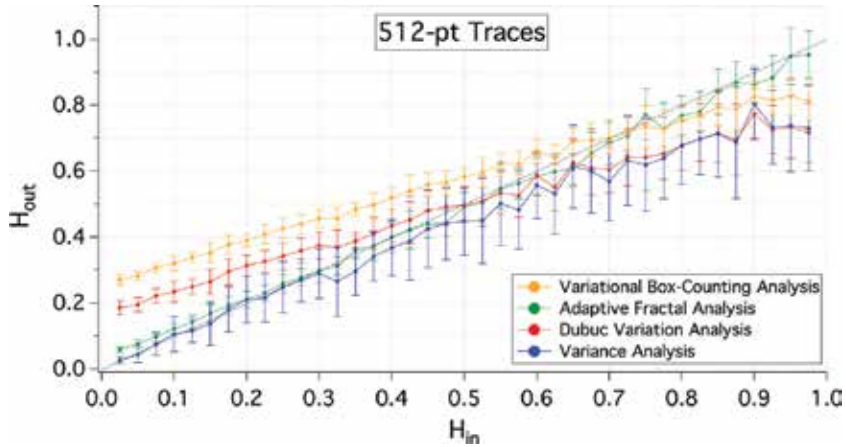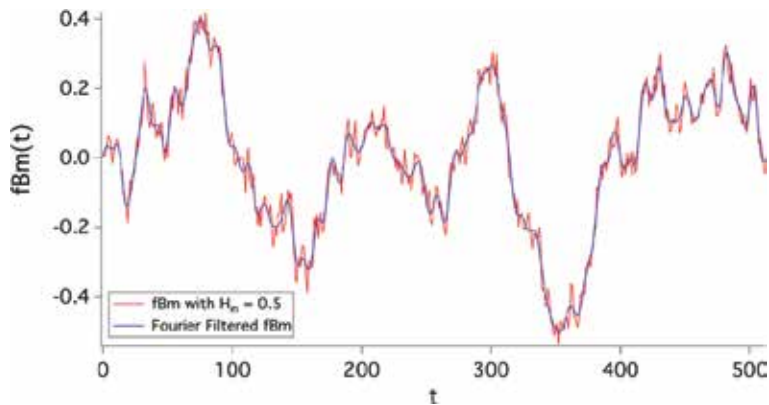

Figure 18.
Comparison of a 512-point fBm trace with $H_{in} = 0.5$ before (red) and after (blue) Fourier filtering to a minimum feature size of 10 points.

variation analysis performs well only for $H \sim 0.5$; and AFA provides an accurate estimate of H throughout the range of H values. In the case of the shorter, 512-point traces, the deviations from the ideal relationship H_{out} vs. H_{in} are more pronounced. Additionally, the precision of the estimated H values for these shorter traces suffers as well, as seen in the relatively large error bars on the data points corresponding to the shorter traces.

We also investigated the effect on the measured H values resulting from another common deviation from ideal fractal behavior. Specifically, in experimentally measured time-series data sets, the smallest-scale measured features often are significantly larger than the resolution limit of the trace. Such is very often the case for experimentally measured data sets that are asserted to represent fractal behavior, in which the finest-scale features may exhibit a characteristic scale that is well over an order of magnitude larger than the point-wise resolution of the trace. To probe the effect of this limitation on a fractal analysis of such a trace, we repeated the above technique on a set of randomly-generated 512-point fBm traces that had been
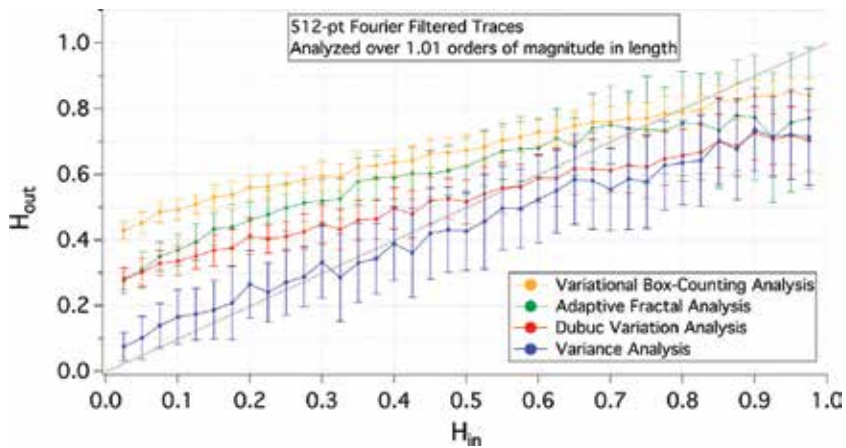

Figure 19.
Summarizing the fidelity of four fractal analysis methods in measuring the H value for randomly-generated 512-point fBm traces with a minimum feature size of 10 points. The scaling properties were observed over 1.01 orders of magnitude in length scale.

Figure 20.
Summarizing the fidelity of four fractal analysis methods in measuring the H value for randomly-generated 512-point fBm traces with a minimum feature size of 10 points. The scaling properties were observed over 0.71 orders of magnitude in length scale.
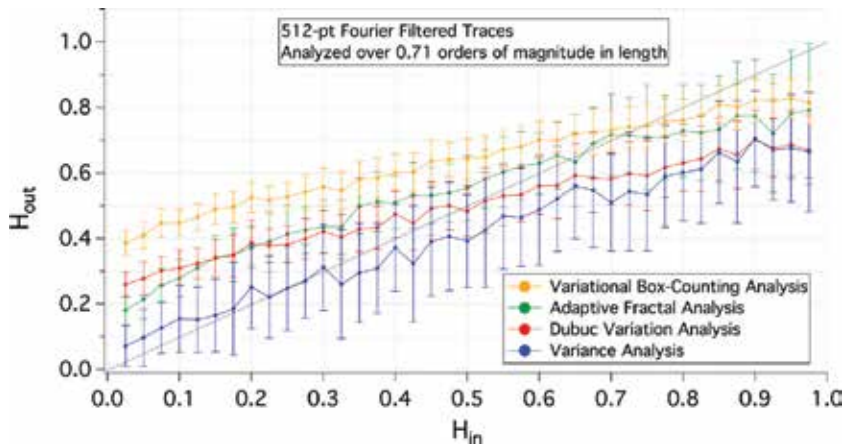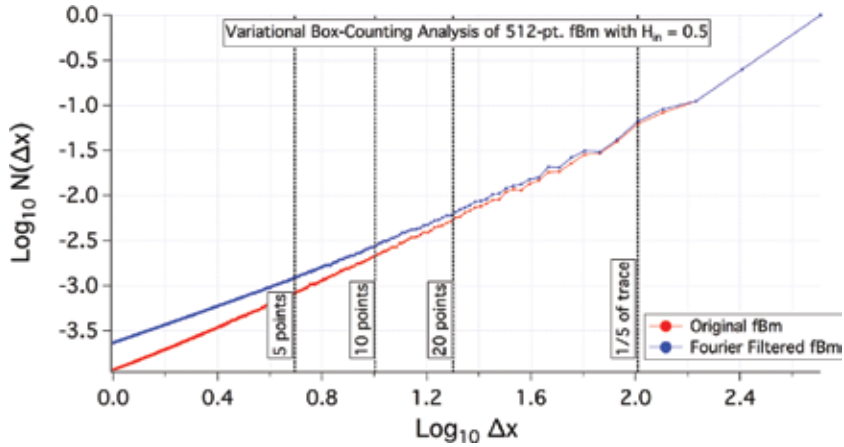
Figure 21.
Comparison of scaling plots produced by the variational box-counting method applied to a 512-point fBm trace with $H_{in} = 0.5$ before (red) and after (blue) Fourier filtering to a minimum feature size of 10 points.

spectrally filtered via Fourier transforms to exhibit a well-defined minimum feature size (i.e., a well-defined maximum frequency component). Specifically, each trace was subjected to a Fourier filter that eliminates all frequency components corresponding to periods shorter than 10 data points, such that the resultant traces have a minimum feature size of 10 points. **Figure 22** illustrates a characteristic result of this filtering procedure by comparing the original and Fourier filtered versions of an fBm trace with $H_{in} = 0.5$.

Performing a fractal analysis of time-series traces with limited spectral content requires a reassessment of the length scales over which one expects to observe the fractal scaling properties. Whereas our analysis of fBm traces whose spectral content extended to the resolution limit of the traces examined scaling properties to a minimum length scale of five data points, we now cannot expect to see such scaling properties at length scales smaller than our minimum feature size of 10 data points. Given this well-defined minimum feature size, it may be tempting to set our fine-scale analysis cutoff at 10 data points and expect to observe the desired scaling properties at all length scales greater than this. In practice, however, the effect of
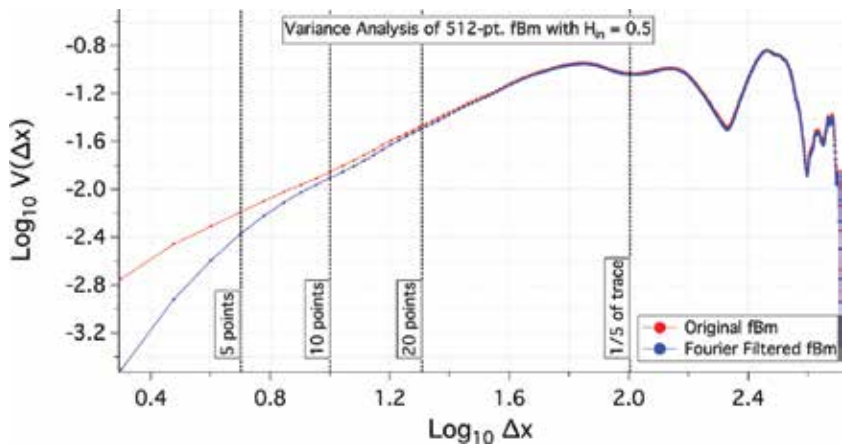

Figure 22.
Comparison of scaling plots produced by the variance method applied to a 512-point fBm trace with $H_{in} = 0.5$ before (red) and after (blue) Fourier filtering to a minimum feature size of 10 points.

such spectral filtering is manifest in a fractal analysis even at length scales significantly greater than that of the minimum feature size.

The results of passing the 512-point Fourier filtered fBm traces through the fractal analysis techniques under consideration are displayed in **Figures 19** and **20**, which illustrate the results obtained when applying fine-scale cutoffs of 10 data points (i.e., the traces' minimum feature size) and 20 data points, respectively. In each of **Figures 19** and **20**, each data point represents the average H_{out} value measured via the corresponding analysis technique using the aforementioned cutoffs at the fine scale limit and 1/5 of the entire trace as the coarse scale cutoff limit. Each error bar represents one standard deviation in the measured values that were averaged to yield the corresponding data point. The dashed black line represents the ideal relation $H_{out} = H_{in}$, as discussed above.

Examples of the logarithmic scaling plots that yielded the data summarized in **Figures 16–17** and **19–20** are provided in **Figures 21–24**. For purposes of

Figure 23.
Comparison of scaling plots produced by the Dubuc variation method applied to a 512-point fBm trace with $H_{in} = 0.5$ before (red) and after (blue) Fourier filtering to a minimum feature size of 10 points.

Figure 24.
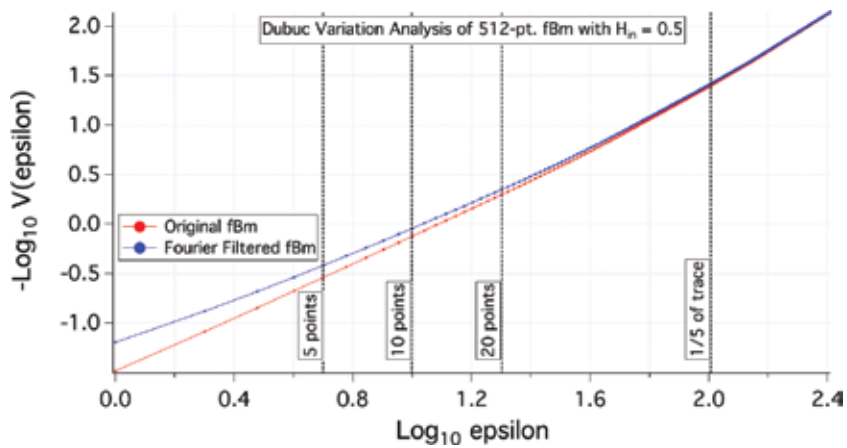*Comparison of scaling plots produced by the adaptive fractal analysis method applied to a 512-point fBm trace with $H_{in} = 0.5$ before (red) and after (blue) Fourier filtering to a minimum feature size of 10 points.*
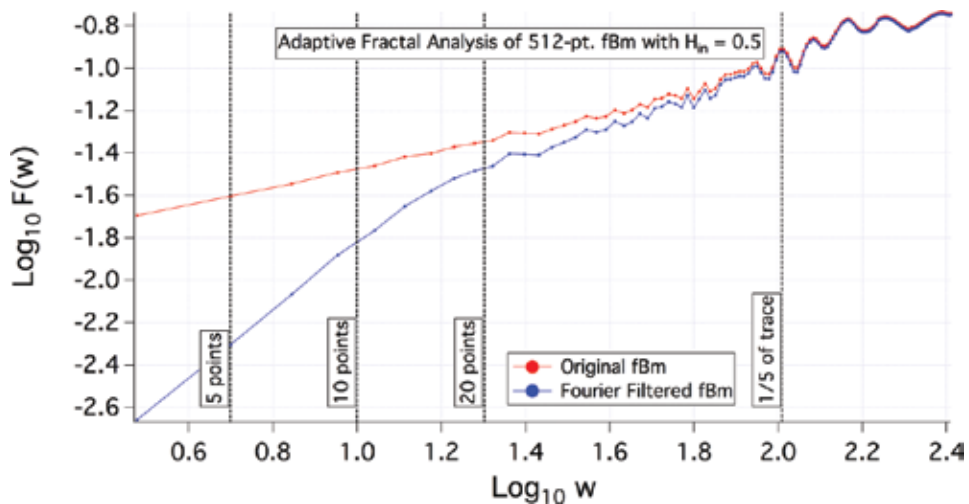
illustration, each of these figures shows the logarithmic scaling plots produced by applying the corresponding fractal analysis technique to the specific pair of fBm traces illustrated in **Figure 18**. That is, each fractal analysis technique under consideration quantifies the fractal characteristic of the input trace by determining the slope of a best-fit line to a log–log scaling plot; **Figures 21–24** provide examples of these logarithmic scaling plots.

In each of **Figures 21–24**, the vertical dashed lines indicate the cutoffs between which the scaling plot is fitted with a straight line whose slope is measured to determine H_{out}. For both traces in each of these figures, the coarse-scale analysis cutoff corresponds to the location of the line labeled "1/5 of trace." The fine-scale analysis cutoff for the raw trace (red points) corresponds to the location of the line labeled "5 points" (corresponding to the data in **Figure 17**), while the fine-scale analysis cutoff for the filtered trace (blue points) may be chosen as 10 data points (corresponding to the data in **Figure 19**) or 20 data points (corresponding to the data in **Figure 20**), as represented by respective dashed vertical lines in **Figures 21–24**.

8. Conclusions

Contrasting the trends displayed in **Figures 19** and **20** with those displayed in **Figures 16** and **17** highlights the inherent challenge in assessing the fractal properties of time-series structures that suffer from limited total length and/or limited resolution/spectral content. Indeed, accommodating the impact of a minimum feature size that is significantly in excess of the trace's resolution limit generally necessitates restricting a fractal analysis to length scales larger still than even this observed minimum feature size. This in turn often restricts an analysis of scaling properties to a consideration of relatively few orders of magnitude in length. For example, performing a fractal analysis of a 512-point Fourier filtered trace using analysis cutoffs corresponding to 10 data points and 1/5 of the trace length corresponds to an analysis of the scaling behavior over barely more than one order of magnitude in length scale; attempting to increase the accuracy of the measurement by raising the fine-scale cutoff to 20 data points further reduces the scaling range to 0.71 orders of magnitude.

Moreover, **Figures 21–24** demonstrate the difficulty in identifying an appropriate fine-scale cutoff for fractal analysis of a time-series trace, even when the minimum feature size found in the trace is easily identifiable and/or well-defined. The examples of **Figures 21–24** further highlight an important distinction between the application of fractal analysis techniques to spatial and time-series fractals. In the case of spatial fractals, it often is reasonable to expect to observe fractal scaling behavior between the length scales corresponding to physical constraints (and in particular at length scales sufficiently far from these cutoffs). By contrast, and as seen in **Figures 21–24**, the effect of imposing (or observing) a finite minimum feature size on a time-series trace is evident at *all* scales, not just at those smaller than the minimum observed period. Accordingly, and as further illustrated in **Figures 21–24**, this effect may impact the slope of a best-fit line to a logarithmic scaling plot (and, hence, the measured fractal dimension) even when this slope is evaluated between cutoffs that are expected to compensate for the fine-scale limitation.

In light of these results, one must take care when applying these analysis techniques to data sets limited in length or spectral content, as it may be difficult to make a compelling argument for the empirical presence of fractal behavior when examining such a narrow range of length scales. Nevertheless, it is instructive to

examine the behavior of fractal analysis applied to known fractal structures such as fBm traces that have been artificially subjected to such constraints. For example, one may argue that an fBm trace that is Fourier filtered to exhibit a coarser minimum feature size is analogous to a natural structure or phenomenon that has been subjected to exterior influences such as weathering effects or measurement limits: both may be considered examples of structures that are legitimately generated via processes associated with fractal behavior, but whose true fractal nature has been obfuscated by secondary considerations. In the eyes of the authors, such effects do not necessarily render the resulting structures "less fractal" than their idealized counterparts. Nevertheless, such effects demand careful consideration when choosing an analysis method and an acknowledgment of the inherent limitations thereof.

Acknowledgements

Author details

Ian Pilgrim* and Richard P. Taylor
University of Oregon, Eugene, Oregon, USA

*Address all correspondence to: pilgrim.ian@gmail.com

IntechOpen

References

[1] Mandelbrot B. How long is the coast of Britain? Statistical self-similarity and fractal dimension. Science. 1967;**156**(3775):636-638. DOI: 10.1126/science.156.3775.636

[2] Richardson LF. The problem of contiguity: An appendix to statistic of deadly quarrels. In: General Systems Yearbook. Ann Arbor: The Society for General Systems Theory; 1961;**6**:139

[3] Mandelbrot B. The Fractal Geometry of Nature. New York: W. H. Freeman and Co; 1982

[4] Voss RF. Characterization and measurement of random fractals. Physica Scripta. 1986;**T13**:27-32. DOI: 10.1088/0031-8949/1986/T13/004

[5] Taylor RP, Newbury R, Sachrajda AS, Feng Y, Coleridge PT, Dettmann C, et al. Self-similar magnetoresistance of a semiconductor sinai billiard. Physical Review Letters. 1997;**78**(10):1952-1955. DOI: 10.1103/PhysRevLett.78.1952

[6] Micolich AP. Fractal magneto-conductance fluctuations in mesoscopic semiconductor billiards [thesis]. Sydney: University of New South Wales; 2000

[7] Micolich AP, Taylor RP, Davies AG, Bird JP, Newbury R, Fromhold TM, et al. Evolution of fractal patterns during a classical-quantum transition. Physical Review Letters. 2001;**87**:036802. DOI: 10.1103/PhysRevLett.87.036802

[8] Hurst HE. Long-term storage capacity of reservoirs. Transactions of the American Society of Civil Engineers. 1951;**116**:770-808

[9] Dubuc B, Quiniou JF, Roques-Carmes C, Tricot C. Evaluating the fractal dimension of profiles. Physical Review A. 1989;**39**(3):1500-1512. DOI: 10.1103/PhysRevA.39.1500

[10] Riley MA, Bonnette S, Kuznetsov N, Wallot S, Gao J. A tutorial introduction to adaptive fractal analysis. Frontiers in Physiology. 2012;**3**(371). DOI: 10.3389/fphys.2012.00371

[11] Mandelbrot B, Van Ness JW. Fractional Brownian motions, fractional noises and applications. SIAM Review. 1968;**10**(4):422-437. DOI: 10.1137/1010093

[12] Mandelbrot B. Self-affine fractals and fractal dimension. Physica Scripta. 1985;**32**:257-260. DOI: 10.1088/0031-8949/32/4/001

[13] Gneiting T, Schlather M. Stochastic models that separate fractal dimension and the hurst effect. SIAM Review. 2004;**46**:269. DOI: 10.1137/S0036144501394387

[14] Barnsley MF, Devaney RL, Mandelbrot B, Peitgen HO, Saupe D, Voss RF. The Science of Fractal Images. New York Inc: Springer-Verlag; 1988

[15] Labate D, Canavero F, De Marchi A. A comparison of fractal dimension and spectrum coefficient characterization of $1/f^{\alpha}$ noise. Metrologia. 1994;**31**(51). DOI: 10.1088/0026-1394/31/1/011

Fractal Geometry: An Attractive Choice for Miniaturized Planar Microwave Filter Design

Hadi T. Ziboon and Jawad K. Ali

Abstract

Various fractal geometries are characterized by the self-similarity and space-filling properties. The space-filling feature has been successfully applied to design multiband antenna structures for a wide variety of multifunction wireless systems. On another hand, the second feature has proved its validity to produce miniaturized antennas and passive microwave circuits including the band-pass filters (BPF). This chapter demonstrates the design of miniaturized microstrip BPFs that are derived from fractal-based DGS resonators. Many microstrip BPFs based on the Minkowski fractal DGS resonators will be presented together with those based on Moore and Peano fractal geometries. Simulation results, of all of the presented BPFs, show that an extra-size reduction can be obtained as the iteration level becomes higher. Measured and simulated results agree well with each other. A comparison has been conducted with other filters based on Peano and Hilbert fractal geometries. The results reveal that the proposed BPF offers acceptable performance and a significant decrease of higher harmonics.

Keywords: miniaturized microwave BPF, fractal-based DGS, Minkowski fractal geometry, Moore fractal geometry, Peano fractal geometry

1. Introduction

Microwave antenna and passive circuit designers have to meet the ever encountered challenges to produce components with miniaturized size and multiband operation. To meet these challenges, the various fractal geometries have been found to be an attractive choice. These geometries have two unique features: the space filling and the self-similarity. For more than two decades, these features have opened the novel and essential techniques for the design of the microwave antennas and passive circuits. The benefits of incorporating these geometries are, among many, enhanced bandwidths, compact sizes, partless electronic parts, and improved performance. Furthermore, fractal-based structures offer an additional epoch of optimizing design mechanisms. These mechanisms are applied successfully in the antenna design, although they can be implemented in a wide-ranging way [1].

Away from the application of the different fractals to produce small-size microwave filters, the use of fractal geometries has been earlier to take place. In this context, the antenna design and the distinctive features, that the various fractal-based structures have, were efficiently adopted to create compact size multi-resonant

antennas [2–9]. Besides, researchers have effectively proposed a variety of fractal geometries to modify to the typical microstrip structures which are efficiently endorsed to obtain miniaturized size of multiband antennas and BPFs for great types of wireless communication. In this perspective, the classical Euclidean shapes, such as the square, have been shaped in the form of the Sierpinski carpet to design a dual-mode BPF [10, 11]. Numerous traditional fractal structures attracted the microwave passive circuit designers to produce of miniaturized microstrip BPFs as well [12, 13]. Microstrip structures with Peano fractal-shaped resonators and its modification were employed in the conventional resonators to fabricate efficient miniaturized single- and dual-mode BPFs with single-band performance and also dual-mode implementation [14–17]. Researchers attempted to try modified versions of the classical fractals in the attempt to get higher space-filling curves to design highly miniaturized resonant structures. The modified variants of the Minkowski fractal proved its validity to suggest microstrip BPFs with more size reduction [18–21]. As an impressive result, the Minkowski fractal-based BPFs are character-ized with a resonant performance with reduced harmonics [22].

In contrast, the defected ground structures have been applied to design min-iaturized BPFs. Enhanced filter characteristics have shown to be attractive, and a growing research effort has been devoted to this topic as implied in the literature. However, most of the reported studies have been dedicated to the design of the microstrip LPFs. It is worth here to say that the application of various fractals and their variants to reshape the defected ground structures has revealed to be success-ful to offer extra-size reduction besides the improved filter performance [23–28]. The conventional Hilbert fractal geometry has been adopted to modify a defected ground structure in an attempt to produce a miniaturized microstrip low-pass filter [23]. A defected ground structure that has been modeled according to the Hilbert fractal curve is implemented to enhance the out-of-band performance of the filter. The fractal structure has been loaded with open stubs for this purpose. The Sierpinski carpet-based defected ground structure is successfully utilized to produce a microstrip low-pass filter as reported in [24]. Also, the variants of the Minkowski and Koch fractals were employed to modify the shape of a defected ground structure CSRR to produce a compact-size band-pass filter [25, 26].

In this chapter, the design of a miniaturized microstrip band-pass filter is loaded with a fractal-shaped defected ground structure. A Minkowski fractal variant, with various iteration orders, has been adopted in the modification of the form of the defected ground structure of the proposed BPF. In addition to the reduced size, the proposed band-pass filter is found to present acceptable resonant characteris-tics with harmonics reduction capability. Even though the various fractals in the production of defected ground structure resonators are used to construct miniatur-ized microstrip band-pass filters, it is interesting to mention that the proposed filter design presented in this work has overperformed numerous of its category since it possesses a considerably reduced size besides the acceptable performance.

2. The modified Minkowski fractal geometry

The most critical criterion in the selection of a fractal curve, from the aspect of the microwave circuit miniaturization, is its dimension. The higher the fractal dimension, the better the fractal curve fills the given area, therefore achieving higher compactness. The generation process of the traditional Minkowski fractal curve is adopting a square with 1/3 unit side length, instead of an equilateral triangle of the same side length. The corresponding fractal dimension is 1.465. For comparison purposes, **Table 1** shows the fractal dimensions of some fractal curves

Fractal curve type	Fractal dimensions
Koch curve	1.2618
Sierpinski triangle	1.5848
Sierpinski carpet	1.8928
Koch snowflake	1.2618
Cantor set	0.631
Minkowski curve	1.465

Table 1.
The fractal dimensions of some fractal geometries [29].

that are widely adopted in the design of microwave antennas and circuits. For this, to enhance the input/output coupling and to obtain a practical range of the fractal dimension of the standard Minkowski fractal curve, a modified variant is introduced.

Figure 1 illustrates the generation process of the proposed Minkowski fractal variant. The figure shows the generation of the modified version up to the second iteration as applied to a square ring. In this version, the typical 1/3 ratio which is the most popular in the generation of the majority of various fractal curves has been replaced by an arbitrary ratio.

As the generation process implies, the shape variations in the sequential steps, depicted in **Figure 1(b)–(d)**, can be thought as a means to enlarge the surface charge density pat as compared with that of the typical square ring resonator. This increase of the path length will lead to lower the resonant frequency. In other words, this will decrease the size of the resulting filter if the operating frequency is kept unchanged. For the nth iteration, the proposed Minkowski fractal variant has been found to have the perimeters given by

$$P_n = \left(1 + 2\frac{w_2}{L_\circ}\right)P_{n-1} \tag{1}$$

where P_n is the perimeter of the nth iteration fractal structure, w_2 and $L_\circ$ are as depicted in **Figure 1**. Examining Eq. (1) and **Figure 1**, it is clear that at a specific iteration level, when varying w_1, w_2, or both, a broad diversity of structures with distinctive perimeters can be achieved.

According to Falconer [29], the modified version of the Minkowski fractal geometry is called multi-fractal or fractal geometry with more than one ratio in the generator: a_1 and a_2. For this case, the fractal dimension, D, can be obtained from the solution of the following equation:

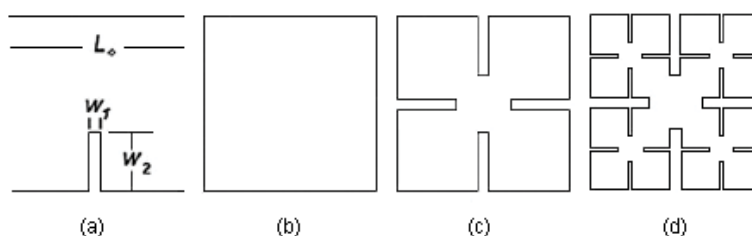$$2\left(\frac{1}{2}(1-a_1)\right)^D + 2a_2^D + a_1^D = 1 \tag{2}$$

Figure 1.
The generation process of the proposed Minkowski fractal variant [18, 25].
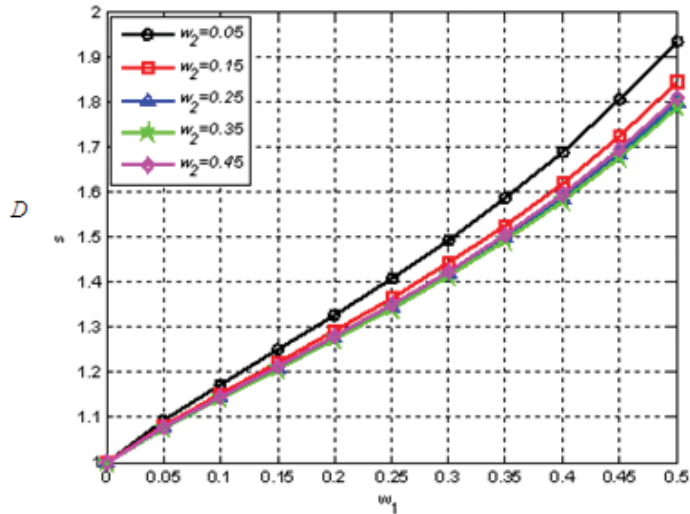
Figure 2.
The variation of the fractal dimensions of the modified Minkowski fractal with the parameter w_2 as a parameter [30].
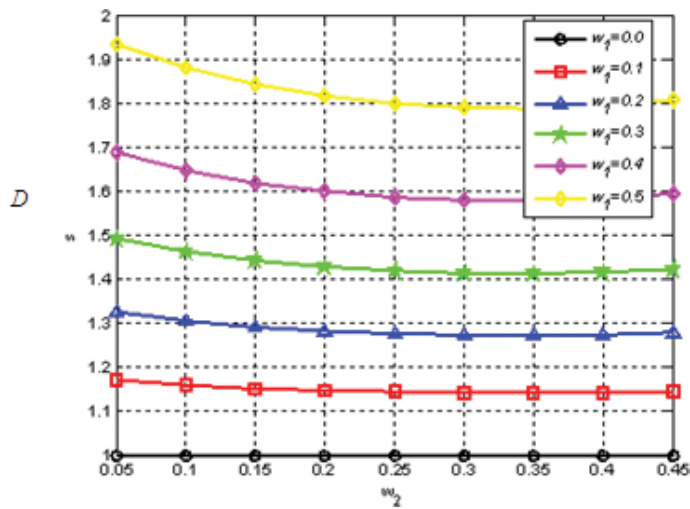

Figure 3.
The variation of the fractal dimensions of the modified Minkowski fractal with the parameter w_1 as a parameter [30].

where a_1 and a_2 are the ratios w_1/L_o and w_2/L_o, respectively. The parameters w_1, w_2, and L_o are as indicated in **Figure 1**.

To demonstrate the effects of varying w_1 and w_2 on the resulting dimension of the modified Minkowski fractal structure, Eq. (2) has been plotted against w_1 and w_2 for as shown in **Figures 2** and **3**, respectively. The parameter w_1 has been varied from zero to 0.5 in steps 0.1, while w_2 has been ranged from 0.05 to 0.45 in steps of 0.1.

Examining **Figures 1**–**3** and Eq. (2), it is clear that when w_1 is equal to zero, the fractal dimension will equal to 1, which represents the non-fractal state. In this case, the resulting structure is not with a fractal shape; it is merely a Euclidean square which has the dimension of 1. Furthermore, when w_1 and w_2 are both equal to 1/3, which is the case with the conventional Minkowski fractal curve, the dimension will be 1.465 as shown in **Table 1**.

As a conclusion, it is likely that further size reduction will take place after the application of the fractal-based structures to the traditional Euclidean-shaped resonators. This process implies that the increased space filling of the modified structures, at the successive iteration levels, will lead to an additional size reduction. The enlargement in the resulting length will result in the reduction of the corresponding size required to implement the fractal-based BPF. Hypothetically, as n goes to infinity, the resulting occupied length will approach to infinity. The capability of the new structure to enlarge its length in the following iteration levels has been shown fascinating for investigating its size reduction ability as a microstrip BPF.

3. The proposed filter design

In this work, many band-pass filters with fractal-based defected ground structures were modeled. The ground planes of these microstrip filters are defected using slots in the shape of two coupled resonators [31]. The suggested DGS consists of two coupled open-loop slot resonators in the form of the Minkowski fractal variants depicted in **Figure 1(b)**–**(d)**. Three microstrip band-pass filters have been modeled. Each filter has a fractal-based defected ground structure corresponding to a specified iteration order. The performance evaluation of each filter has been carried out using the commercially available EM simulator, IE3D [32].

Figure 4 demonstrates the configuration of the proposed microstrip DGS BPF filter. Here, it is clear that L denotes the resonator side lengths of the filters, D is the gap width, X is the inter-resonator spacing, and W is the distance between the longitudinal filter center and the transmission line lower edge. It is apparent that two coupled open-loop slots defect the ground plane of this filter. The slots take the shape of the Minkowski fractal variant of the second iteration. The proposed band-pass filter is constructed using a substrate with a relative permittivity of 2.65 and thickness of 1.0 mm. A microstrip transmission line is printed on the top of the substrate as shown in **Figure 4(b)**. A gap with a width D is etched in its center.
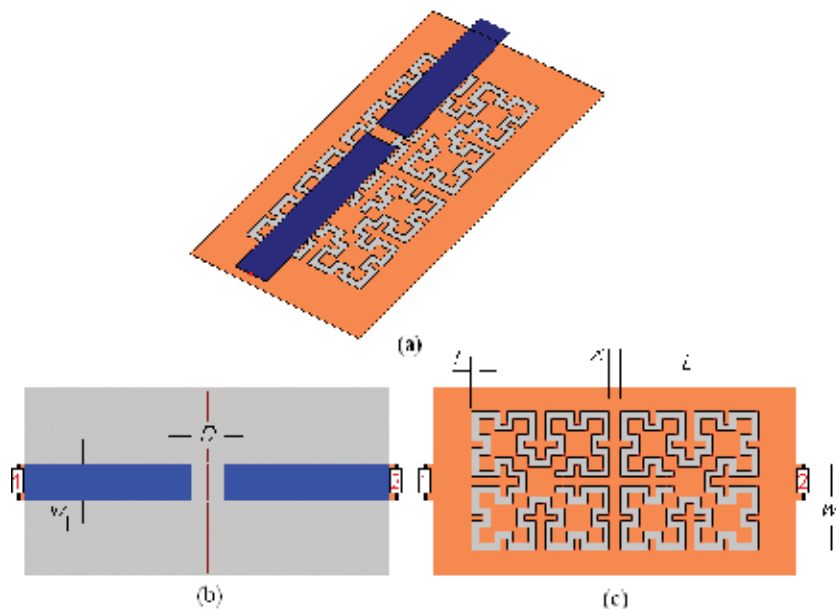

Figure 4.
(a) The layout of the proposed DGS BPF, (b) the front and (c) the back views [31].

The input/output ports have 50 Ω characteristic impedance. The corresponding transmission line width is found to be 2.75 mm. The defected ground structures are etched on the bottom side of the substrate as demonstrated in **Figure 4(c)**.

Throughout the simulation of the proposed BPF, the length L is maintained constant as that of the open-square-loop resonator. Consequently, at the design frequency of 2.45 GHz, the length L, for the simulated band-pass filter with the square open-loop resonator is equal to 12.50 mm at resonance. This value corresponds to about 0.15 λ_g. Then, λ_g is calculated as

$$\lambda_g = \frac{\lambda_o}{\sqrt{\varepsilon_{reff}}} \tag{3}$$

where ε_{eff} is the effective permittivity. Various EM simulators provide the means to calculate ε_{eff} using an embedded calculator. However, the empirical expressions required for the computation of ε_{eff} can be found in the literature [33]. On the other hand, the application of the fractal structures means that an extensive length will be added to that of the resonator structures. In this case, it is not conditional that the new lengths are equal to half or multiple of λ_g at resonance. This is because not all the resonator length will be part of the cause of realizing resonance. This fact becomes more evident when studying the charge density distributions on the various parts of the modeled filters.

It should be mentioned that the resonator lengths, L, of the simulated BPFs are kept fixed at a specified value. In the next section, it will become apparent that the parameters D, X, and W play a crucial influence on the final BPF resonant responses.

4. The simulation results

The resonant response of a band-pass filter is, in general, assessed all over its passband specifications, together with its passband insertion loss. It is essential that the insertion loss has not exceeded a certain specified level, and it should be reliably below some particular value throughout the occupied passband. The band-pass filter has to offer as much elimination of undesired signals as possible, both in its lower stopband and upper stopband outside of the low-loss passband. However, to describe the degree of selectivity of a band-pass filter, the term what is the roll-off rate is introduced [34, 35]. The roll-off rate, R, of a BPF response, is defined as

$$R = \frac{|\alpha_{max} - \alpha_{min}|}{|f_s - f_c|} \tag{4}$$

where α_{max} and α_{min} are the 40 dB and the 3 dB attenuation points, respectively, while f_s and f_c are the 40 dB stopband and the 3 dB cutoff frequencies. It should
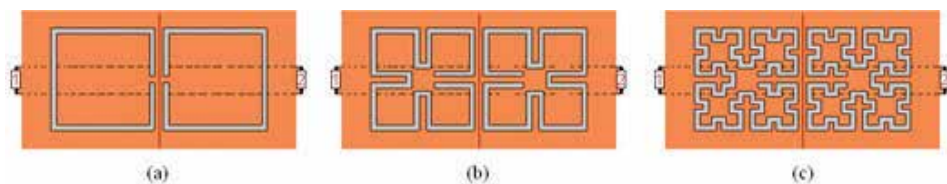

Figure 5.
The configurations of the simulated band-pass filters with: (a) zero, (b) first iteration, and (c) the second iteration fractal-based defected ground structures [31].

be noted that various values might be specified for α_{max} to find out the roll-off rate [36]. However, in this work α_{max} has been chosen to be 40 dB. Many BPFs with the defected ground structures, based on those shown in **Figure 5**, were modeled, and their performance responses have been evaluated. Two BPFs were modeled, both with the fractal-based resonators defected ground structures as those shown in **Figure 5(a)** and **(b)**.

5. A parametric study

Three band-pass filters with fractal-detected ground structures, shown in **Figure 5(a)**–**(c)**, were simulated, and their performance responses have been evaluated. The side length L of all the coupled DGS resonators of the modeled filters has been kept unchanged at 12.50 mm and slot trace width, T of about 0.61 mm. At this length, the zero iteration-detected ground structure BPF resonates at 2.50 GHz. For the three modeled filters, a parametric study was achieved to explore the effects of the different BPF elements, mainly D, X, and W, on its resonant behavior as will be presented in the following subsections.

5.1 The first iteration fractal DGS BPF

The impact of making the gap width D varied, while maintaining the other filter structure elements fixed, has been demonstrated in **Figure 6**. The increment of D causes the response transmission zeros to move away from the center frequency position, while approximately it does not affect the filter passband. Furthermore, as D is increased further, the realized BPF bandwidth is extended at the expense of the reduction of the filter selectivity. At a specific value of D, the upper transmission zero will vanish.

On the other hand, when the spacing X is made variable, the resulting responses are displayed in **Figure 7**. In contrast with the impact of changing D, the variation of X will be insignificant on the overall filter response including both the passband and the stopband.

The variation of the distance between the longitudinal filter center and the transmission line lower edge, W, has a considerable impact on the resulting filter responses as clearly demonstrated in **Figure 8**. In this case, both of the filter passband and stopband are significantly worsened. As the feed line becomes near the edge of
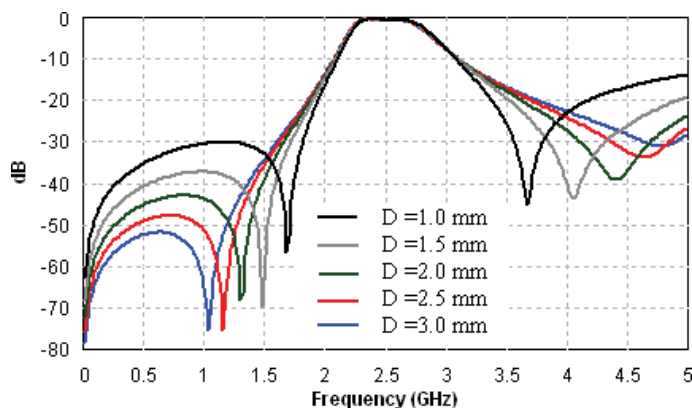

Figure 6.
The simulated scattering coefficient S_{21} responses of the modeled DGS BPF depicted in Figure 5(a) with the gap width, D, as a parameter.
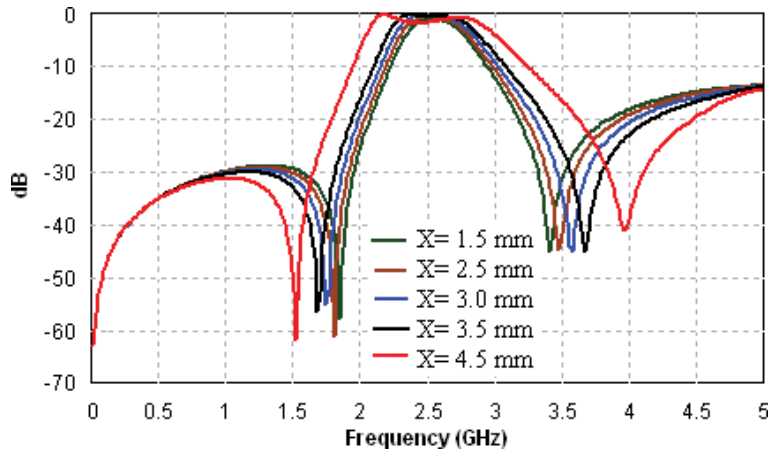
Figure 7.
The simulated scattering coefficient S_{21} responses of the modeled DGS BPF depicted in Figure 5(a) with the inter-resonator spacing, X, as a parameter.
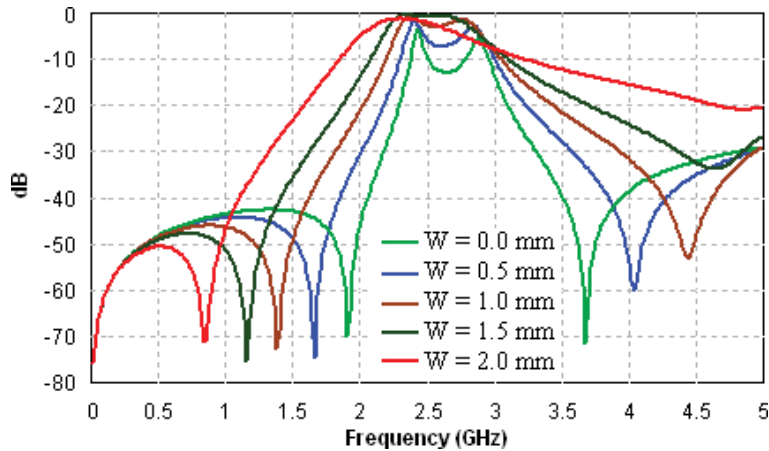

Figure 8.
The simulated scattering coefficient S_{21} responses of the modeled DGS BPF depicted in Figure 5(a) with the distance between the longitudinal filter center and the transmission line lower edge, W, as a parameter.

the defected ground structure, an improvement of the resonant filter responses will take place. Best performance has found at $W = 1.5$ mm, $X = 2.5$ mm, and $D = 1.0$ mm.

5.2 The first iteration fractal DGS BPF

An analogous investigation is performed to explore the effects of the parameters D, X, and W of this filter on its performance.

In this study, the side length of the fractal-based defected ground structure of this filter is kept the same as in Section 5.1. The additional length, that is made available by the application of the first iteration fractal resonator, causes the resulting BPF to resonate at a lower frequency. The S_{21} responses imply that this BPF resonates at 1.61 GHz. A comparison of the DGS BPF responses, those of this filter, reveals that this filter offers a size reduction of about 65%.

In addition to the size miniaturization offered by this filter, the resonant responses show that it overperforms that with the conventional DGS. This filter

provides an improved selectivity. The impacts of the modification of the parameters D, X, and W on the filter S_{21} responses are correspondingly demonstrated in **Figures 9–11**.

In summary, the resonant responses shown in **Figures 9–11** imply that this filter offers a most favorable resonant performance when the parameters W = 2.25 mm, X = 2.0 mm, and D = 0.25 mm. This filter provides a resonant response with a center frequency of 1.61 GHz. The resonant response is symmetrical about the center frequency. The results also reveal that the filter resonant response shows two transmission zeros located at 1.33 and 2.15 GHz. Furthermore, the resonant filter behavior is characterized by a steeper response with higher roll-off rates of 132.74 and 94.81 dB/GHz, at the lower and the upper edges of the passband, respectively. More interesting, this BPF provides an extra rejection level in the stopband when compared with that offered by the filter depicted in Section 5.1.

5.3 The second iteration fractal DGS BPF

The resonant behavior of this filter has also been studied under the impacts of varying the same parameters on its overall performance.

In this context, it has been that this filter possesses the optimal performance among those examined in Sections 5.1 and 5.2. The filter scattering coefficient, S_{21}, responses under the influence of the variation of the parameters D, X, and W are demonstrated in **Figures 12–14**, respectively. It is apparent from these responses that this band-pass filter overperforms the other two BPFs in several aspects that this filter presents the maximum selectivity and the top rejection level in the stopband.

Examining the resonant characteristics of this filter, it has an exciting performance with a steep roll-off in its in-band response. The –40 dB lower edge roll-off rate of the passband is of 197.70 dB/GHz and that of the upper edge is of 180.04 dB/GHz. Also, the resonant response shows that it has two transmission zeros almost symmetrically positioned about the center frequency. These transmission zeros are placed at 1.32 and 1.87 GHz. More interestingly, the filter performance responses reveal that it does not support the higher harmonics. Besides, according to [27, 28], the locations of the transmission zeros, in the filter response, are immensely influenced by the equivalent capacitance of the defected ground structures. Consequently, the improvement of the selectivity of this filter can be clarified as follows. When applying iteration levels, the incorporated length will become
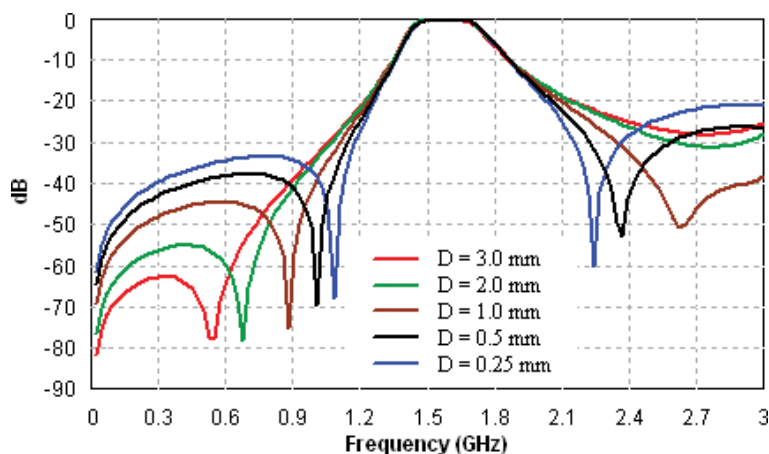

Figure 9.
The simulated scattering coefficient S_{21} responses of the modeled DGS BPF depicted in Figure 5(b) with the gap width, D, as a parameter.
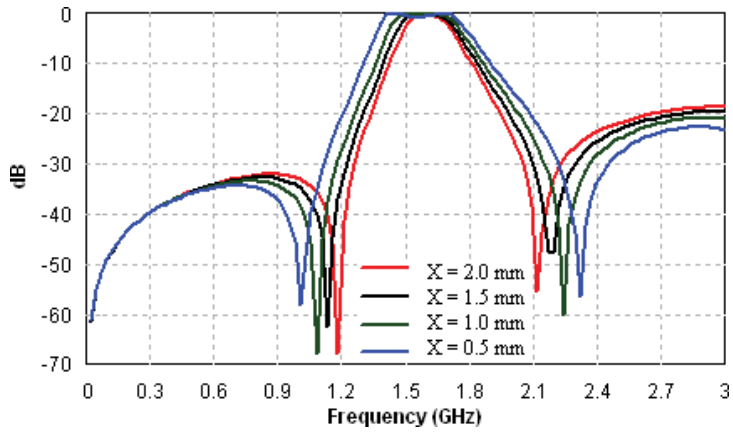
Figure 10.
The simulated scattering coefficient S_{21} responses of the modeled DGS BPF depicted in Figure 5(b) with the inter-resonator spacing, X, as a parameter.

Figure 11.
The simulated scattering coefficient S_{21} responses of the modeled DGS BPF depicted in Figure 5(b) with the distance between the longitudinal filter center and the transmission line lower edge, W, as a parameter.

Figure 12.
The simulated scattering coefficient S_{21} responses of the modeled DGS BPF depicted in Figure 5(c) with the gap width, D, as a parameter.

Figure 13.
The simulated scattering coefficient S_{21} responses of the modeled DGS BPF depicted in Figure 5(c) with the inter-resonator spacing, X, as a parameter.
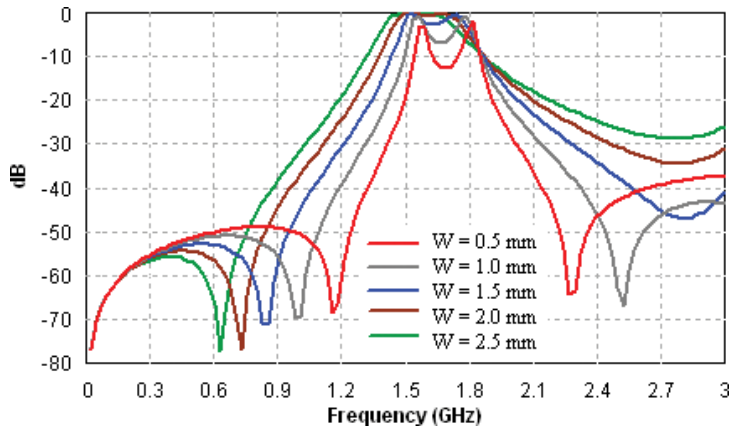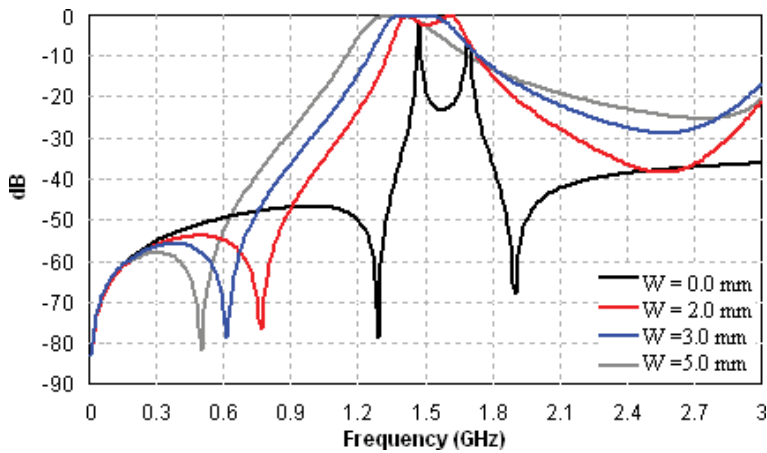

Figure 14.
The simulated scattering coefficient S_{21} responses of the modeled DGS BPF depicted in Figure 5(c) with the distance between the longitudinal filter center and the transmission line lower edge, W, as a parameter.
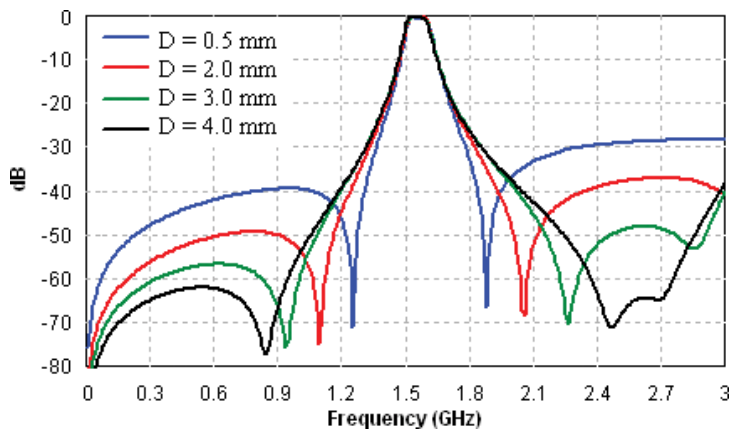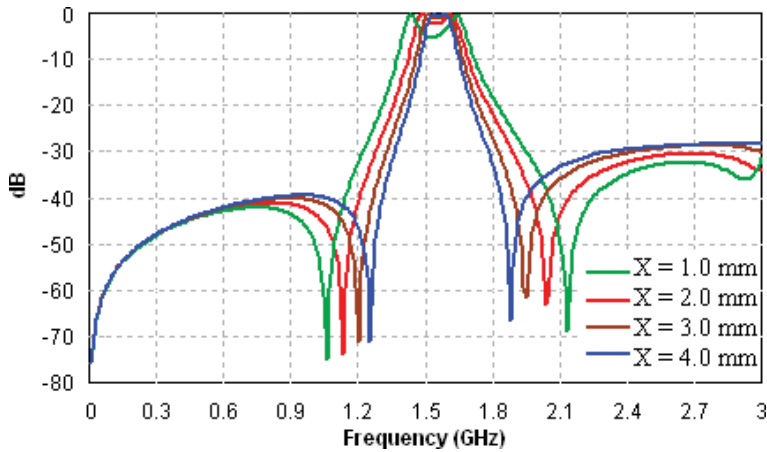

Figure 15.
The current distributions on the surface of the ground plane of the filter at different frequencies in the resonant band and outside it.

larger. The resulting substructures of the fractal-based resonators approach each other, leading to the existence of a capacitive coupling which, in turns, enhances the final filter skirt characteristics at both sides.

What is more, to offering an additional physical clarification about the electromagnetic aspects of the modeled band-pass filter, the current distributions on its 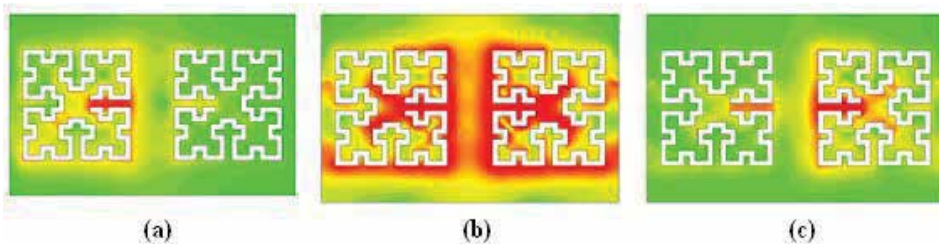surface have been simulated at different frequencies in the resonant band and outside it. **Figure 15(a)–(c)** illustrate the surface current distributions at 1.30, 1.55, and 1.70 GHz which represent the frequencies in the lower stopband, in the passband, and in the upper stopband, respectively. **Figure 15** exhibits the current distributions on the surfaces of the ground plane of the modeled BPF structure. **Figure 15(a)** and **(c)** indicates that there is no coupling taking place between the resonators in the lower stopband and the upper stopband. On the other hand, the large current densities, exposed in **Figure 15(b)**, represent an indication of the strong coupling which results in the conclusive resonance. It is apparent that the majority of the resonator length plays a role in causing the resonance.

6. Comparison with other fractal-based filter models

In this chapter, the modified Minkowski fractal geometry has been adopted to design the proposed BPF filter. The modified Minkowski fractal geometry is with better space-filling property to achieve more miniaturization as compared with the conventional Minkowski fractal geometry. However, an attempt has been carried out to compare the performance of the proposed filter with those modeled using other fractal geometries with high space-filling properties.

For this purpose, Peano and Moore fractal geometries have been adopted to design two BPFs based on the presented design idea. In the modeling of the proposed BPF filters, the same substrate and the same resonator dimensions are used. **Figures 16** and **17** illustrate the filter structures together with their performance
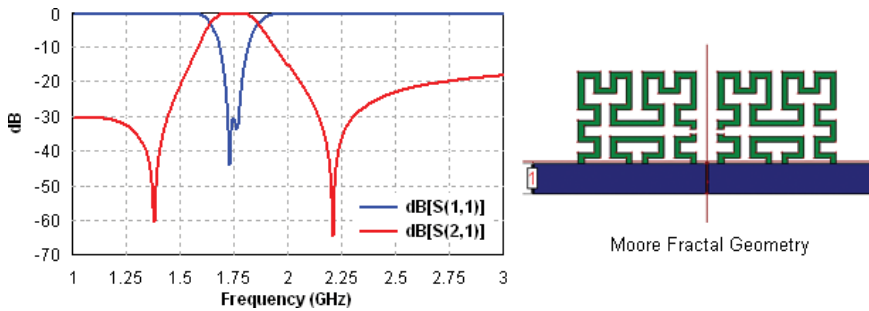

Figure 16.
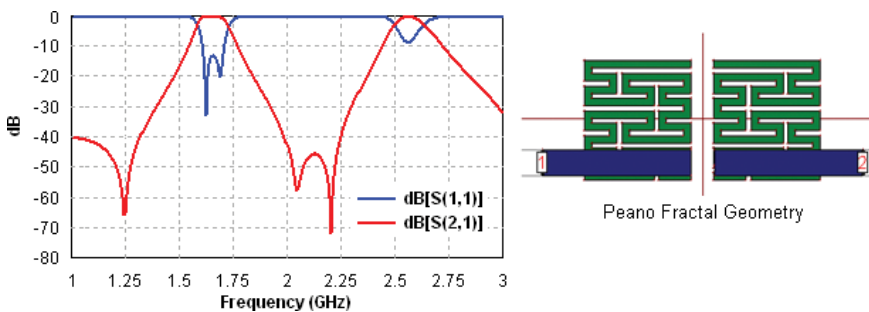*Moore fractal-based DGS BPFs together with performance responses.*

Figure 17.
*Peano fractal-based DGS BPFs together with performance responses.*

responses. It is clear that both filters offer resonant responses at a higher frequency than that provided by the Minkowski fractal-based BPF. This means that the Minkowski fractal-based BPF possesses a higher size reduction. It is worth to note that the BPF based on Peano fractal geometry offers dual-band resonant response which can be tuned to a certain extent by the filter elements. However, further investigation of this filter has to be conducted later.

7. Fabricated model and the measured results

A prototype of the fractal-based defected ground structure band-pass filter has been manufactured. The fabricated prototype uses an identical substrate with a relative permittivity of 2.65 and thickness of 1.0 mm. **Figure 18** shows photos of the manufactured filter. The measured and simulated scattering coefficient responses, S_{11} and S_{21}, are depicted in **Figures 19** and **20**, respectively.

The simulated and measured results of the modeled and the fabricated band-pass filters well agree with each other. Some deviation, between the measured and the simulated results, is noticed. The shift of the lower edge of the passband response of the S_{21} responses is slight, while that of the upper edge is hardly visible. Furthermore, the measured results reveal attenuation in the passband region.

The production technique might cause dimensional tolerance which, in turns, leads to the differences observed between the measured and the simulated results. Employing more advanced manufacturing methods, besides the selection of a substrate having a more stable parameter, will result in a closer agreement.
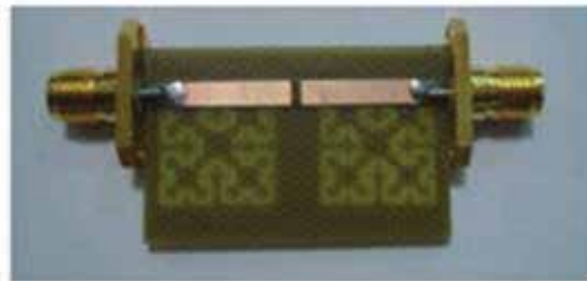
Figure 18.
Photos of the fabricated prototype (a) the top and (b) the bottom views.
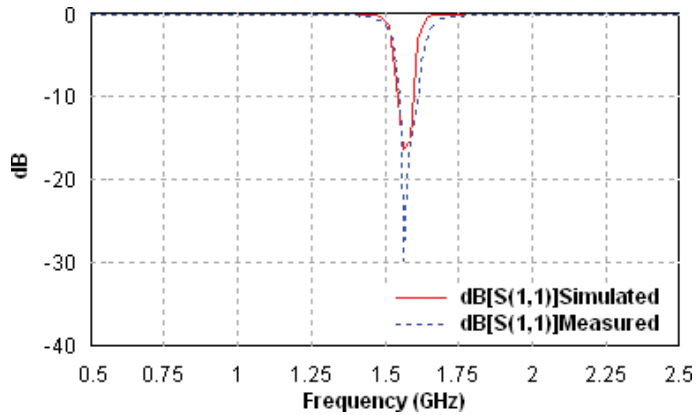
Figure 19.
The simulated and measured S_{11} responses of the fabricated filter prototype.
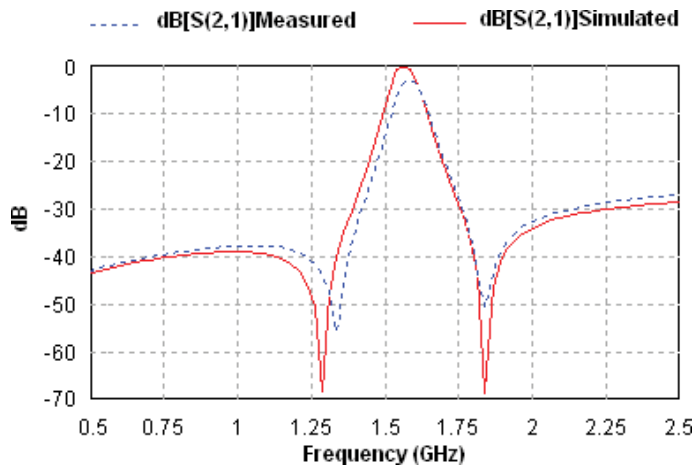
Figure 20.
The simulated and measured S_{21} responses of the fabricated filter prototype.

The resonant behaviors of the modeled band-pass filters suggested in this work have to be compared with those recently reported in the literature. **Table 2** summarizes a comparison of the performances of the presented filters which are based on the zero, first, and second iteration DGS band-pass filters with those recently reported in the literature [27, 28]. As the table implies, the comparison is carried out

Filter type	Filter size $[\lambda_g]^2$	Roll-off rate (lower edge) (dB/GHz)	Roll-off rate (upper edge) (dB/GHz)
Zero iteration DGS	0.45 × 0.23	78.51	47.10
First iteration DGS	0.30 × 0.15	132.74	94.81
Second iteration DGS	0.29 × 0.14	197.70	180.04
DGS BPF [27]	0.50 × 0.25	72.54	52.86
DGS BPF [28]	0.22 × 0.17	41.11	12.75

Table 2.
Comparison of the presented band-pass filters with those published in the literature.

concerning the occupied areas and the filter selectivity which in turns is expressed by the roll-off rates at the lower and the upper edges. In spite of the extra miniaturization of the second iteration, fractal-based DGS band-pass filter is minor, but this BPF possesses the most excellent selectivity, among the others, regarding the lower and the upper edges roll-off rates. However, the realized size by each BPF has been calculated in terms of the guided wavelength, λ_g, computed at the lower resonant frequency. Even though the DGS band-pass filter reported in [28] is approximately equivalent in the occupied area with that suggested in this work, it suffers from poor selectivity. It has poor upper edge roll-off rate and low selectivity in the lower edge roll-off rate.

8. Conclusions

The defected ground structure resonator based on the Minkowski fractal variant reported in this chapter has confirmed its capability to produce reduced size microstrip band-pass filters. Besides the acceptable resonant responses of the suggested BPFs, the adoption of the Minkowski fractal geometry to the defected ground structure resonator bring about BPF designs with considerable miniaturization with reference to those recently published in the literature. As expected, the results showed that more filter size miniaturization could be obtained when employing higher fractal orders. In the real practice, this might not be the situation; several restrictions are coming across the practical implementation of a filter prototype, especially for the higher iteration levels. Also, the results revealed that the proposed BPF performances are characterized by a low loss in the passband and high rejection in the stopband with considerable reduction of higher harmonics. A significant finding is that the final BPF performance possesses a high selectivity with steep roll-off rates at both the lower and the upper edges of the passband. A comparison of the performance of the DGS BPF based on the modified Minkowski fractal geometry with other filters based on Peano and Hilbert fractal geometries revealed that the proposed BPF has acceptable resonant responses with a significant lessening of higher harmonics. Measured results of a fabricated prototype well agree with those evaluated by the EM simulator. The presented BPF resonant characteristics, besides the considerable size miniaturization, will make it an appropriate candidate for the application in a broad diversity of the modern wireless communication services.

Conflict of interest

The authors declare there are no conflicts of interest regarding the publication of this book chapter.

Author details

Hadi T. Ziboon and Jawad K. Ali*
Microwave Research Group, Department of Electrical Engineering, University of Technology, Iraq

*Address all correspondence to: jawadkali@theiet.org

IntechOpen

References

[1] Cohen N. Fractal antenna and fractal resonator primer. Chapter 8. In: Rock JA, van Frankenhuijsen M, editors. Fractals and Dynamics in Mathematics, Science, and the Arts: Theory and Applications. Vol. 1. World Scientific Publishing, USA; 2015

[2] Ali JK, Ahmed ES. A new fractal based printed slot antenna for dual band wireless communication applications. In: Proceedings of Progress in Electromagnetics Research Symposium, PIERS 2012; Kuala Lumpur, Malaysia; 2012. pp. 1518-1521

[3] Ali JK, Jalal ASA. A miniaturized multiband Minkowski-like pre-fractal patch antenna for GPS and 3g IMT-2000 Handsets. Asian Journal of Information Technology. 2007;**6**(5):584-588

[4] Ali JK, Yassen MT, Hussan MR, Salim AJ. A printed fractal based slot antenna for multi-band wireless communication applications. In: Proceedings of Progress in Electromagnetics Research Symposium, PIERS 2012; Moscow, Russia; 2012. pp. 618-622

[5] Mezaal YS. New compact microstrip patch antennas: Design and simulation results. Indian Journal of Science and Technology. 2016;**9**(12):1-6. DOI: 10.17485/ijst/2016/v9i12/85950

[6] Abdulkarim SF, Salim AJ, Ali JK, Hammoodi AI, Yassen MT, Hussan MR. A compact Peano-type fractal based printed slot antenna for dual-band wireless applications. In: 2013 IEEE International RF and Microwave Conference, RFM 2013; Penang, Malaysia; 2013. pp. 329-332

[7] Ali JK, AL-Hussain ZAA, Osman AA, Salim AJ. A new compact size fractal based microstrip slot antenna for GPS applications. In: Proceedings of Progress in Electromagnetics Research Symposium, PIERS 2012; Kuala Lumpur, Malaysia; 2012. pp. 700-703

[8] Ali JK, Abdulkareem SF, Hammoodi AI, Salim AJ, Yassen MT, Hussan MR, et al. Cantor fractal based printed slot antenna for dual band wireless applications. International Journal of Microwave and Wireless Technologies. 2016;**8**(02):263-270

[9] Ghiyasvand M, Bakhtiari A, Sadeghzadeh RA. Novel microstrip patch antenna to use in 2×2 sub arrays for DBS reception. Indian Journal of Science and Technology. 2012;**5**(7):2967-2971. DOI: 10.17485/ijst/2012/v5i7/30493

[10] Ye CS, Su YK, Weng MH, Wu HW. Resonant properties of the Sierpinski-based fractal resonator and its application on low-loss miniaturized dual-mode bandpass filter. Microwave and Optical Technology Letters. 2009;**51**:1358-1361

[11] Weng MH, Jang LS, Chen WY. A Sierpinski-based resonator applied for low loss and miniaturized bandpass filters. Microwave and Optical Technology Letters. 2009;**51**(2):411-413

[12] Mezaal YS, Eyyuboglu HT, Ali JK. New microstrip bandpass filter designs based on stepped impedance Hilbert fractal resonators. IETE Journal of Research. 2014;**60**(3):257-264

[13] Mezaal YS, Ali JK, Eyyuboglu HT. Miniaturised microstrip bandpass filters based on Moore fractal geometry. International Journal of Electronics. 2015;**102**(8):1306-1319

[14] Ali JK, Miz'el YS. A new miniature Peano fractal-based bandpass filter design with 2nd harmonic suppression. In: Proceedings of 3rd IEEE International Symposium on Microwave, Antenna, Propagation and EMC Technologies for Wireless Communications; Beijing, China; 2009. pp. 1019-1022

[15] Ali JK, Mezaal YS. A new miniature narrowband microstrip bandpass filter

design based on Peano fractal geometry. Iraqi Journal of Applied Physics. 2009;**5**(4):3-9

[16] Ali JK, Alsaedi H, Hasan MF, Hammas HA. A Peano fractal-based dual-mode microstrip bandpass filters for wireless communication systems. In: Proceedings of Progress in Electromagnetics Research Symposium, PIERS; Moscow, Russia; 2012. pp. 888-892

[17] Mezaal YS, Eyyuboglu HT, Ali JK. A new design of dual band microstrip bandpass filter based on Peano fractal geometry: Design and simulation results. In: Proceedings of the 13th IEEE Mediterranean Microwave Symposium, MMS'2013; Saida, Lebanon; 2013. pp. 1-4

[18] Ali JK. A new miniaturized fractal bandpass filter based on dual-mode microstrip square ring resonator. In: Proceedings of the 5th International Multi-Conference on Signals, Systems and Devices, IEEE SSD '08; Amman, Jordan; 2008. pp. 1-5

[19] Ali JK, Hussain NN. A new fractal microstrip bandpass filter design based on dual-mode square ring resonator for wireless communication systems. Iraqi Journal of Applied Physics. 2009;**5**(1):7-14

[20] Ali JK, Hussain NN. An extra reduced size dual-mode bandpass filter for wireless communication systems. In: Proceedings of Progress in Electromagnetics Research Symposium, PIERS 2011; Suzhou, China; 2011. pp. 1467-1470

[21] Liu JC, Liu HH, Yeh KD, Liu CY, Zeng BH, Chen CC. Miniaturized dual-mode resonators with Minkowski-island-based fractal patch for WLAN dual-band systems. Progress in Electromagnetics Research C. 2012;**26**:229-243

[22] Lalbakhsh A, Neyestanak AAL, Naser-Moghaddasi M. Microstrip hairpin bandpass filter using modified Minkowski fractal-shape for suppression of second harmonic. IEICE Transactions on Electronics. 2012;**E95C**(3):378-381

[23] Chen J, Weng ZB, Jiao YC, Zhang FS. Lowpass filter design of Hilbert curve ring defected ground structure. Progress in Electromagnetics Research. 2007;**70**:269-280

[24] Liu HW, Li ZF, Sun XW. A novel fractal defected ground structure and its application to the low-pass filter. Microwave and Optical Technology Letters. 2003;**39**:453-456

[25] Alqaisy M, Chakrabraty C, Ali JK, Alhawari ARH. A miniature fractal-based dual-mode dual-band microstrip bandpass filter design. International Journal of Microwave and Wireless Technologies. 2015;7:127-133

[26] Li TP, Wang GM, Lu K, Xu HX, Liao ZH, Zong B. Novel bandpass filter based on CSRR using Koch fractal curve. Progress in Electromagnetics Research Letters. 2012;**28**:121-128

[27] Boutejdar A, Ibrahim AA, Burte EP. DGS resonators form compact filters. Microwaves and RF. 2015;**54**(3):52-60

[28] Boutejdar A, Elsherbini A, Balalem A, Machac J, Omar A. Design of new DGS hairpin microstrip bandpass filter using coupling matrix method. In: Proceedings of Progress in Electromagnetics Research Symposium, PIERS 2007; Prague, Czech Republic; 2007. pp. 261-265

[29] Falconer K. Fractal Geometry: Mathematical Foundations and Applications. Wiley & Sons, West Sussex, England; 2004

[30] Ziboon HT, Ali JK. Minkowski fractal geometry: An attractive choice of compact antenna and filter designs. ARPN Journal of Engineering and Applied Sciences. Accepted, 2018

[31] Ali JK, Ziboon HT. Design of compact bandpass filters based on fractal defected ground structure (DGS) resonators. Indian Journal of Science and Technology. 2016;**9**(39):1-9. DOI: 10.17485/ijst/2016/v9i39/91350

[32] IE3D User's Manual, Release 12.3. Fremont, CA: Zeland Software, Inc.; 2007

[33] Hong JS. Microstrip Filters for RF/ Microwave Application. New York: Wiley; 2001

[34] Wang J, Xu LJ, Zhao S, Guo YX, Wu W. Compact quasi-elliptic microstrip lowpass filter with wide stopband. Electronics Letters. 2010;**46**(20):1384-1385

[35] Li JL, Qu SW, Xue Q. Compact microstrip lowpass filter with sharp roll-off and wide stop-band. Electronics Letters. 2009;**45**(2):110-111

[36] Hayati M, Naderi S, Jafari F. Compact microstrip lowpass filter with sharp roll-off using radial resonator. Electronics Letters. 2014;**50**(10):761-762

Chapter 4

Fractal Antennas for Wearable Applications

Mohamed I. Ahmed and Mai F. Ahmed

Abstract

This chapter focuses on the design and fabrication of different types of flexible and inflexible wearable fractal for modern wireless applications with body-area-networks (BANs). A wearable antenna is intended to be a part of clothing used for modern wireless communication purposes. Fractal technology allowed us to design compact antennas and integrate multiple communication services into one device. The proposed antennas were simulated and measured by CST simulator version 2017 and Agilent N9918A VNA respectively. Furthermore, these antennas were fabricated using folded copper. The measured results agree well with the simulated results.

Keywords: fractal, wearable antenna, metamaterial, SAR, Sierpinski carpet, crown rectangular, textile antenna

1. Introduction

Conventional antenna designs which include planar dipoles, monopoles, planar inverted-Fs (PIFAs), and microstrip patches were used in recent research for wearable antennas design [1]. Wearable microstrip antennas are planar. This made them a practical antenna type due to their low cost, low profile, light weight, small size and eases for fabrication to be worn or carried on human body [2]. A wearable antenna is a body-worn antenna which designed from textile materials as antenna substrates to form the "smart clothes" or in the other mean, is an antenna which designed and meant to be a part of clothing or integrated into a personal accessory (such as shoes, glasses, buttons, and helmets) [3]. The wearable antennas are divided into two main categories: flexible and inflexible wearable antennas [4].

Nowadays, the compact antenna with a better performance and multi-bands working frequencies is one of the main trends in modern wireless communications systems [5]. One of the most important techniques used to reduce the antenna's dimensions is the fractal geometries. A fractal is a fragmented or split geometric shape that can be subdivided into parts; each of this is a reduced-size copy of the whole. Fractal antennas have more benefits such as; high radiation efficiency, high gain, wide bandwidth and reduced size etc. Generally, fractals are self-similar and independent of scale. There are many shapes of fractals such as Sierpinski's gasket; Cantor's comb, Von Koch's snowflake, the Mandelbrot set, and the Lorenz attractor see **Figure 1** [6].

Figure 1.
The different geometries of fractals in natural [6].

1.1 Wearable antennas design steps

1.1.1 Material selection

The fabrication process of flexible and wearable antennas depends mainly on the materials involved in the designed structure. Properties of conductive and dielectric materials used in flexible and wearable antennas, are surveyed in this section [7].

1.1.2 Dielectric materials

Dielectric materials that are used as substrates for antennas, these materials may be inflexible such as conventional soft PCB or flexible such as textile material in clothing. The textile materials must be it is flexible, easy to design, water resistant and light in weight to make the wearable antenna more suitable [8].

1.1.3 Conductive materials

Conductive materials may be pure metallic materials or electro-textile materials. The pure metallic material is pasted on the dielectric substrate which is made out of different materials such as: copper, gold and etc. The electro-textile materials are conductive fabrics [9].

1.2 Antenna design

In general, to design any rectangular wearable microstrip patch antenna should be considered the following parameters such as dielectric constant (ε_r), resonant frequency (f_o), and height of the substrate (h) for calculating the length and the width of the patch [10].

1.3 Antenna simulation

There are several technologies and simulators for analysis and simulation the wearable antennas. CST MICROWAVE STUDIO is a computer system technology and is a numerical simulator which uses the finite integration technique (FIT) [11].

1.4 Performance near human

Generally, wearable antenna or body-worn antenna radiates the electromagnetic waves (EMWs) which are absorbed by tissues of the human body. The

absorption of these waves will cause damage and burn human tissues [12]. So that it is necessary to decrease the electromagnetic energy interaction towards the human body tissue from the wearable antennas when in use [13]. The absorption of the electromagnetic waves (EMWs) from the human tissue is measured by the specific absorption rate (SAR) [14]. Therefore, the SAR value plays a vital role in any design of wearable antenna. There are some parameters which will effect on the SAR value such as: size, shape, location, radiated power and type of antenna used and etc. in [15, 16].

1.4.1 The SAR safety limitation

The SAR safety limit is based on the standardization committee and is various in different regions in over the world. In the US is regulated by the Federal Communications Commission (FCC) where the acceptable maximum SAR value 1.6 W/kg, averaged over 1 gram of tissue [17]. But in Europe, the acceptable maximum SAR value is 2.0 W/kg averaged over 10 grams of tissue which is regulated by the International Commission on Non–Ionizing Radiation Protection (ICNIPR) [17]. If the SAR value exceeds the safety limit, the antenna must be changed and replaced by antenna with a lower back radiation [18].

1.5 Applications of wearable microstrip antenna

The development of antenna technology for human and machine interface has made qualitative leaps in the use of textiles as antenna substrates [19]. In future, this will permit freedom to design antenna systems worn by the body and integrated into it so; these are called "smart clothes" [20]. They will emerge in various as shown in **Figure 2** [21]:

1. Emergency workers outfits.

2. Medical applications.

3. Space applications.

4. Military applications.

5. Sports outfits and so forth.

Figure 2.
The various applications of the wearable antenna [21].

2. Fractal wearable antenna on metamaterial cell

2.1 Fractal wearable antenna design

The simulated geometry of the proposed fractal wearable antenna is illustrated in **Figure 3**. The patch and the ground planes are squares with length = 46 mm, and 70 mm respectively. The substrate is made from FR4 material with thickness h = 1.6 mm, relative permittivity ε_r = 4.4 and tan (δ) = 0.02.

The inset fed line of the proposed antenna is consisted of two sections: 50 Ω stripline and tapered line for achieving the 50 Ω impedance matching as shown in **Figure 4**. The port dimensions are tabulated in **Table 1**.

The proposed third iteration fractal antenna is designed based on an iteration length, Lm. It is calculated as follows [22]:

$$L^m = 2L^{m+1} + W1^{m+1} + 2W2^{m+1} \quad (14).$$

Where: m is the order of iteration, $W1^{m+1} = c_1L^m$; is the width of the middle segment, and $W2^{m+1} = c_2L^m$; is the indentation width.

Furthermore, Parameters c_1 and c_2, are very important parameters for the efficiency of the size reduction [22]. Now, in the presented fractal wearable antenna c_1 and c_2 are chosen as 0.1 and 0.4 respectively. This antenna is designed to be suitable for operating in GPS, WiFi like Bluetooth, and WiMax frequencies at the time as shown in **Figure 5**.

In addition to, a metamaterial spiral cell is meandered in the ground plane of the presented 3[rd]iteration fractal wearable antenna for enhancement the SAR results (as shown in **Figure 6**). By using this spiral cell, the permeability and the permittivity will be negative, and then the reflection coefficient will be also negative, so that the SAR value is minimized.
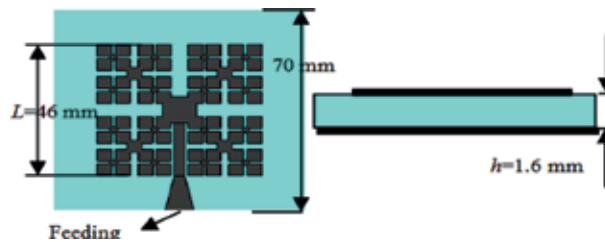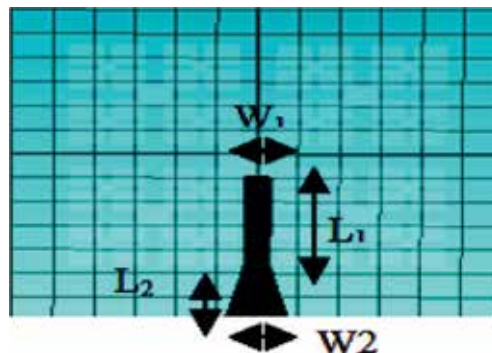

Figure 3.
The geometry of proposed antenna.

Figure 4.
The port geometry.

Parameter	W1	L1	W2	L2
Value (mm)	3	18.4	8	12

Table 1.
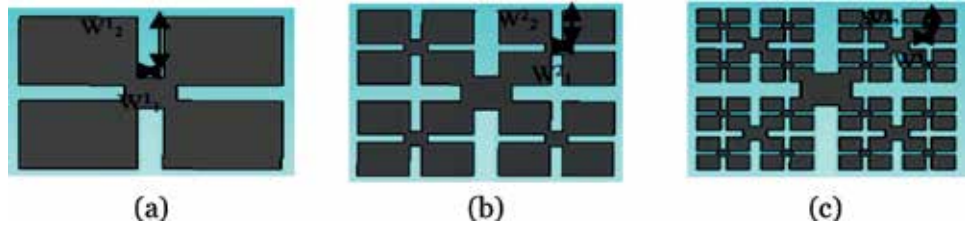*Strip-Line Dimensions.*

Figure 5.
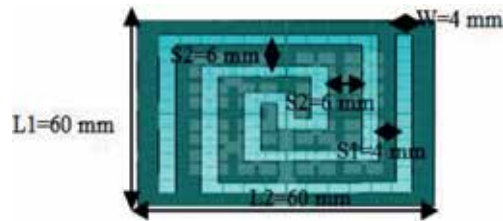*The proposed fractal antenna with different iteration structures.*

Figure 6.
The geometry of spiral cell.

2.2 Simulation results

Simulation analysis of the proposed antennas is performed through the commercial software simulator called CST 2016. The simulated S_{11} for the conventional patch, 1st iteration, 2nd iteration, and the 3rd iteration of the Fractal Wearable Antenna are shown in **Figure** 7. Also, the antenna radiation patterns with/without spiral cell in E-plane and H-plane are plotted in **Figures** 8 and **9**.

For the four resonance frequency bands, the gain and efficiency are improved by using metamaterial spiral cell. The first band with return loss −23 dB from 1.54 to1.62 GHz, this band is suitable for GPS application. In this band, the gain and efficiency are 2.152 dB and 44.7% and improved with MTM spiral cell to 4.41 dB and 79.1%. The second band with return loss −20.78 dB from 2.67 to 2.87 GHz, this band
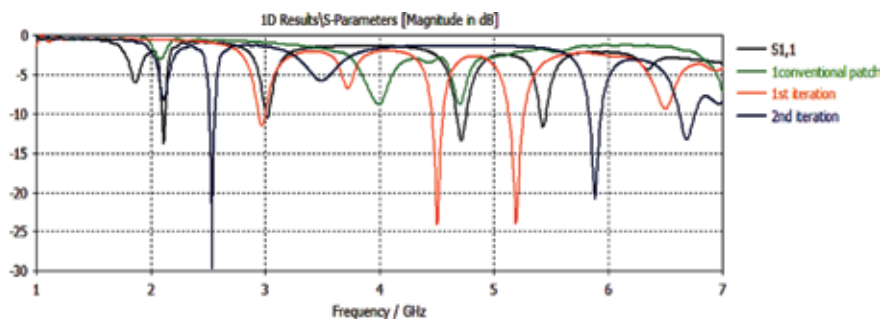

Figure 7.
The S11 against frequency for three different iterations.
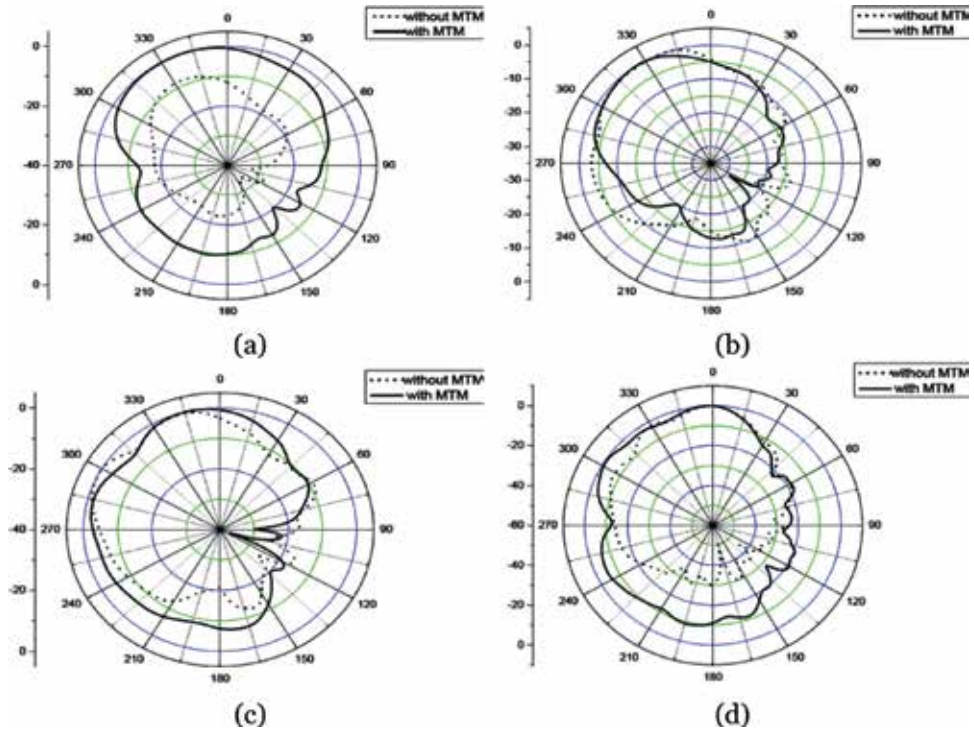
Figure 8.
Radiation pattern in E-plane at (a) 1.57, (b) 2.7, (c) 3.4 (d) 5.3 GHz.

is suitable for WiMax application. In this band, the gain and efficiency are 1.19 dB and 47.2% and improved to 3.56 dB and 55.54%. The third band with return loss −9.67 dB from 3.33 to 3.46 GHz, this band is suitable also for WiMax application. In this band, the gain and efficiency are 1.112 dB and 56.6% and improved to 2.89 dB
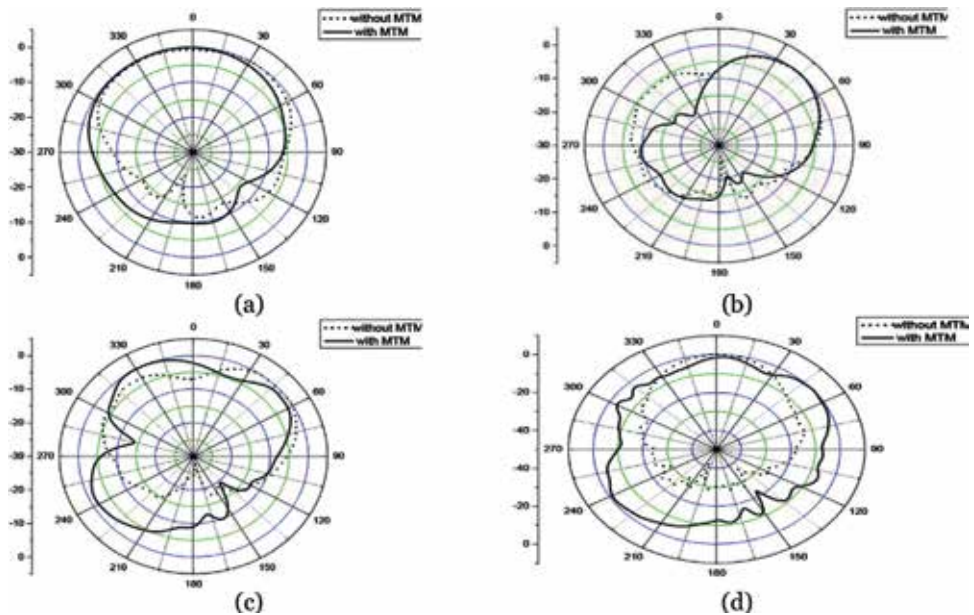

Figure 9.
Radiation pattern in H-plane at (a) 1.57, (b) 2.7, (c) 3.4 and (d) 5.3 GHz.
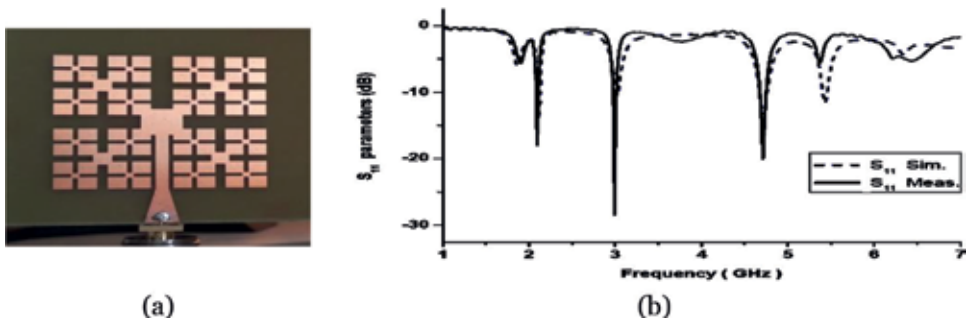
Figure 10.
The fabricated proposed antenna without MTM cell: (a) fabricated geometry, and (b) the measured and simulated return loss S11 with the frequency.
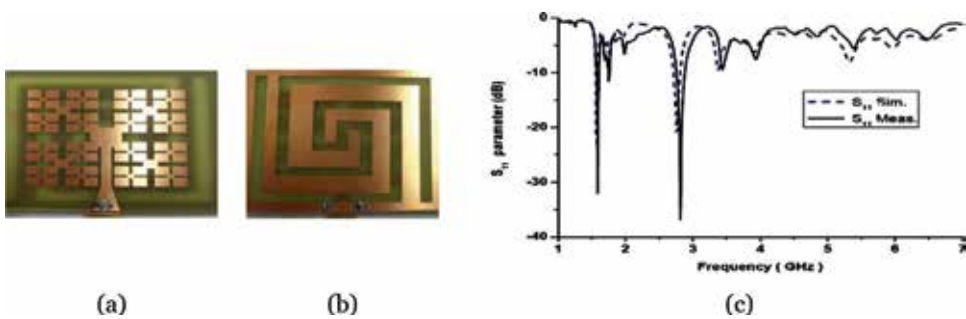

Figure 11.
Fabricated proposed antenna with MTM cell: (a) top and (b) bottom view and (c) the measured and simulated return loss S11 with the frequency.

and 67.45%. The forth band with return loss −8.56 dB from 5.24 to 5.42 GHz, this band is suitable for WiFi application. In this band, the gain and efficiency are 2.29 dB and 58.5% and improved to 3.38 dB and 68.1%.

2.3 Experimental results and discussion

The prototypes of the proposed fractal antenna without and with spiral cell and the measured S11 for those are shown in **Figures 10** and **11**.

2.4 SAR calculations

Figure 12 shows that the SAR simulation results for the proposed antenna with spiral MTM cell. These results are shown in **Figure 13** and mentioned in **Table 2**. From **Figure 13** and **Table 2**, the intended four bands have a very low SAR value and do not exceed unity. Also, can be notes as the distance between the proposed antenna and the human is maximized, the SAR value is minimized.

2.5 Proposed antenna integrated on life jacket as application

In this section, the presented 3rd iteration fractal wearable antenna with MTM spiral cell is used for integration on a floating life jacket. This smart life jacket can be used to help humans get away in the event of an accident [23]. Also, there is another benefit for using that life jacket; it can be used as an isolation cover to prevent the

water reaching the proposed antenna. The simulated life jacket with voxel model is shown in **Figure 14**, and the dimensions with some electrical characteristics of that simulated life jacket are tabulated in **Table 3**.

Figure 12.
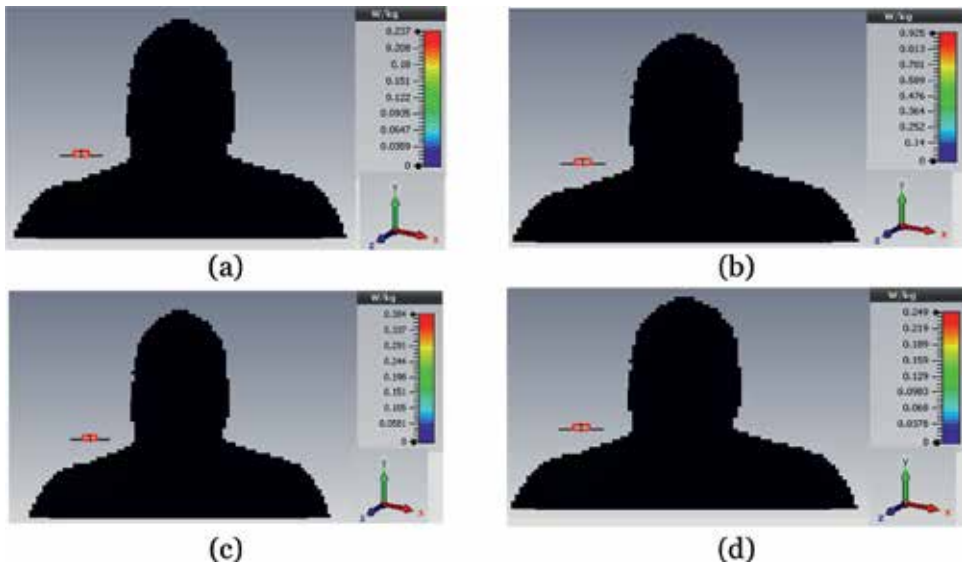*SAR distribution at (a) 1.57, (b) 2.7, (c) 3.4 and (d) 5.3 GHz.*
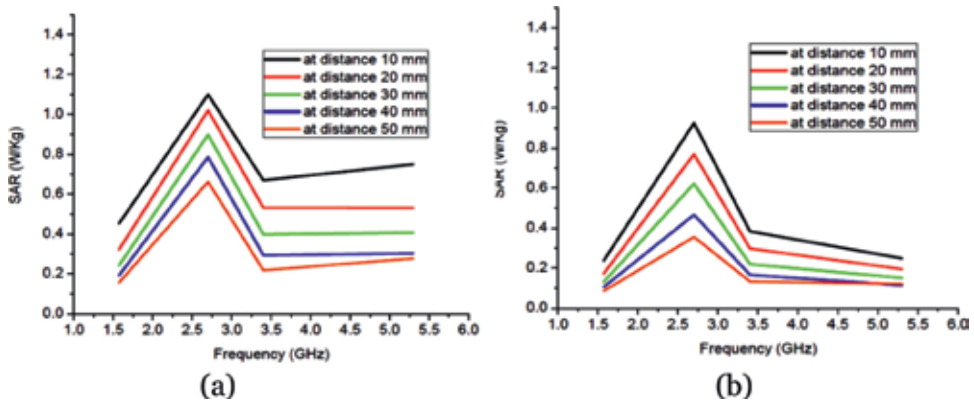
Figure 13.
Maximum SAR values by two standard: (a) FCC, and (b) ICNIRP.

Resonance frequency (GHz)	SAR (W/kg)	
	1 g	**10 g**
1.57	0.452	0.237
2.7	1.02	0.925
3.4	0.67	0.384
5.3	0.75	0.249

Table 2.
Max. SAR values for the proposed antenna with spiral cell.
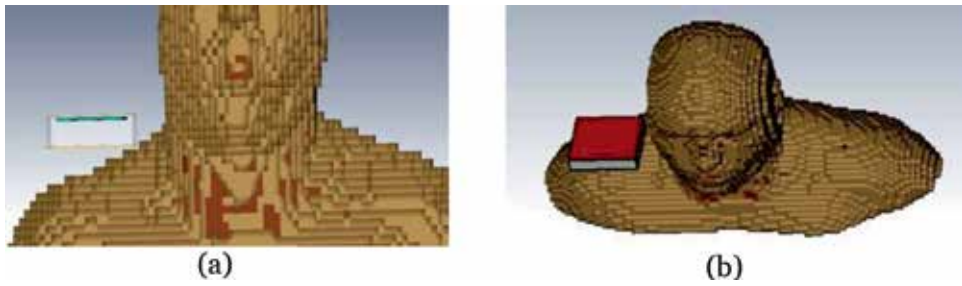
Figure 14.
The simulated life jacket attached to the proposed antenna with voxel model: (a) front and (b) top views.

Layer type	Rubber	Air
Layer thickness (mm)	1.9	20
Dielectric constant (εr)	3	1
Tangent loss (σ)	0.0025	0.002

Table 3.
Dimensions of simulated life jacket with some electrical characteristics.
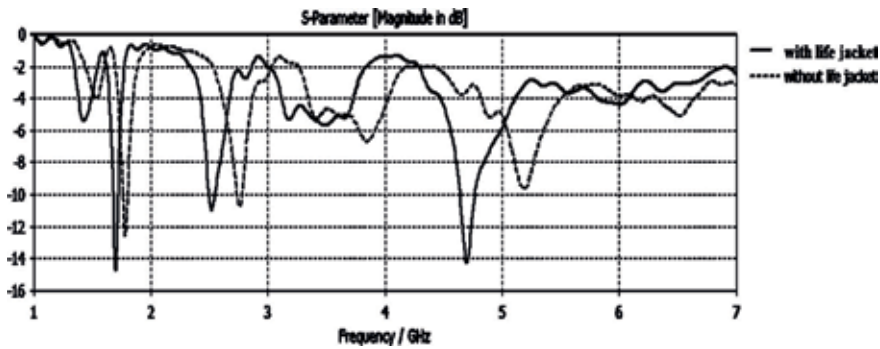
Figure 15.
Simulated S11 for the presented antenna with/without life jacket.

Resonance frequency (GHz)	Gain (dB)	Efficiency (%)
1.57	1.11	67.3
2.7	2.89	51.2
3.4	1.65	62.3
5.3	2.42	63.4

Table 4.
The simulation results of the proposed antenna with life jacket.

The simulated S_{11} for the presented wearable fractal antenna with and without the floating life jacket are shown in **Figure 15**. Furthermore, the simulated performance results for the intended antenna with the simulated floating life jacket are shown in **Table 4**.

By using the floating life jacket is as an isolation cover for the presented antenna, the SAR value is also improved as shown in **Figure 16**. The SAR simulation results are shown in **Table 5**.

Figure 16.
SAR with life jacket at (a) 1.57, (b) 2.7, (c) 3.4, (d) 5.3 GHz.

Resonance frequency (GHz)	SAR (W/kg)	
	1 g	**10 g**
1.57	0.232	0.125
2.7	0.607	0.314
3.4	0.632	0.529
5.3	0.347	0.147

Table 5.
Max. SAR values for the proposed antenna with the life jacket.

3. Sierpinski carpet wearable fractal antenna

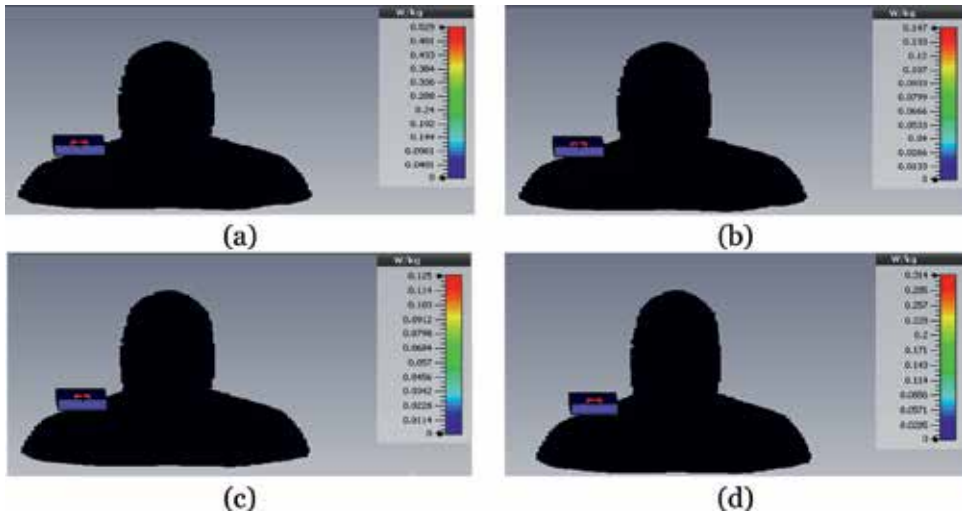The construction of Sierpinski carpet fractal antenna is more simple and easy to design. The zeroth iteration, the base shape is a square. In the base shape, the central square is removed to obtain the first iteration. In first iteration geometry, eight squares are left to design the second iteration. This procedure is repeated to obtain next iterations [24]. Furthermore, this antenna is a wearable or body-worn antenna which used Jeans textile as a substrate. Two methods for measuring the dielectric constant (ε_r) and loss tangent (tanδ) of the Jeans material were presented in this chapter: a microstrip ring resonator method [25, 26] as shown in **Figure 17** and DAK (Dielectric Assessment Kit) method [27]. The results for the two methods are tabulated in **Table 6**. Therefore, use the second method to confirm the results that were selected by using the first one. Also, the thickness of the jeans textile is 0.6 mm which measured by using screw gauge.

3.1 Fractal wearable antenna design

Figure 18 represents the geometries of the initial, first and second iterations of the Sierpinski carpet fractal wearable microstrip antenna. The optimized dimensions of the presented three antennas are indicated in **Table 7**.
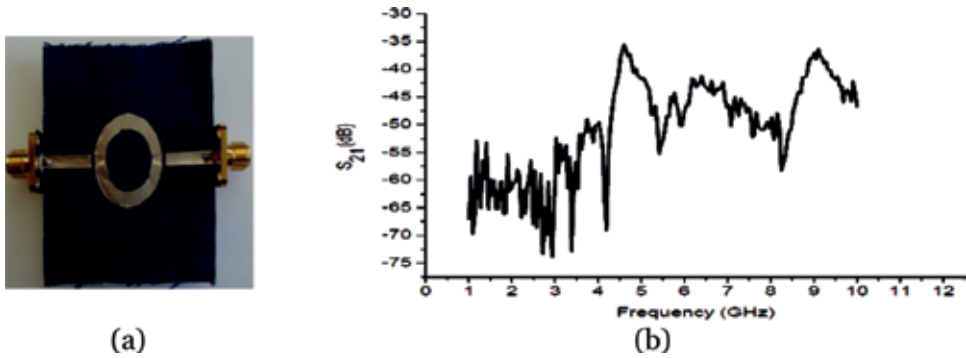
Figure 17.
(a) The fabricated ring resonator model, and (b) measured S21.

Material	The microstrip ring resonator method				
Dry jeans	**Mode**	**Resonance frequency (GHz)**	**S21 (dB)**	**Dielectric constant (εr)**	**Loss tangent (tanδ)**
	n = 1	4.26	−35.5	1.73	0.077
	n = 2	8.89	−36.9	1.69	0.073
	Dielectric assessment kit method (DAK)				
	Dielectric constant (εr)			**Loss tangent (tanδ)**	
	1.78			0.085	

Table 6.
Results of the two methods for characterization of jeans textile.
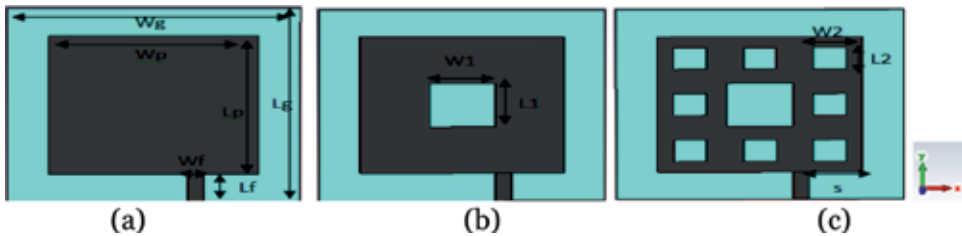
Figure 18.
Fractal antenna structures: (a) initial, (b) 1st, (c) 2nd iterations.

The fabricated geometry of the 2nd iterations Sierpinski carpet fractal wearable microstrip antenna is shown in **Figure 19a**. The simulated and measured S_{11} for the three iterations antennas are shown in **Figure 19b**. Furthermore, the radiation patterns of the proposed fractal antenna in E-plane ($\Phi = 0°$) and H-plane ($\Phi = 90°$) are simulated and plotted in **Figure 20**. From **Figure 19**, Consistent results are

	Wg	Lg	Wp	Lp	Wf	Lf	L1	W1	L2	W2	s
Value (mm)	70	70	50	50	4	10	16	16	8	8	13

Table 7.
The optimized dimensions of three iterations antenna.

Figure 19.
Proposed fractal antenna structures: initial, 1st, and 2nd iterations.
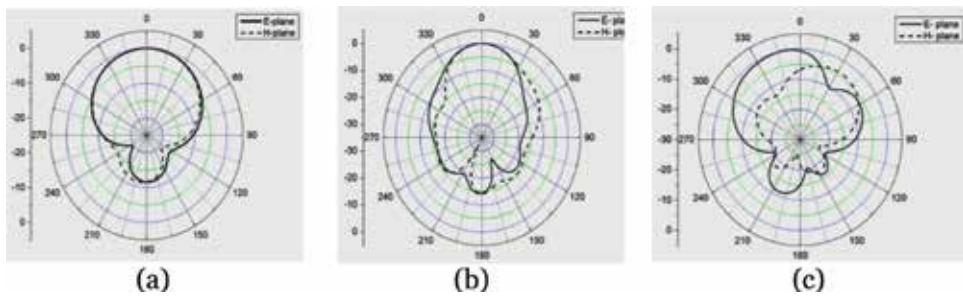
Figure 20.
Radiation pattern in E-plane, H-plane at: (a) 1.7, (b) 5.3, (c) 5.8 GHz.

Resonant Frequency (GHz)	S11 (dB)	Gain (dB)	Efficiency %
1.7	−24.719	4.5	72.6
5.3	−14.778	1.78	52.3
5.8	−19.937	4.4	67.4

Table 8.
Performance simulated results of proposed fractal antenna.

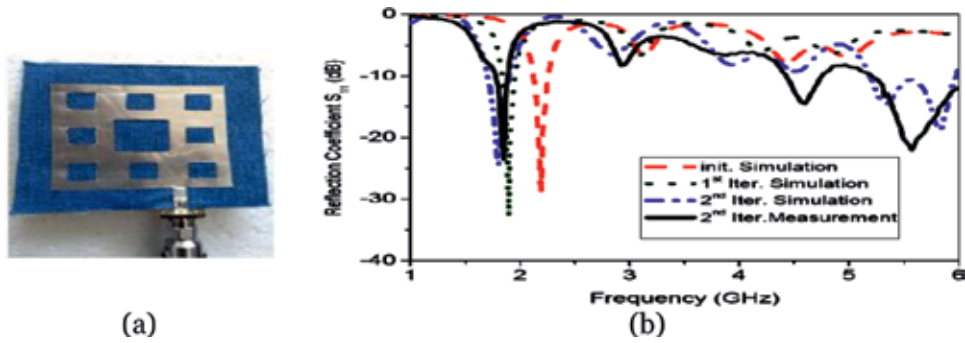measured with simulation results. Further, the proposed 2nd iteration Sierpinski carpet fractal wearable microstrip antenna can be used as a multiband antenna. This antenna is operated at three frequency bands in the same time for modern wireless applications as GPS, WiMax and WiFi. The simulation performance results are tabulated in **Table 8**.

4. Crown rectangular wearable fractal (CRWF) antenna

The third wearable fractal antenna designed in this chapter is based on the rectangular shape and is called CRWF antenna. The base geometry construction as, zeroth iteration is a rectangle. The first iteration geometry is obtained by cutting an ellipse from the base shape and then inserting a rectangle such that the corners of the inserted rectangle touch the boundary of elliptical slot. The same procedure is repeated for the inner rectangle of first iteration geometry to obtain the second iteration geometry. The further iterations can be obtained [28].

4.1 Fractal wearable antenna design

Figure 21 represents the geometries of the initial, 1st and 2nd iterations of the crown rectangular fractal wearable microstrip antenna. The optimized dimensions of the presented three antennas are indicated in **Table 9**. This antenna is also pasted on Jeans material as a substrate. Also, the simulated S11 for the three iterations antennas are shown in **Figure 22**. In addition, the radiation patterns of the proposed antenna in E-plane ($\Phi = 0°$) and H-plane ($\Phi = 90°$) are simulated and plotted in **Figure 22**.

From **Figure 22**, the proposed 2nd iteration crown rectangular fractal wearable microstrip antenna can be used as a multiband antenna. This antenna is operated at three frequency bands in the same time with different application as WiMax, WiFi for modern wireless applications and the third frequency band may be used for fixed satellite (earth-space) applications. Also, note the great affinity between the first and second iterations (**Figure 23**). The simulation performance results are mentioned in **Table 10**.
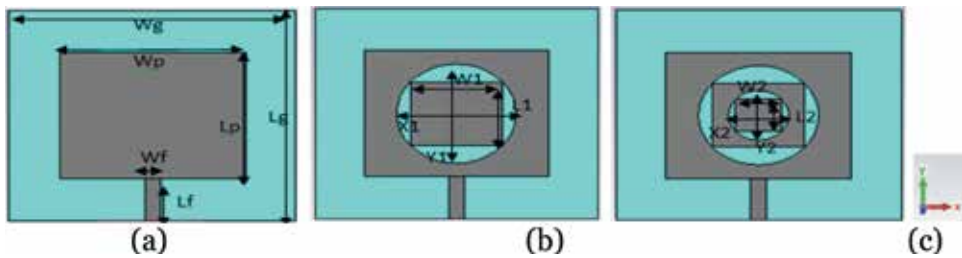
Figure 21.
Proposed fractal antenna structures: initial, 1st, and 2nd iterations.

Wg	Lg	Wp	Lp	Wf	Lf	L1	W1	L2	W2	X1	Y1	X2	Y2
57	50	37	30	3	10	15	18.5	7.5	9.25	12	11.85	6	5.9

Table 9.
The optimized dimensions of three iterations antenna.
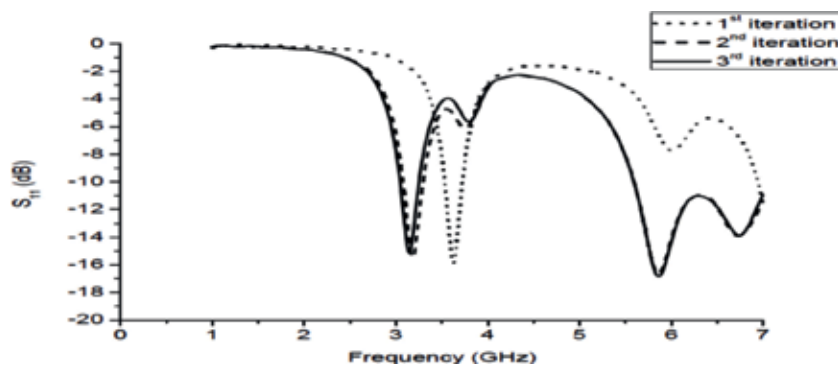
Figure 22.
*The S11 for the three antennas: initial, 1st, and 2nd iterations.*
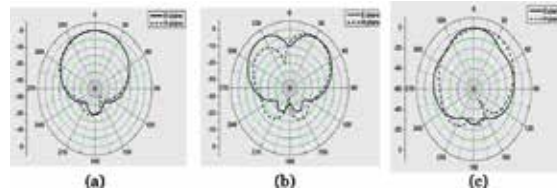
Figure 23.
Radiation pattern in E-plane, H-plane at: (a) 3.3, (b) 5.8, and (c) 6.7 GHz.

Resonant Frequency (GHz)	S11 (dB)	Gain (dB)	Efficiency %	Applications
3.3	−15.19	3.4	64.7	WiMax
5.8	−16.797	3.5	65.2	WiFi
6.7	−13.85	3.44	64.9	Satellite

Table 10.
The simulated performance results of the proposed fractal antenna.

5. Conclusion

This chapter focuses on the design and fabrication of different three types wearable fractal for modern wireless applications with body-area-networks.

A 3rd iteration fractal wearable antenna is designed and fabricated. This antenna is designed to be suitable for GPS, WiMax and WiFi (Bluetooth) applications at the same time. The presented antenna is a body-worn antenna to be attached with the human body. Therefore, the specific absorption ratio (SAR) plays a vital role in the design of this body-worn antenna. So that, the SAR value should be calculated and also improved. Another design is presented and also fabricated to improve the SAR value. The intended fractal antenna is attached with a spiral MTM cell etched in the ground plane. This spiral is used to minimize the SAR value by reducing the energy absorbed by the human body tissue. Finally, this design is integrated onto a floating life jacket. This smart jacket can be used for finding the human body if an accident happens.

A 2nd iteration Sierpinski carpet wearable antenna was designed and fabricated. This antenna was pasted on Jeans textile material as substrate. Two methods for measuring the dielectric constant (ε_r) and loss tangent ($\tan\delta$) of the Jeans material were presented in this chapter: a microstrip ring resonator method and DAK method. This antenna was operated at three resonance frequencies which were suitable for GPS, WiFi, and WiMax application.

A crown rectangular wearable fractal antenna was designed and fabricated. The proposed antenna was a 2nd iteration fractal antenna to operate at three resonance frequencies which were suitable for WiFi and WiMax applications over BAN-network and also might be used for satellite applications.

Author details

Mohamed I. Ahmed[1*] and Mai F. Ahmed[2]

1 Microstrip Department, Electronics Research Institute, Giza, Egypt

2 Department of Electrical and Electronics Engineering, Faculty of Engineering, Zagazig University, Zagazig, Egypt

*Address all correspondence to: miahmed@eri.sci.eg

IntechOpen

References

[1] Dumanli S, Sayer L, Mellios E, Fafoutis X, Hilton G, Craddock I. Off-body antenna wireless performance evaluation in a residential environment. IEEE Transactions on Antennas and Propagation. 2017

[2] Salonen P, Jaehoon K, Rahmat-Samii Y. Dual-band E-shaped patch wearable textile antenna. In: Proceedings of the IEEE International Symposium on the Antennas and Propagation Society; 2005

[3] Salonen P. Dual-band wearable textile antenna. International Symposium on the IEEE Antennas and Propagation Society. 2004;**1**:463-466

[4] Tanaka M, Jang JH. Wearable microstrip antenna. International Symposium on the IEEE Antennas and Propagation Society; Columbus, OH. 2003;**2**:704-707

[5] Crownver RM. Introduction to Fractals and Chaos. London, England: Jones and Bartlett Publishers; 1995

[6] Gianvittorio JP, Rahmat-Samii Y. Fractal antennas: A novel antenna miniaturization technique, and applications. IEEE Antennas and Propagation Magazine. January 2002;**44**(1):20-36

[7] Famolari D, Agrawal P. Architecture and performance of an embedded IP bluetooth personal area network. In: IEEE International Conference on Personal Wireless Communications. 2000. pp. 75-79

[8] Vallozzi L, Torre PV, Hertleer C, Rogier H. A textile antenna for off-body communication integrated into protective clothing for fire fighters. IEEE Transactions on Antennas and Propagation. April 2009;**57**(4):919-925

[9] Koski K, Vena A, Sydanheimo L, Ukkonen L, Rahmat-Samii Y. Design and implementation of electro-textile ground planes for wearable UHF RFID patch tag antennas. IEEE Antennas and Wireless Propagation Letters. 2013:964-967

[10] Arya S, Khan S, Shan CK, Lehana P. Design of a microstrip patch antenna for mobile wireless communication systems. Journal of Computational Intelligence and Electronic Systems. 2013;**1**(2):1-5

[11] Milligan TA. Modern Antenna Design. 2nd ed. John Wiley & Sons, Inc.; 2005

[12] Zainud-Deen SH, Malhat H, Awadalla KH. Radio frequency identification antennas: Design and applications [PhD dissertation]. Department of Electronics and Electrical Communications Engineering; 2011

[13] Sunohara T, Laakso I, Hirata A, Onishi T. Induced field and SAR in human body model due to wireless power transfer system with induction coupling. IEEE Electromagnetic Compatibility. 2014;**5**:40-48

[14] Hirata A, Fujiwara O, Nagaoka T, Watanabe S. Estimation of whole-body average SAR in human models due to plane-wave exposure at resonance frequency. IEEE Transactions on Electromagnetic Compatibility. 2010;**52**:41-48

[15] Zhao K, Zhang S, Ying Z, Bolin T, He S. SAR study of different MIMO antenna designs for LTE application in smart mobile handsets. IEEE Transactions on Antennas and Propagation. June 2013;**61**(6):3270-3279

[16] Tateno A, Tanaka K, Nagaoka T, Watanabe S, Saito K, Takahashi M, et al. Comparison of SAR in human body radiated from mobile phone and tablet computer. In: International Symposium on Electromagnetic Compatibility, vol. 6; Tokyo. 2014. pp. 55-59

[17] Nagaoka T, Watanabe S. Large-scale calculation of the specific absorption rate in a human body exposed to RF-EMFs by GPU cluster system. In: International Symposium on Electromagnetic Compatibility, vol. 3. 2013. pp. 110-116

[18] Kivekäs O, Ollikainen J, Lehtiniemi T, Vainikainen P. Bandwidth, SAR, and efficiency of internal mobile phone antennas. IEEE Transactions on Electromagnetic Compatibility. February 2004;**46**(1)

[19] Hadjem A, Conil E, Gati A, Wong MF, Wiart J. Analysis of power absorbed by children's head as a result of new usages of mobile phone. IEEE Transactions on Electromagnetic Compatibility. Nov. 2011;**52**(4):812-819

[20] Tanaka M, Jang JH. Wearable microstrip antenna. In: IEEE APS International Symposium and URSI North American Radio Science Meeting; Columbus, OH, USA; vol. 5. June 2003. pp. 41-48

[21] "http://www.antenna-theory.com/antennas/wearable-antennas.php"

[22] Ismail M, Elsadek H, Abdallah EA, Ammar AA. New configurations of planar fractal microstrip antenna. In: IEEE International Symposium on Antennas and Propagation; San Diego, California. July 2008

[23] Serra AA, Nepa P, Manara G. A wearable two-antenna system on a life jacket for Cospas-Sarsat personal locator beacons. IEEE Transactions on Antennas and Propagation. February 2012;**60**(2):1035-1042

[24] Yadav AN, Chawhan R, Singhal DPK, Tiwari KA. Simulation of Sierpinski carpet fractal antenna. Telecommunications. May 2011;**8**

[25] Hopkins R, Free C. Equivalent circuit for the microstrip ring resonator suitable for broadband materials characterisation. IET Microwaves, Antennas & Propagation. February 2008;**2**(1):66-73

[26] Rashidian A, Aligodarz MT, Klymyshyn DM. Dielectric characterization of materials using a modified microstrip ring resonator technique. IEEE Transactions on Dielectrics and Electrical Insulation. Aug. 2012;**19**(4)

[27] www.speag.com/products/dak/dielectric-measurements/

[28] Mehak S, Rana SB, Bhomia Y. Design of a combined crown and Sierpinski fractal antenna. International Journal of Electronics & Communication Technology. Sept 2016;**7**

Chapter 5

Parrondian Games in Discrete Dynamic Systems

Steve A. Mendoza and Enrique Peacock-López

Abstract

An interesting problem in nonlinear dynamics is the stabilization of chaotic trajectories, assuming that such chaotic behavior is undesirable. The method described in this chapter is based on the Parrondo's paradox, where two losing games can be alternated, yielding a winning game. The idea of alternating parameter values has been used in chemical systems, but for these systems, the undesirable behavior is not chaotic. In contrast, ecological relevant map in one and two dimensions, most of the time, can sustain chaotic trajectories, which we consider as undesirable behaviors. Therefore, we analyze several of such ecological relevant maps by constructing bifurcation diagrams and finding intervals in parameter space that satisfy the conditions to yield a desirable behavior by alternating two undesirable behaviors. The relevance of the work relies on the apparent generality of method that establishes a dynamic pattern of behavior that allows us to state a simple conjecture for two-dimensional maps. Our results are applicable to models of seasonality for 2-D ecological maps, and it can also be used as a stabilization method to control chaotic dynamics.

Keywords: chaos control, Parrondo's paradox, switched dynamic systems, ecological maps, seasonality

1. Introduction

In population dynamics, discrete dynamic systems have been used to model the dynamics of ecological systems. One of the first maps used in ecology that suggested to study the new, (X_{n+1}), and the old, (X_n), non-overlapping populations is the logistic map. [1] Although a simple one-dimensional (1-D) map, the logistic map shows complex dynamics including chaos. Furthermore, the analyses of the logistic map gave us a better understanding of the properties of chaotic dynamics [2–7].

In the case of 1-D discrete dynamics, for the last 18 years, alternate dynamics strategies have been the center of attention due to the so-called Parrondo paradox [8–10], where two losing games can be combined to yield a winning game. Furthermore, the idea that "lose + lose = win" has been extended to "chaos +chaos = periodic" in one-dimensional maps [11]. Just recently and for the first time, we were able to find the Parrondo dynamics in two 2-D maps [12]. In the contest of seasonality, we consider the alternation of undesirable dynamical behaviors yield a desirable behavior [13, 14]. So in the context of population dynamics we have considered cases where "undesirable + undesirable = desirable" dynamical behaviors occur as a result of a simple alternation of parameters [15–21].

In our present discussion, we extend our seasonality modeling strategy to several two-dimensional ecologically relevant maps and find that the "undesirable + undesirable = desirable", the "chaos + chaos = periodic", as well as, the "periodic + periodic = chaos" behaviors are not unique to 1-D maps. In Section 2, we consider a delayed logistic map, and in Section 3, we analyze a Lotka-Volterra map. In Section 4, we study a modified 2-D Ricker map, and in Section 5, we analyze the Beddington map. In Section 6, we discuss a modified Lotka-Volterra map, which includes a logistic prey growth. We conclude in Section 7 with a discussion and a summary of our results.

2. Delayed logistic equation

In our analysis of two-dimensional maps, we begin with the extended logistic map that incorporates a delay in population growth, defined by the following relation:

$$X_{n+1} = Y_n \tag{1}$$

$$Y_{n+1} = C\, Y_n(1 - X_n) \tag{2}$$

where C is our bifurcation parameter. For the Lagged Logistic Equation, we consider C values from 0 to 2.27 in the original map, although with alternation, we can obtain a bifurcation diagram showing larger C values. **Figure 1**, shows the regular bifurcation map of the lagged logistic model. For all of the maps we study, both the X and Y graphs for a given show the same dynamics; for instance, parameters associated with chaotic dynamics in the X map are also associated with chaotic dynamics in the Y map; since we focus on a map's dynamics, we only show the X function map.

From **Figure 1**, we define our parameter value regions associated with complex or non-complex dynamics. The map on the left of the figure shows the whole bifurcation map; while the right magnifies the complex region. On the right hand figure, which is the magnified map, we can clearly see some periodic windows, but we pick parameter values associated with complex dynamics.

Next, we switch, or alternate, the parameter values between even and odd iterations through the following relation:

$$X_{n+1} = \begin{cases} f_n(X_n, Y_n) = Y_n & \text{if n even} \\ \\ f_n(X_n, Y_n) = Y_n & \text{if n odd} \end{cases} \tag{3}$$

$$Y_{n+1} = \begin{cases} g_n(X_n, Y_n) = C_e\, Y_n(1 - X_n) & \text{if n even} \\ \\ g_n(X_n, Y_n) = C_o\, Y_n(1 - X_n) & \text{if n odd} \end{cases} \tag{4}$$

The equation above describes our switching strategy in which we pick one parameter for every odd iteration, which we name C_o, and use the even parameter, C_e, as our bifurcation parameter, for every even iteration. For the first type of behavior, we pick one parameter associated with complex dynamics as our C_o value and switch it with our even parameter, C_e, in areas associated with chaotic dynamics. In our case, we see chaotic dynamics for C values greater than 2.0 when we construct the bifurcation diagram for Eqs. (1) and (2). In the resulting alternated, or switched, bifurcation diagram, represented by Eq. (3) for the current section, we

look for regions that have periodic oscillations that are normally associated with chaos, thus resulting in the case "chaos + chaos = order." Hence, for every switching map that we study, in the figures we also show the unswitched map for the same C_e parameter space. We make a note that the alternation of parameter values as defined by our switching strategy may result in an extension of C parameters yielding oscillations; that is we may see oscillations for C values greater than 2.27 as in the case for lagged logistic map. To compare our maps with Eqs. (1) and (2), we only study bifurcation maps using Eqs. (3) and (4) from $C = 0$ to 2.27.

For our analysis, we pick a C_o as in the "chaos + chaos = order" case; however, we may choose a parameter within the periodic windows in the chaotic region, and when using the switched map, we focus on the C_e values that are less than the onset of chaos, which for the case of the lagged logistic pap is $C = 2$. We use the analysis discussed above for all of the cases in this paper.

For our first example of "chaos + chaos = periodic", we consider the parameter value, $C_o = 2.10$ and Eqs. (3) and (4). In our bifurcation diagram for Eqs. (3) and (4), in **Figure 2**, we consider C_e greater than 2 and look for C_e values that give us periodic oscillations. **Figure 2** shows two maps at once, the left hand showing Eqs. (1) and (2), and the right hand graph shows Eqs. (1) and (2) with $C_o = 2.1$. In this case, from **Figure 2**, we can see one region of periodicity from $C_e = 2.26$ to 2.27.

Another combination of parameters yielding "chaos+chaos = periodic" uses $C_o = 2.15$ and Eqs. (3) and (4), where **Figure 3** shows a range of C_e values for which "chaos + chaos = periodic" holds, from $C_e = 2.36$ to 2.38. The same figure also shows other values for which the "chaos + chaos = periodic" relation holds, but these bands are not as prominent as the one we focus on. Through out the paper, we make a point that different C_e values give widely different behaviors and these differences in dynamic behaviors reveals the differences in the C_e values that give us desirable behaviors. For the rest of the paper, the approximate ranges of C_e will be given for
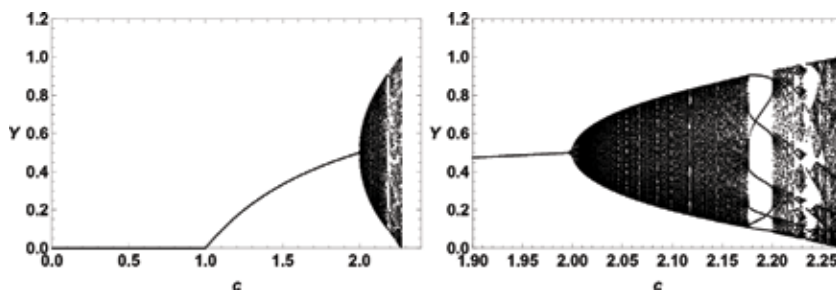

Figure 1.
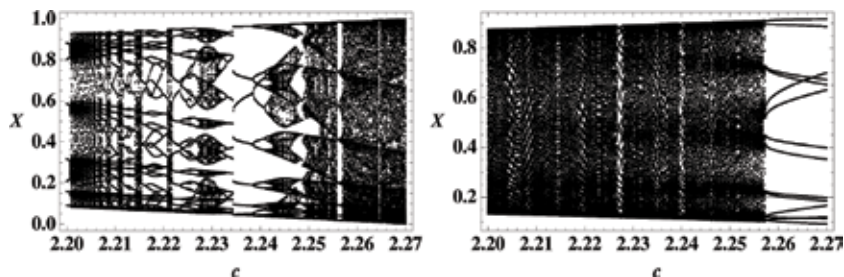*Lagged logistic map model, Eqs. (1,2), with C = 0 to C = 2.27 and the region from C = 1.90 to C = 2.27.*

Figure 2.
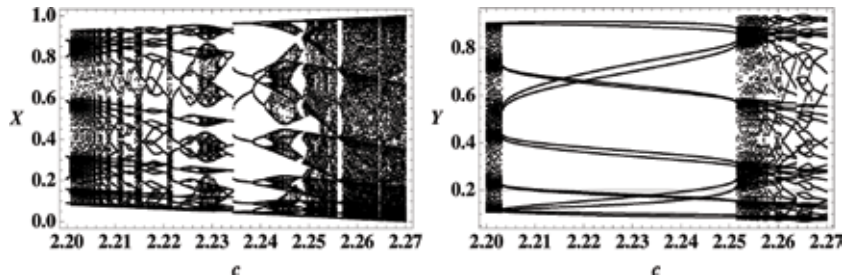*Bifurcation diagram for Eqs. (1) and (2) and Eqs. (3) and (4), using C₀ 2.1.*

Figure 3.
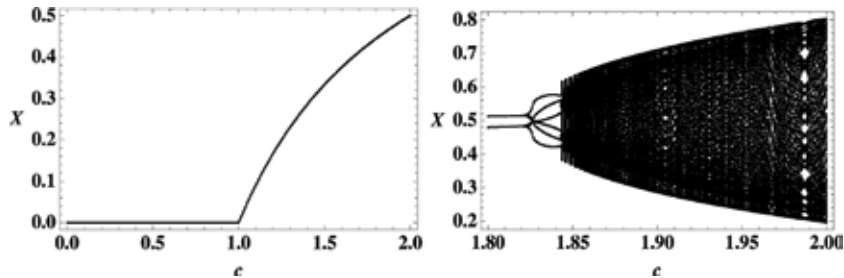*Bifurcation diagram for Eqs. (1) and (2), and Eqs. (3) and (4), using $C_o = 2.15$.*

Figure 4.
Bifurcation diagram for Eqs. (1) and (2), and Eqs. (3) and (4), using C_o 2.19.

one window that satisfies the "chaos + chaos = order" or "periodicity + periodicity = chaos", since there are sometimes a variety of parameters meeting the relevant criteria for switching.

We complete our analysis of delayed logistic map with one case in which "periodic + periodic = chaos". As mentioned beforehand, we pick our value associated with periodic trajectories from the area associated with chaotic trajectories, and focus on C_e values less than the chaotic region for comparison. In particular, we choose $C_o = 2.19$ as our periodic parameter for Eqs. (3) and (4); **Figure 4** shows the corresponding bifurcation map, and, from the figure, we see one prominent example of "periodic+periodic = chaos" for C_e = 1.85 to 2.00.

3. Lotka-Volterra model

We begin our next section by discussing a discretized form of the Lotka-Volterra model. The Lotka-Volterra map describes predator prey interactions, assuming that the prey has a relatively high initial population, and that the predator's growth rate is directly proportional to the prey's growth rate.

The model follows a relation defined by the map below

$$X_{n+1} = (1 + r)X_n - rX_n^2 - C\,X_n\,Y_n \tag{5}$$

$$Y_{n+1} = C\,X_n\,Y_n \tag{6}$$

In **Figure 5**, showing Eqs. (5) and (6), we look at the unswitched map, defined by showing the ranges of periodic and aperiodic behavior. As in the previous section, we use the unswitched bifurcation map as a comparison to the switched map when using certain parameters. For this section, we focus on the interval $C = 0$ to 2.8, and set r = 2 for this map and the rest of the maps that have an r parameter.

$$X_{n+1} = \begin{cases} f_n(X_n, Y_n) = (r+1)(X_n) - r(X_n)^2 - C_e X_n Y_n & \text{if n even} \\ f_n(X_n, Y_n) = (r+1)(X_n) - r(X_n)^2 - C_o X_n Y_n & \text{if n odd} \end{cases} \qquad (7)$$

$$Y_{n+1} = \begin{cases} g_n(X_n, Y_n) = C_o X_n Y_n & \text{if n odd} \\ g_n(X_n, Y_n) = C_e X_n Y_n & \text{if n even} \end{cases} \qquad (8)$$

As before, we pick a C_o value associated with a chaotic trajectory and alternate with C_e, using Eq. (7), which we use as the bifurcation parameter, illustrated in **Figure 6**. For this figure, we use $C_o = 2.1$, and we can easily find conditions in which "chaos + chaos = order." In particular, we see this phenomena for parameter values of $C_e = 2.33$–2.40. **Figure 7**, shows another example of "chaos + chaos = order" using Eqs. (7) and (8) with a C_o value of 2.22, and in the corresponding bifurcation diagram for roughly $C_e = 2.58$–2.65.

We conclude the present section with an example of "periodicity + periodicity = chaos", using Eqs. (7) and (8) and $C_e = 2.44$. In this case, in **Figure 8**, we see
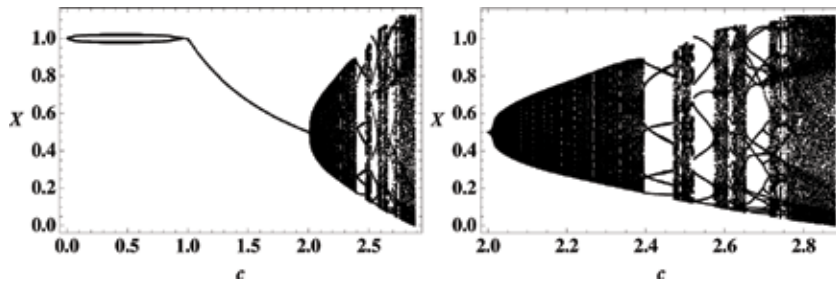

Figure 5.
Bifurcation diagram for Eqs. (5) and (6), showing the interval studied, as well as a close up of the chaotic region.
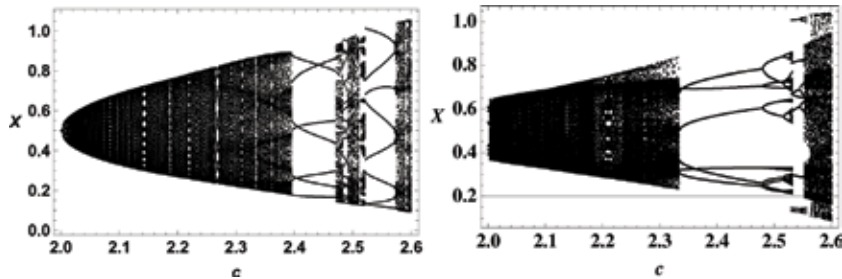

Figure 6.
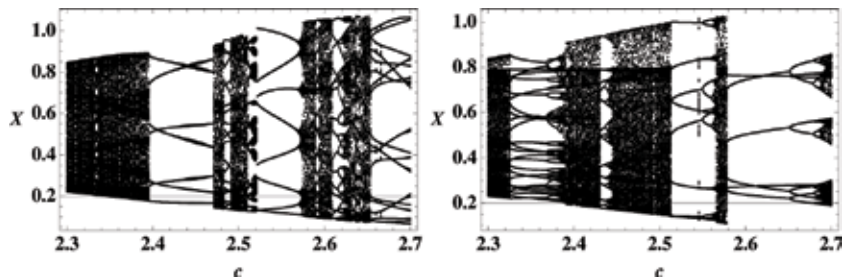*Bifurcation diagram for Eqs. (5) and (6) and Eqs. (7) and (8) with the C_o value 2.1.*

Figure 7.
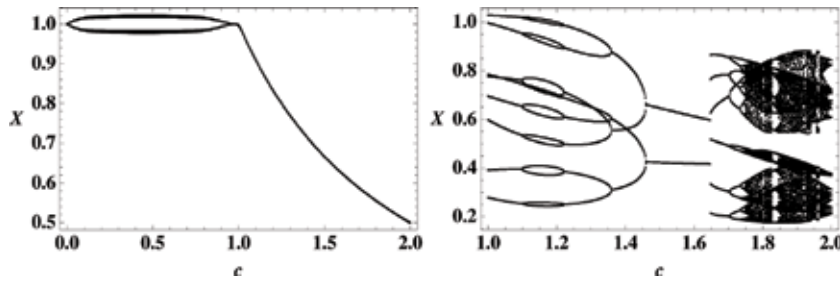*Bifurcation diagram for Eqs. (5) and (6) and Eqs. (7) and (8) with the C_o value 2.22.*

Figure 8.
Bifurcation diagram for Eqs. (5) and (6) and Eqs. (7) and (8) with the C_o value 2.44.

some chaotic behavior for values of C_e in the interval $[1.75, 2.00]$, a region that is periodic when using Eqs. (5) and (6).

4. Modified 2-D Ricker map

Another interesting map includes an exponential term, describing the prey growth, with a simple predator–prey interaction term. The map is determined by the following equations:

$$X_{n+1} = X_n \ Exp\left[r(1 - X_n - Y_n)\right] \tag{9}$$

$$Y_{n+1} = C\,X_n(Y_n) \tag{10}$$

which is in essence modified and extended to 2-D Ricker-like map [22]. The corresponding switched map is defined below:

$$X_{n+1} = \begin{cases} f_n(X_n, Y_n) = X_n \ Exp\left[r(1 - X_n - Y_n)\right] & \text{if n even} \\ f_n(X_n, Y_n) = X_n \ Exp\left[r(1 - X_n - Y_n)\right] & \text{if n odd} \end{cases} \tag{11}$$

$$Y_{n+1} = \begin{cases} g_n(Y_n) = C_e X_n Y_n & \text{if n even} \\ g_n(Y_n) = C_o X_n Y_n & \text{if n odd} \end{cases} \tag{12}$$

Figure 9, showing Eqs. (9) and (10), considers the range of C values we focus on, from C = 0 to 2.8. We want to remark however, that this map also shows some interesting behavior beyond the interval of study, but we choose this interval to get a close up of the intervals of periodicity, since this interval is where we find our relevant behavior. For the X function we study, at higher values, the function stays at unity for values of C = 28 and higher, while the Y function stays at extinction, or Y = 0.
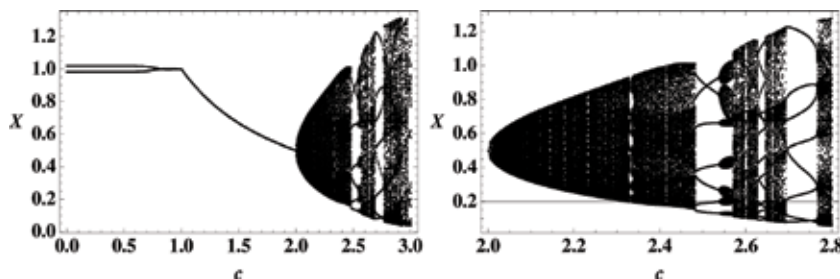

Figure 9.
Bifurcation map for Eqs. (9) and (10) showing the interval studied, as well as a close up of the chaotic region.

As in previous cases, we start with finding parameter values satisfying the "chaos + chaos = order" relation. To begin, we use Eqs. (11) and (12) with C_o = 2.10, associated with aperiodic dynamics. **Figure 10** zooms into the region for which "chaos + chaos = order" holds. From this diagram, we see a narrow region of periodicity from C = 2.775 to 2.790.

We then use Eqs. (11) and (12) with C_o = 2.26, for which **Figure 11** hones in on the relevant C_e parameter values. The interval of C_e values is significantly wider in this case than the previous one, since we find "chaos + chaos = order" for 2.74–2.80.

We finish this section by introducing one case in which "periodic + periodic = chaos". We pick the periodic parameter C_o = 2.333. In some maps, it is harder to find periodic windows, although they could usually be found sometimes but an extra significant figure is necessary such as in this case. We find chaos in this map from C_e = 1.71 to 2.00, as shown in **Figure 12**, periodic values when using Eqs. (11,12).
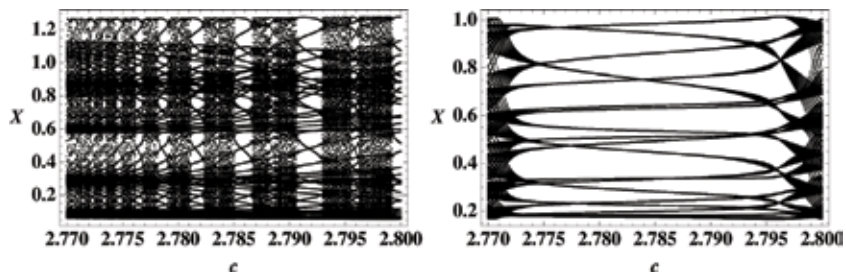

Figure 10.
Bifurcation diagram for Eqs. (9) and (10) and Eqs. (11) and (12) with the C_o value 2.10.
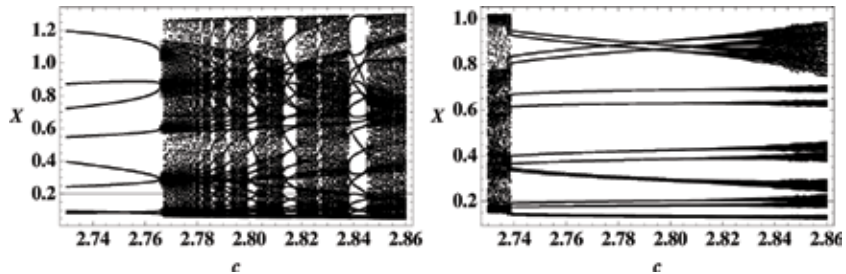

Figure 11.
Bifurcation diagram for Eqs. (9) and (10) and Eqs. (11) and (12) with the C_o value 2.26.
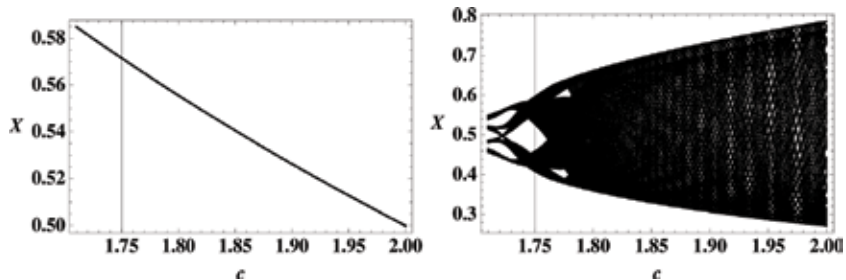

Figure 12.
Bifurcation diagram for Eqs. (9) and (10) and Eqs. (11) and (12) with the C_o value 2.333.

5. Beddington model

Our next map is the Beddington 2-D map defined by the following equations:

$$X_{n+1} = X_n \; Exp\,(r(1-X_n) - Y_n) \tag{13}$$

$$Y_{n+1} = C\,X_n(1 - Exp\,(-Y_n)) \tag{14}$$

along with the corresponding alternation equation.

$$X_{n+1} = \begin{cases} f_n(X_n, Y_n) = X_n \; Exp\,(r(1-X_n) - Y_n) & \text{if n even} \\ f_n(X_n, Y_n) = X_n \; Exp\,(r(1-X_n) - Y_n) & \text{if n odd} \end{cases} \tag{15}$$

$$Y_{n+1} = \begin{cases} g_n(X_n, Y_n) = C_e\,X_n(1 - Exp\,(-Y_n)) & \text{if n even} \\ g_n(X_n, Y_n) = C_o\,X_n(1 - Exp\,(-Y_n)) & \text{if n odd} \end{cases} \tag{16}$$

Figure 13, showing Eqs. (13) and (14), shows the parameter range we use to analyze the map. We pick points between 0 and 14, and show the corresponding bifurcation diagrams within that range. We pick 14 as our maximum value because above that parameter, there are only steady state solutions.

We start with describing our first chaotic value, C_o = 10, for Eqs. (15) and (16). **Figure 14** shows the corresponding bifurcation diagram, and we see a relatively wide range of C_e values for which we have "chaos + chaos = order". We find this behavior for most points of C_e between 4.54 and 4.7.

We then use Eqs. (15) and (16), with C_o = 4.0, and here we also see a relatively wide range of parameters in which we find that "chaos + chaos = periodicity". Specifically, we see that alternating with C_e = 10.7–10.88 gives us the desired behavior, shown in **Figure 15**. Our last figure pertaining to this map, **Figure 16**, shows the

Figure 13.
Bifurcation diagram for Eqs. (13) and (14) showing the interval studied, as well as a close up of the chaotic region.

Figure 14.
Bifurcation diagram for Eqs. (13) and (14) and Eqs. (15) and (16) with the C_o value 10.

Figure 15.
Bifurcation diagram for Eqs. (13) and (14) and Eqs. (15) and (16) with the C_o value 4.0.

Figure 16.
Bifurcation diagram for Eqs. (13) and (14) and Eqs. (15) and (16) with the C_o value 6.0.

"periodic + periodic = chaos" behavior, for C_o = 6.0. **Figure 16** shows the area of the map that is normally periodic, and shows characteristic chaotic behavior from C_e = 1.7–3.0, although this particular map shows some periodic windows than the other "periodic + periodic = chaos" maps.

6. Modified Lotka-Volterra map

Our last 2-D map considers a logistic growth, and an interaction term, and only a predation term for the predator. The dynamics of this map is considerably different than the previous two maps,

$$X_{n+1} = (1+r)X_n - r\,X_n^2 - \frac{CX_nY_n}{X_n + h} \tag{17}$$

$$Y_{n+1} = \frac{CX_nY_n}{X_n + h} \tag{18}$$

As before, the switched map is shown below.

$$X_{n+1} = \begin{cases} f_n(X_n) = (1+r)X_n - rX_n^2 - \dfrac{C_eX_nY_n}{X_n + h} & \text{if n even} \\[3mm] f_n(X_n) = X_n(r+1) - r(X_n)^2 - \dfrac{C_oX_nY_n}{X_n + h} & \text{if n odd} \end{cases} \tag{19}$$

$$Y_{n+1} = \begin{cases} g_n(Y_n) = \dfrac{C_oX_nY_n}{X_n + h} & \text{if n odd} \\[3mm] g_n(Y_n) = \dfrac{C_eX_nY_n}{X_n + h} & \text{if n even} \end{cases} \tag{20}$$

Aside from the r parameter, this map also has the h parameter, which we set equal to unity. Unlike the previous two maps we study that have relevant behaviors past C = 10, the max value of the unswitched map is C = 3.85, but chaos is only present above C = 3.0, as shown in **Figure 17**.

Our first chaotic point is C_o = 3.3, and the corresponding bifurcation diagram is shown in **Figure 18**. There is a somewhat small region of periodicity from C_e = 3.704 to 3.724.

The second to last figure, **Figure 19** shows our final odd switching parameter, C_o = 3.1 and the corresponding bifurcation diagram, which shows a similar range of periodic parameter values, specifically, C_e = 3.70–3.72.

Our last figure, **Figure 20**, shows an example of "periodic + periodic = chaos", where we switch with C_o = 3.57 and see chaos for most values between C_e = 2.5 and 3.0.
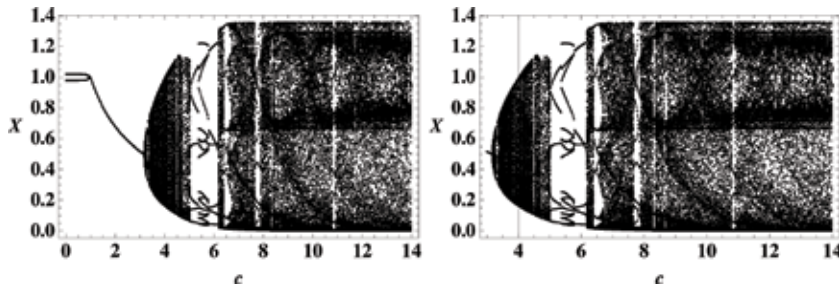

Figure 17.
Bifurcation diagram for Eqs. (17) and (18) showing the interval studied, as well as a close up of the chaotic region..

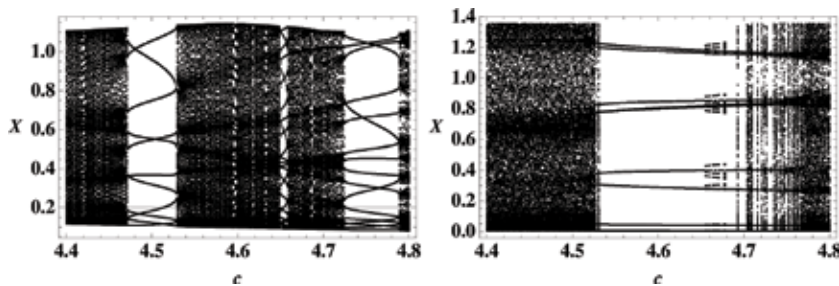**Figure 18.**
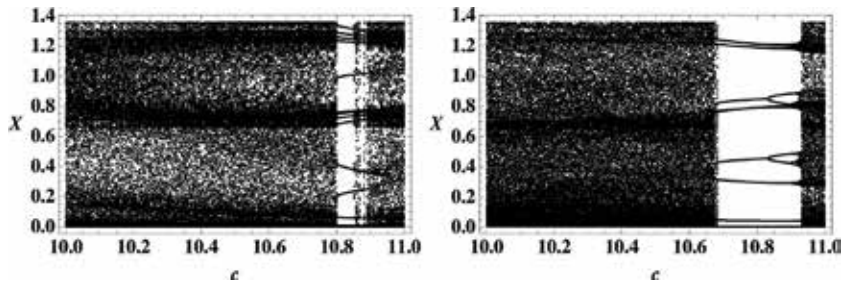*Bifurcation diagram for Eqs. (17) and (18) and Eqs. (19) and (20) with the C_o value 3.3.*

Figure 19.
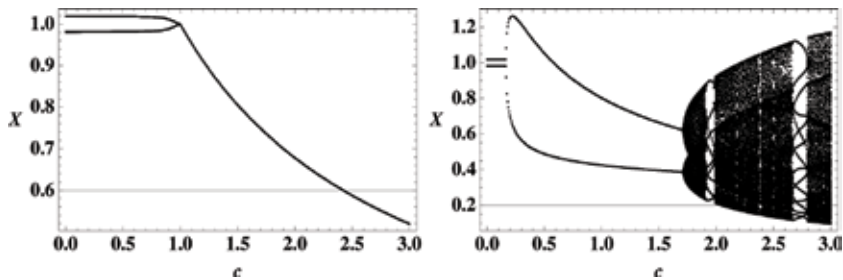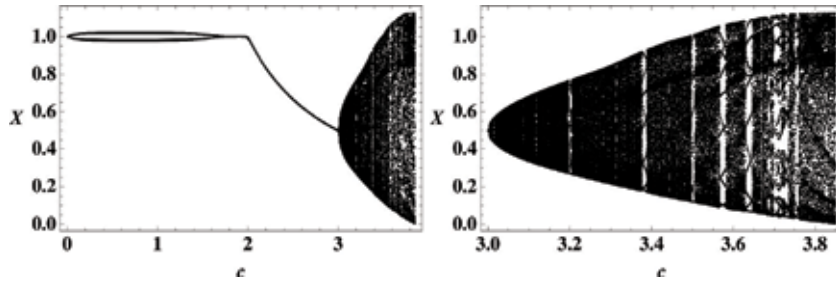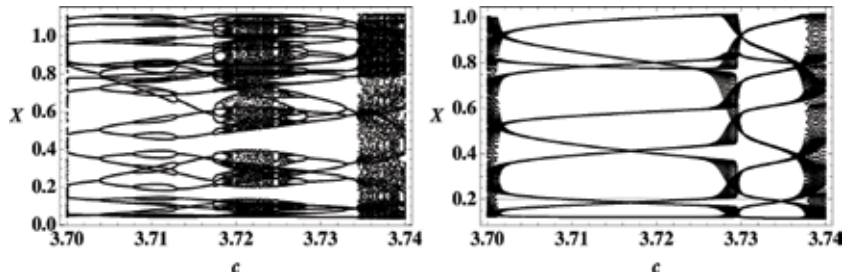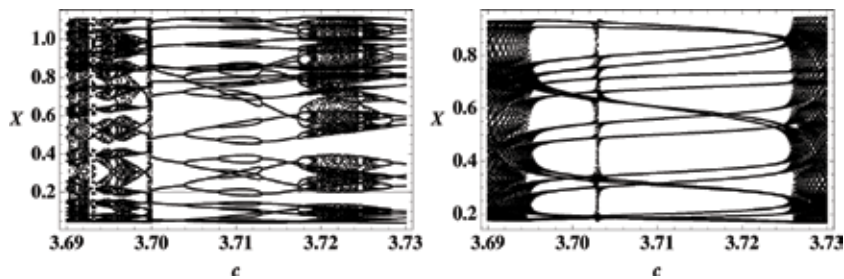*Bifurcation diagram for Eqs. (17) and (18) and Eqs. (19) and (20) with the C_o value 3.1.*
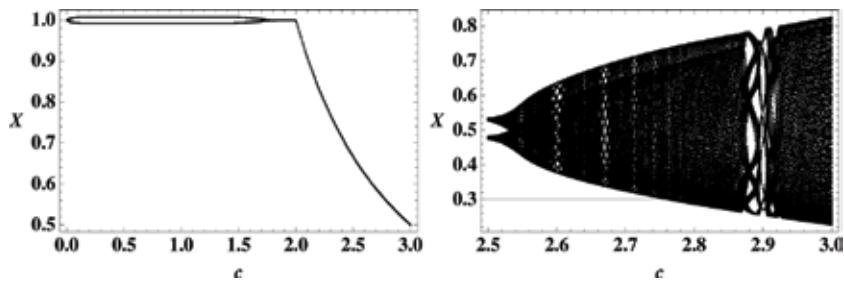
Figure 20.
Bifurcation diagram for Eqs. (17) and (18) and Eqs. (19) and (20) with the C_o value 3.57.

7. Discussion

In previous sections, we have analyzed five relevant ecological 2-D maps, setting a pattern of dynamic behavior similar to the well studied "chaos + chaos = periodic" in switched 1-D maps. Therefore, with the results discussed in this chapter, we can extend the 1-D maps conjecture to 2-D maps. The conjecture asserts that given a map with chaotic dynamics, we can find two parameters associated to chaotic trajectories that, when alternated yield a periodic trajectory. In general, we can consider these kinds of maps as nonautonomous maps because one of the parameters is a function of the iterations. In most case, we pick a parameter value for the even iterations and a different parameter for the odd iterations. But the connection with the Parrondo's paradox is associated with the kind of alternating parameters, which in the conjecture are parameter associated with chaotic, or, in general, complex trajectories.

The case of "chaos + chaos = periodic" was presented for the first time by Almeida et al. [16] for simple 1-D maps, and just recently for 2-D maps by Mendoza et al. [12]. The implication of the so-called Parrondo's dynamics has been used to model seasonality, but with the observation that, under the Parrondo dynamics, the case of "periodic + periodic = chaos" is also possible [15]. As generalization we have consider cases of "undesirable + undesirable = desirable" dynamics behaviors to analyze simple models of seasonality [23–25], which include migration or immigration [13, 14].

In the present analysis, we emphasize the use of bifurcation diagrams to find intervals of values in parameter space that could satisfy the "undesirable + undesirable = desirable" or "periodic + periodic = chaos" dynamics. Although we are interested in modeling ecological systems and in particular the effect of seasonality, one could use our results to look at the switched maps as a way to control chaotic dynamics. In particular an extension to continuous dynamic systems may be relevant or applicable to chemical and mechanical systems [26].

In summary, our approach of building bifurcation diagrams readily yield intervals of parameter values that can show the so-called Parrondian dynamics for 1-D and 2-D maps. We have concentrated on ecological relevant maps, but the approach applies to any kind of maps. In particular, we can easily find parameters that show desirable dynamics in switched maps, controlling complex or undesirable dynamics, with the by product that we can also avoid the alternation of desirable dynamics that could yield undesirable dynamics in switched maps. Finally, we believed that we have stablished a pattern of dynamic behavior that supports the conjecture described in previous paragraphs.

8. Conclusions

In previous sections, we have stablished a pattern of dynamic behavior for 2-D maps, which have been used to model ecological systems. The dynamic pattern allows to state that for any 2-D maps that shows chaotic dynamics for a set of parameters, we can always find two of such parameters that, when alternate, yield a periodic trajectory. This conjecture is an extension of the so-called Parrondo's paradox, in the sense that two undesirable dynamics can be alternate to yield a desirable dynamics. In other words, we can always find a region in parameter space, where we can select a pair of such parameters. Therefore, we the developed methodology can be use, in general, as a chaos control approach, and, in particular, we can use it to model, in the case of ecological maps, seasonality. Although we interested in ecological relevant 2-D maps, we believed that our conjecture can be extended to other type of 1-D and 2-D maps. Finally, we consider that the major application of the methodology is in controlling chaotic dynamics.

Acknowledgements

Author details

Steve A. Mendoza and Enrique Peacock-López*
Department of Chemistry, Williams College, MA, USA

*Address all correspondence to: epeacock@williams.edu

IntechOpen

References

[1] May RM. Simple mathematical models with very complicated dynamics. Nature. 1976;**261**:459-467

[2] May RM. Stability and Complexity in Model Ecosystems. Princeton: Princeton University Press; 1974

[3] Kot M. Elements of Mathematical Ecology. Cambridge: Cambridge University press; 2001

[4] Turchin P. Complex Population Dynamics. Princeton: Princeton University Press; 2003

[5] Mangel M. The Theortical Biologist's Toolbox. Cambridge: Cambridge University press; 2006

[6] Allen LJS. An Introduction to Mathematical Biology. Upper Saddle River, NJ: Pearson Prentice Hall; 2007

[7] May RM, McLean AR. Theoretical Ecology: Principles and Applications. Oxford: Oxford University Press; 2007

[8] Harmer GP, Abbott D. Losing strategies can win by Parrondo's paradox. Nature. 1999;**402**:864

[9] Harmer GP, Abbott D. Parrondo's paradox. Statistical Science. 1999;**14**:14

[10] Harmer GP, Abbott D, Taylor PG. The paradox of Parrondo's games. Proceedings of the Royal Society. 2000;**456**:247-259

[11] Cánovas JS, Linero A, Peralta-Salas D. Dynamic Parrondo's paradox. Physica D. 2006;**218**:177-184

[12] Mendoza SA, Matt EW, Guimaraes-Blandon DR, Peacock-López E. Parrondo's paradox or chaos control in discrete two-dimensional dynamic systems. Chaos, Solitons & Fractals. 2018;**106**:86-93

[13] Peacock-López E. Seasonality as a Parondian game. Physics Letters A. 2011;**375**:3124-3129

[14] Silva E, Peacock-López E. Seasonality and the logistic map. Chaos, Solitons & Fractals. 2017;**95**:152-156

[15] Percus OE, Percus JK. Can two wrongs make a right? Coin-tossing games and Parrondo's paradox. Mathematical Intelligencer. 2002;**24**:68-72

[16] Almeida J, Peralta-Salas D, Romera M. Can two chaotic systems give rise to order? Physica D. 2005;**200**:124-132

[17] Behrends E. Stochastic dynamics and Parrondo's paradox. Physica D. 2008;**237**:198-206

[18] Boyarsky A, Góra P, Aslam MS. Randomly chosen chaotic maps can give rise to nearly ordered behavior. Physica D. 2005;**210**:284-294

[19] Amengual P, Meurs P, Cleuren B, Toral R. Reversal of chance in paradoxical games. Physica A. 2006;**371**:641-648

[20] Levinohn EA, Mendoza SA, Peacock-López E. Switching induced complex dynamics in an extended logistic map. Chaos, Solitons & Fractals. 2012;**45**:426-432

[21] Maier MPS, Peacock-López E. Switching induced oscillations in the logistic map. Physics Letters A. 2010;**374**:1028-1032

[22] Ricker WE. Stock and recruitment. Journal of the Fisheries Research Board of Canada. 1954;**11**:559-623

[23] Blasius B, Kurths J, Stone L, editors. Complex Population Dynamics. Singapore: World Scientific; 2007

[24] Allen LJS. An Introduction to Mathematical Biology. Upper Saddle River: Prentice Hall; 2007

[25] Kot M, Schaffer WM. The effects of seasonality on discrete models of population growth. Theoretical Population Biology. 1984;**26**:340-360

[26] Kohar V, Ji P, Choudhary A, Sinha S, Kurths J. Synchronization in time-varying networks. Physical Review E. 2014;**90**:022812

Chapter 6

Fractal Structures of the Carbon Nanotube System Arrays

Raïssa S. Noule and Victor K. Kuetche

Abstract

In this work, we investigate fractals in arrays of carbon nanotubes modeled by an evolution equation derived by using a rigorous application of the reductive perturbation formalism for the Maxwell equations and for the corresponding Boltzmann kinetic equation of the distribution function of electrons in such nanomaterials. We study the integrability properties of our dynamical system by using the Weiss-Tabor-Carnevale analysis. Actually, following the leading order analysis, we write the solution in the form of series of Laurent. We also use the Kruskal's simplification to find the solutions. Using the truncated Painlevé expansion, we construct the auto-Backlund transformation of the system. We take advantage of the above properties to construct a wide panel of structures with fractals properties. As a result, we unearth some typical features, namely the fractal dromion, the fractal lump, the stochastic and nonlocal fractal excitations. We also address some physical implications of the results obtained.

Keywords: carbon nanotubes, Weiss-Tabor-Carnevale analysis, Kruskal's simplification, auto-Backlund transformation, fractal excitations

1. Introduction

Carbon nanotubes stand to be one of the wonder materials of the present century [1–3] owing to their tremendous range of physical, mechanical, thermal, electronic, and optical properties. They are found in some flat panel displays, some field-effect transistors as emerging applications exploiting the good thermal and electronic conductivities of the above nanomaterials. The carbon nanotubes were synthesized previously in 1991 as graphitic carbon needles with diameter ranging from 4 to 30 nm and length up to 1 μm [4]. Large-scale synthesis [5] provided an impetus to research in the area of carbon fiber growth, as well as in the production and characterization of fullerene materials. Two years later [6], abundant single-shell tubes with diameters of about 1 nm were synthesized. In the past few years, some studies of various nonlinear effects in carbon nanotube arrays have been achieved. There are intrinsic localized modes in strongly nonlinear systems of anharmonic lattices [7, 8], large-amplitude oscillating modes with additional features of being nonlinear as well as discrete [9], spin-wave propagation [10], propagation of short optical pulses with dispersive nonmagnetic dielectric media [11], propagation of ultimately short optical pulses in coupled graphene waveguides [12, 13].

From the reductive perturbation method, Leblond and Mihalache [14, 15] investigated the formation of ultrashort spatiotemporal optical waveforms in arrays of carbon nanotubes while deriving a new coupled system. They actually used the multiscale analysis for the Maxwell equations and for the corresponding Boltzmann kinetic equation of the distribution function of electrons. The above authors [14] showed that a perturbed few-cycle plane-wave input evolves into a robust two-dimensional light bullet propagating without being dispersed and diffracted over long distance with respect to the wavelength.

In the present work, our motivation is to investigate whether other types of robust light bullets with different features can be supported by the previous arrays. Actually, from the governing system derived by Leblond and Mihalache [14], we need to tread into its structural properties of integrability while performing the Weiss-Tabor-Carnevale approach [15] to such a problem and discuss in detail the existence of fractal solutions to the system.

Weiss, Tabor and Carnevale [15] developed one of the most powerful methods known as the Painlevé analysis [16] which is very useful in proving the integrability of a model system. Such an analysis is helpful in generating some exact solutions, no matter the model is integrable or not. Also, if ones wants only to prove the Painlevé property of a model, the use of Kruskal's simplification [17] for the WTC approach is also addressable. Thus, if we need to find some more information from the model, it is better to use the original WTC approach or some extended forms [18–21]. In this work, we combine the standard WTC approach [15] with the Kruskal's simplification [17] in view of simplifying the proof of the Painlevé integrability.

We organize the work as follows: in Section 2, we briefly present the physical background of the system under investigation. In Section 3, we perform the WTC method to the governing equations under study. Next, in Section 4, we take advantage of the arbitrary functions generated by the previous analysis to discuss some higher dimensional pattern formations of light bullets, namely the fractals. In the last section, we end with a brief conclusion.

2. Physical ground of light propagation within the carbon nanotube arrays

In a recent study, Belonenko et al. [22, 23] investigated both analytically and numerically the propagation of light bullets within an array of carbon nanotubes. They obtained an analytical function presenting some (2 + 1)-dimensional optical soliton with some diffraction displays in propagation. In view of suppressing the diffraction to obtain some robust light bullet waveform, the model is slightly modified [14] while deriving a new higher dimensional coupled system. Using the calibration $\mathbf{E} = -\partial \mathbf{A}/\partial t$, $\mathbf{E}$ and $\mathbf{A}$ being the electric field and the potential vectors, respectively, and variable t being the time, taking into account of the dielectric and magnetic properties of carbon nanotubes [24], the Maxwell equations reduce to the following system

$$\Delta \mathbf{A} - \mathbf{A}_{tt}/c^2 = -\mu_0 \mathbf{J}, \qquad (1)$$

where subscripts denote the partial derivatives. Constants μ_0 and c are magnetic permeability and light velocity in vacuum, respectively. We have neglected the diffraction blooming of the laser beam in the directions perpendicular to the propagation plane. The current $\mathbf{J}$ is directed along the axis of the nanotubes, i.e., $\mathbf{J} = J_z \mathbf{e}_z$, where unitary vector $\mathbf{e}_z$ spans the z-axis. Besides, we consider the case where the wave field is polarized in the same direction, and $\mathbf{A} = A\mathbf{e}_z$.

In order to determine the current, we use a semiclassical approximation [25] taking into account the dispersion law from the quantum-mechanical model and the evolution of the ensemble of particles by the classical Boltzmann kinetic equation in the approximation of relaxation time. It comes

$$f_t - qA_t f_p = (F_0 - f)/\tau, \qquad (2)$$

where constant q stands for the electron charge. The relaxation time τ can be assessed according to Ref. [26]. The quantity f is the distribution function of electrons in the nanotubes depending upon the time t and the momentum $p \equiv p\left(p_\varphi, p_z\right)$ of the electron. The azimuthal component p_φ reads $p_\varphi = s\Delta p_\varphi$, and the axial component p_z is merely denoted p below. It then appears that the integer s characterizes the momentum quantization transverse to the nanotube. We also mention that the function F_0 is the equilibrium value of the distribution f and is known as the Fermi-distribution function expressed as

$$F_0 = 1/[1 + \exp(E/k_B T_0)], \qquad (3)$$

in which quantities k_B, T_0, and E stand for the Boltzmann constant, the absolute temperature, and the energy in the conduction band, respectively. In account of the zigzag-type carbon nanotubes, the energy E is given by the Huckel π-electron approximation as follows

$$E = \gamma\sqrt{1 + 4\cos(ap)\cos(\pi s/m) + 4\cos^2(\pi s/m)}, \qquad (4)$$

with $\gamma = 2.7eV$ and $a = 3b/2\hbar$ where constant $b = 0.142nm$ represents the distance between the adjacent carbon atoms. Constant m is the number of hexagons in the perimeter of a nanotube. The surface current density J_s can hence be expressed as

$$J_s = \frac{2q}{2\pi\hbar}\int\int vf dp_\varphi dp, \qquad (5)$$

where the velocity v reads $v = \partial E/\partial p$. The distribution function f can be written as

$$f = \sum_s \Delta p_\varphi \delta\left(p_\varphi - s\Delta p_\varphi\right) f_s(p, t), \qquad (6)$$

with quantity f_s representing the longitudinal distribution function relative to the azimuthal quantum number s. The volume current density J is hence obtained as

$$J = \frac{Nq}{\pi\hbar}\sum_s \int vf_s dp, \qquad (7)$$

where constant N represents the surface density of nanotubes in the xy-plane.

We use the powerful reductive perturbation method in the short-wave approximation regime [13, 28]. Assuming that the typical duration of the pulse is very small with respect to τ and the propagation length is very long with respect to the wavelength, we introduce the fast and slow variables

$$\theta = (t - x/V)/\varepsilon, \quad \xi = \varepsilon x, \qquad (8)$$

in which the quantities ε and V denote the small perturbative parameter and the wave velocity, respectively. Accordingly, we address the following expansions

$$f_s = f_0 + \varepsilon f_1 + \cdots, \quad A = A_0 + \varepsilon A_1 + \cdots. \tag{9}$$

Thus, at leading order ε^{-1}, Eq. (2) yields

$$f_{0t} - qA_{0t}f_{0p} = 0, \tag{10}$$

in which solution f_0 reads $f_0 = \varphi(p + qA_0)$ with φ being an arbitrary function. However, at large t, the wave A vanishes and f_0 goes to its equilibrium value F_0. Thus, from Eq. (7), we write

$$J_0 = \frac{q}{\pi\hbar} \sum_s \int v(p + qA)f_0(p)dp. \tag{11}$$

Now, at leading order ε^{-2}, the Maxwell equations transform to

$$V = c. \tag{12}$$

The order ε^0 provides

$$(2/c)\partial^2 A_0/\partial\xi\partial\theta = \mu_0 J_0, \tag{13}$$

which, with Eq. (11), stands for the governing model system.

The energy E is of the same order of magnitude as γ. Calculating $\gamma/k_B = 3.1 \times 10^4 K$ shows that E is very large with respect to room temperature. Thus, only the levels with the lowest energy are excited. Let us seek for this minimum for a given parameter s. Hence, we find that

$$E_{min} = \gamma|1 - 2|\cos(\pi s/m)||, \tag{14}$$

for $p = \pm\pi/a$ when $\cos(\pi s/m) > 0$ and for $p = 0$ when $\cos(\pi s/m) < 0$. Thus, as s varies, the minimum of E_{min} is zero, i.e., $s/m = \pm 1/3$ or $s/m = \pm 2/3$. Therefore, for $m = 6$, $s = 2$ or $s = 4$. Besides, in other nanotubes, there is a nonzero gap between valence and conduction bands. The gap is so great that the conductivity is very low. Hence, only the nanotubes where m is multiple of 3 contributes. In this sense, the expression of $E_s(p)$ reads

$$E_s = 2\gamma|\cos(ap/2)|, \tag{15}$$

for $s/m = 1/3$ and

$$E_s = 2\gamma|\sin(ap/2)|, \tag{16}$$

for $s/m = 2/3$. Calculating the velocity $v = \partial E/\partial p$, where variable p is substituted by $p - qA_0$, and considering the value at which the minimum is reached, we get

$$v = -a\gamma\,\text{sgn}\left(\sin(aqA_0/2)\right)\cos(aqA_0/2), \tag{17}$$

where $\text{sgn}(X)$ denotes the sign of X in both cases.

The current J_0 can hence be expressed as

$$J_0 = -Q \, \text{sgn} \left(\sin \left(aqA_0/2 \right) \right) \cos \left(aqA_0/2 \right), \tag{18}$$

where $Q = (4Nq\gamma/\pi\hbar)\Phi(\gamma/k_BT_0)$. The function Φ reads

$$\Phi(X) = \int_{-\pi/2}^{\pi/2} dx/[1 + \exp \left(2X|\sin x|\right)]. \tag{19}$$

Inserting Eq. (18) into (13) yields the evolution equation. As a matter of illustration, we assume that $0 < aqA_0/2 < \pi$ and define A_0' such that $aqA_0'/2 = aqA_0/2 - \pi/2$. Hence, we obtain

$$\partial^2 A_0'/\partial\xi\partial\theta = -R \sin \left(aqA_0'/2 \right), \tag{20}$$

with $R = (2Nq\gamma/\pi\varepsilon_0\hbar c)\Phi(\gamma/k_BT_0)$. Assuming $|aqA_0/2|>\pi$, we can set $A_0'' = A_0 + \pi/aq$. Therefore, Eq. (20) remains. This shows that Eq. (20) is valid for any A_0. Retaining the second transverse derivative in the wave Eq. (13), we derive the following

$$\partial^2 A_0'/\partial\xi\partial\theta = (c/2)\partial^2 A_0'/\partial y^2 - R \sin \left(aqA_0'/2 \right), \tag{21}$$

which can be known as the two-dimensional sine-Gordon equation. Eq. (21) can be written as

$$A_T = -BC, \quad C_T = AB, \quad B_Z = C + \int^T B_{YY}dT, \tag{22}$$

provided $B = E_0/E_r$, $Z = x/L_r$, $T = (t - x/c)/t_r$, and $Y = y/w_r$, with $E_r = 2/(aqt_r)$, $L_r = -UE_r/R$, and $w_r = \sqrt{ct_rL_r/2}$. The assumption $\lim_{T\to-\infty}A = U$ is regarded. The system (22) has been investigated by means of a modified Euler scheme in Z in each substep of which the equations relative to the variable T are solved by a scheme of the same type [14]. Unlikely, we develop an analytical scheme known as the WTC formalism in view of studying the full integrability of the system above while unearthing other kinds of light bullet waveforms with compact supports.

3. Painlevé analysis

According to the standard WTC method [15], if equation Eq. (22) is Painlevé integrable, then all the possible solutions of the system can be written in the full Laurent series as follows

$$A = \sum_{k=0}^{\infty} A_k g^{k+\alpha}, \quad B = \sum_{k=0}^{\infty} B_k g^{k+\beta}, \quad C = \sum_{k=0}^{\infty} C_k g^{k+\gamma}, \tag{23}$$

with sufficient arbitrary functions among A_k, B_k, C_k, and g, where $g = g(Y,Z,T)$, $A_k = A_k(Y,Z,T)$, $B_k = B_k(Y,Z,T)$, and $C_k = C_k(Y,Z,T)$ (k being nonzero integers) are analytical functions within the neighborhood of $g = 0$. The constants α, β, and γ should all be negative integers.

The leading order analysis provides the following

$$\alpha = \gamma = -2, \quad \beta = -1 \tag{24}$$

and

$$A_0 = 2\big(g_Z g_T - g_Y^2\big), \quad B_0 = 2i\varepsilon g_T, \quad C_0 = -i\varepsilon A_0, \tag{25}$$

where $\varepsilon = \pm 1$ and $i^2 = -1$.

In order to obtain the recursion relations to determine the functions A_k, B_k, and C_k, we substitute Eqs. (23)–(25) into (22). This leads us to the following algebraic system

$$\mathcal{M}_k \mathcal{V}_k = \mathcal{T}_k, \tag{26}$$

where $\mathcal{M}_k$ is a square matrix, $\mathcal{V}_k = (A_k, B_k, C_k)^T$, and $\mathcal{T}_k = (\mathcal{A}_k, \mathcal{B}_k, \mathcal{C}_k)^T$ with

$$
\begin{aligned}
\mathcal{A}_k = {}& -B_{k-2,\,ZT} + B_{k-2,\,YY} \\
& - (k-2)\big[B_{k-1,\,Z}g_T + B_{k-1,\,T}g_Z - 2B_{k-1,\,Y}g_Y + B_{k-1}\big(g_{ZT} - g_{YY}\big)\big] \\
& + \sum_{j=1}^{k-1} A_j B_{k-j},
\end{aligned} \tag{27}
$$

and

$$\mathcal{B}_k = -A_{k-1,\,T} - \sum_{j=1}^{k-1} C_j B_{k-j}, \tag{28}$$

with

$$\mathcal{C}_k = -C_{k-1,\,T} + \sum_{j=1}^{k-1} A_j B_{k-j}, \tag{29}$$

provided $A_k = B_k = C_k = 0$ for $k < 0$. The matrix $\mathcal{M}_k$ is given by

$$
\mathcal{M}_k = \begin{pmatrix}
-B_0 & k(k-3)A_0/2 & 0 \\
(k-2)g_T & C_0 & B_0 \\
-B_0 & -A_0 & (k-2)g_T
\end{pmatrix}. \tag{30}
$$

Thus, the determinant Δ_k of the matrix $\mathcal{M}_k$ is given by

$$\Delta_k = -(k+1)(k-2)(k-2)(k-4)\big(g_Z g_T - g_Y^2\big)g_T^2. \tag{31}$$

If the determinant Δ_k of the cœfficient matrix $\mathcal{M}_k$ is not equal to zero, then the functions A_k, B_k, and C_k can be obtained from Eq. (26) straightforwardly as unique solutions. Nonetheless, when

$$k \in \{-1, 2, 2, 4\}, \tag{32}$$

resonances occur.

The resonance at $k = -1$ corresponds to the singularity manifold g, which is an arbitrary function, and the case $k = 0$, which is then satisfied identically by the leading order analysis provided by Eq. (25). If the model is Painlevé integrable, we require two resonance conditions at $k = 2; 4$, which are satisfied identically such that the other four arbitrary functions among A_k, B_k, and C_k can be introduced into the general series expansion given by Eq. (23).

For $k = 1$, we can easily obtain from Eq. (26)

$$
\begin{aligned}
A_1 &= \frac{\iota\varepsilon\left[{}_{gT}B_{0,Z} + {}_{gZ}B_{0,T} - 2{}_{gY}B_{0,Y} + {}_{(gZT-gYY)}B_0 + C_{0,T}\right]}{gT}, \\
B_1 &= \frac{{}_{gT}B_{0,Z} + {}_{gZ}B_{0,T} - 2{}_{gY}B_{0,Y} + {}_{(gZT-gYY)}B_0 + 2C_{0,T}}{A_0}, \\
C_1 &= -\iota\varepsilon A_1.
\end{aligned}
\tag{33}
$$

On the other hand, solving the case for $k = 2$, the following resonance condition is derived

$$
-B_{0,ZT} + B_{0,YY} + C_{1,T} = 0.
\tag{34}
$$

It is straightforward to see that the resonance condition given by Eq. (34) is satisfied identically because of Eqs. (25) and (33). Then, we have, after solving Eq. (26),

$$
B_2 = \frac{C_{1,T} - A_1 B_1 - B_0 A_2}{A_0}, \quad C_2 = -\iota\varepsilon A_2,
\tag{35}
$$

where one of the quantities among A_2 and C_2 is arbitrary.

For $k = 3$, Eq. (26) gives us

$$
\begin{aligned}
A_3 &= \frac{\iota\varepsilon}{2gT}\left[-B_{1,ZT} + B_{1,YY} - {}_{gT}B_{2,Z} - {}_{gZ}B_{2,T} + 2{}_{gY}B_{2,Y}\right] \\
&\quad + \frac{\iota\varepsilon}{2gT}\left[-{}_{(gZT-gYY)}B_2 + A_1 B_2 + A_2 B_1\right] \\
B_3 &= \frac{1}{2A_0}\left[-3B_{1,ZT} + 3B_{1,YY} - 3{}_{gT}B_{2,Z} - 3{}_{gZ}B_{2,T} + 6{}_{gY}B_{2,Y}\right] \\
&\quad + \frac{1}{2A_0}\left[-3{}_{(gZT-gYY)}B_2 + 2C_{2,T} + A_1 B_2 + A_2 B_1\right], \\
C_3 &= -\iota\varepsilon A_3.
\end{aligned}
\tag{36}
$$

Let us emphasize that $\partial_g/\partial_T \equiv gT$, and so on.

For $k = 4$, we can obtain

$$
A_4 = \frac{\iota\varepsilon}{6g_T}\left(\mathcal{A}_4 + 2C_4 - 4g_T C_4\right), \quad B_4 = \frac{1}{3A_0}\left(\mathcal{A}_4 - C_4 + 2g_T C_4\right),
\tag{37}
$$

where C_4 is an arbitrary function.

Nevertheless, let us make a remark that throughout the above study, the following relations are derived:

$$
\mathcal{B}_k - \iota\varepsilon\mathcal{C}_k = 0, \ (k = 1, 2, 3, 4).
\tag{38}
$$

Then, for $k = 4$, Eq. (38) verifies the resonance condition. All of the resonance conditions with four arbitrary functions are satisfied identically. Hence, the system (22) is Painlevé integrable. Its complete integrability will be established if some other essential properties such as the Bäcklund transformation (BT) and the Hirota bilinearization [27–30] are derived.

The Painlevé analysis can also be used to obtain other interesting properties [15] of the (2 + 1)-dimensional coupled system above. In this work, we use the standard

truncation of the WTC expansion to obtain the BT and the Hirota bilinearization [27–30] of the system (22). By setting

$$A_{k+1} = B_k = C_{k+1} = 0, \quad for \quad k \geq 2, \tag{39}$$

Eq. (23) with (24) becomes a standard truncated expansion

$$A = A_0/g^2 + A_1/g + A_2, \quad B = B_0/g + B_1, \quad C = C_0/g^2 + C_1/g + C_2. \tag{40}$$

After vanishing A_3 and B_3, and using Eq. (38), we can reduce the system (36) to

$$B_{1,ZT} = A_2 B_1 + B_{1,YY}, \quad A_{2,T} = -B_1 C_2, \quad C_{2,T} = A_2 B_1. \tag{41}$$

From Eq. (41), it follows that A_2, B_1, C_2 is a solution of the system (22). Besides, the truncated expansion Eq. (40) actually stands for a BT. Generally, in order to construct a typical family of solution to Eq. (22) in a simple manner, it is useful to consider very simple expressions of $A_2, B_1,$ and C_2. For convenience, we fix the original seed solution as

$$A_2 = \nu, \quad B_1 = 0, \quad C_2 = -\iota\varepsilon\nu, \tag{42}$$

with parameter ν being an arbitrary constant. The seed solution is actually used for constructing many other solutions. However, many other classes of solutions are obtained for other existing seed solutions. It is that property of the Painlevé approach for constructing various kinds of solutions by means of arbitrary functions that makes it potential and powerfully underlying. The solutions are given by Eq. (40) expressed in a truncated form. Many solutions are constructed in a straightforward way due to the arbitrariness of these functions, provided to solve analytically or numerically some nonlinear partial differential constraint equations.

Substituting the BT from Eq. (40) and using the Eq. (42) into Eq. (22), we derive some bilinear equations which can be decoupled as

$$\begin{aligned} D_Z D_T H \cdot F &= v_1 HF, \quad D_Y D_T H \cdot F = -v_2 HF, \quad D_Y^2 H \cdot F = -v_2 HF, \\ D_Y D_T F \cdot F &= H^2/2, \quad D_T^2 F \cdot F = H^2/2, \quad D_Y^2 F \cdot F = H^2/2, \end{aligned} \tag{43}$$

provided $A = D_Z + E_Y$ and $C \propto (B_Z - B_Y)$ so as to express

$$B = H/F, \quad D = \nu_1 Z - 2\partial_T \ln(F), \quad E = \nu_2 Y + 2\partial_Y \ln(F), \tag{44}$$

with $\nu = \nu_1 + \nu_2$. The symbols $D_Y, D_Z,$ and D_T refer to the Hirota operators [29–31] with respect to the variables $Y, Z,$ and T, respectively. According to the usual procedure, the dependent function is expanded into suitable power series of a perturbation parameter and using them in Eq. (43), we can straightforwardly construct the one-, two- and N-soliton solutions (N being an integer) to Eq. (22). Nevertheless, the investigation of these solutions will be studied in detail in a separate paper. Now, knowing the BT and the related Hirota bilinearization of Eq. (22), we can conclude that the $(2 + 1)$-dimensional system above is completely integrable.

After substitution Eqs. (25) and (33) into (40), we find

$$A = \nu + \frac{(D_Y^2 - D_Z D_T)g \cdot g}{g^2}, \quad B = 2\iota\varepsilon\partial_T(\ln|g|), \quad C = -\iota\varepsilon A. \tag{45}$$

In the next section, because of the arbitrariness of some functions derived from the Painlevé analysis, we aim at focusing our interest to solutions for which the quantities A and B are expressed in the reduction form Eq. (45). In order to express some exact solutions of our initial coupled evolution system, we consider the general ansatz for the function g in the form

$$g = a_0 + a_1 P + a_2 Q + a_3 PQ, \qquad (46)$$

where the parameter $a_k (k = 0, 1, 2, 3)$ is an arbitrary constant and $P = P(Z, T)$ and $Q = Q(Y, T)$ are arbitrary functions of (Z, T) and (Y, T), respectively.

4. Discussion of some higher dimensional solutions

With this aim, we follow the method developed by Tang and Lou [32] for generating some families of diverse pattern formations while using the arbitrary functions g expressed previously.

Let us mention that for some convenience, we rewrite the variables X, Y, and T into their lower cases. Paying particular attention to fractal pattern formations, based upon the previous works carried out on the subject, we classify the above waves according to the different expressions of the generic lower dimensional function Θ of two generalized coordinates (ξ, t) as defined by [33].

1. *Nonlocal fractal pattern:* we have the following

$$\Theta(\xi, t) = \sum_{j=1}^{2} \lambda_j \theta_j |\theta_j| \left\{ \left\{ \alpha_j \sin \left[\ln \left(\theta_j^2 \right) \right] + \beta_j \cos \left[\ln \left(\theta_j^2 \right) \right] \right\} \right\}, \qquad (47)$$

provided quantities θ_{0j}, λ_j, α_j, and β_j being arbitrary parameters. Also, $\theta_j \equiv k_j \xi - v_j t + \theta_{0j}$. Variables ξ, k_j, and v_j are spacelike-defined, wave number, and velocity of the j-wave component, respectively.

2. *Fractal dromiom pattern*: the dromion-like (lump-like) structure is exponentially (algebraically) localized on a large scale and possesses self-similar structure near the center of the pattern. The function Θ can be expressed as

$$\Theta(\xi, t) = \exp \left\{ -|\theta| \overline{N} \left\{ r + s \sin \left[\ln \left(\theta^2 \right) \right] + w \cos \left[\ln \left(\theta^2 \right) \right] \right\} \right\}, \qquad (48)$$

with $\theta_j \equiv k\xi - vt + \theta_{0j}$, θ_0 being an arbitrary parameter, and constants $\overline{N}$, r, w, and s are arbitrary parameters. But also we can find

$$\Theta(\xi, t) = |\theta| \left\{ \overline{\alpha} \sin \left[\ln \left(\theta^2 \right) \right] + \overline{\beta} \cos \left[\ln \left(\theta^2 \right) \right] \right\} \tilde{N} / (1 + \theta^4), \qquad (49)$$

for fractal lump solution. Constants $\overline{\alpha}$, $\overline{\beta}$, and $\tilde{N}$ are arbitrary parameters.

3. *Stochastic fractal pattern*: Such typical excitation is expressed through the differentiable Weierstrass function $\wp$ defined as

$$\wp(\xi, t) = \sum_{j=0}^{N} \alpha^{-j/2} \sin \left(\beta^j \theta \right), N \to \infty, \qquad (50)$$

with constants α and β being arbitrary parameters. A stochastic fractal excitation can be expressed as

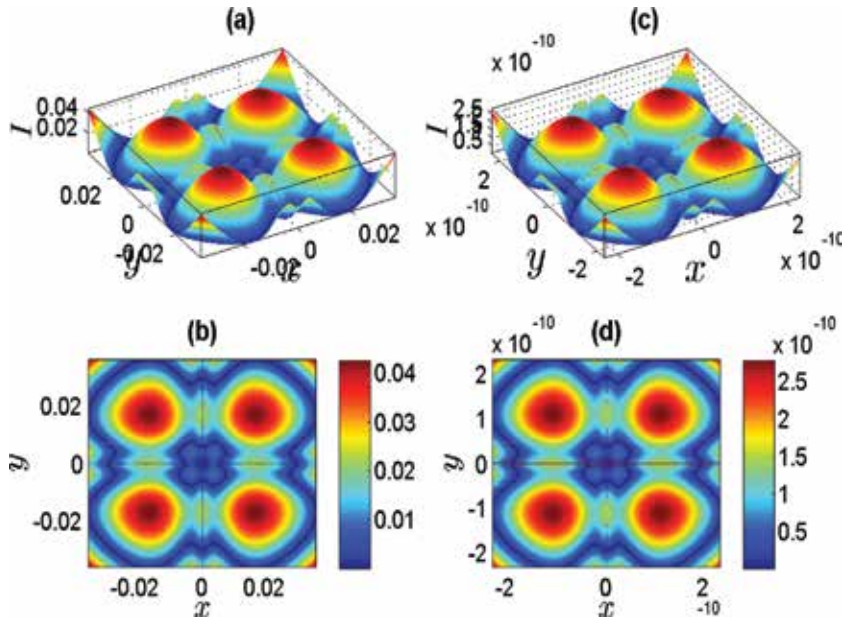$$\Theta(\xi, t) = \sum_{i,j} R_i(\theta_i) R_j(\theta_j), \qquad (51)$$

Figure 1.
Depiction of Nonlocal fractal patterns at $t = 0$. The parameters are chosen as $a_0 = 1$, $a_1 = 1$, $a_2 = 1$, and $a_3 = 1$ such that: For $p(x,t) = \Theta(x,t)$, $\lambda_1 = 1/4$, $\lambda_2 = 0$, $\theta_{01} = 0$, $k_1 = 1$, and $v_1 = 1$. For $q(y,t) = \Theta(y,t)$, $\lambda_1 = 1/4$, $\lambda_2 = 0$, $\theta_{02} = 0$, $k_2 = 1$, and $v_2 = 1$. Note that $\alpha_1 = 1$ and $\beta_1 = 0$. Panels (a) and (c) represent the pattern formations depicted in 3D-perspective, and the two others (b) and (d) are their corresponding densities represented within the square regions $\left[-3.6 \cdot 10^{-2}, 3.6 \cdot 10^{-2}\right]^2$ and $\left[-2.32 \cdot 10^{-10}, 2.32 \cdot 10^{-10}\right]^2$, respectively.

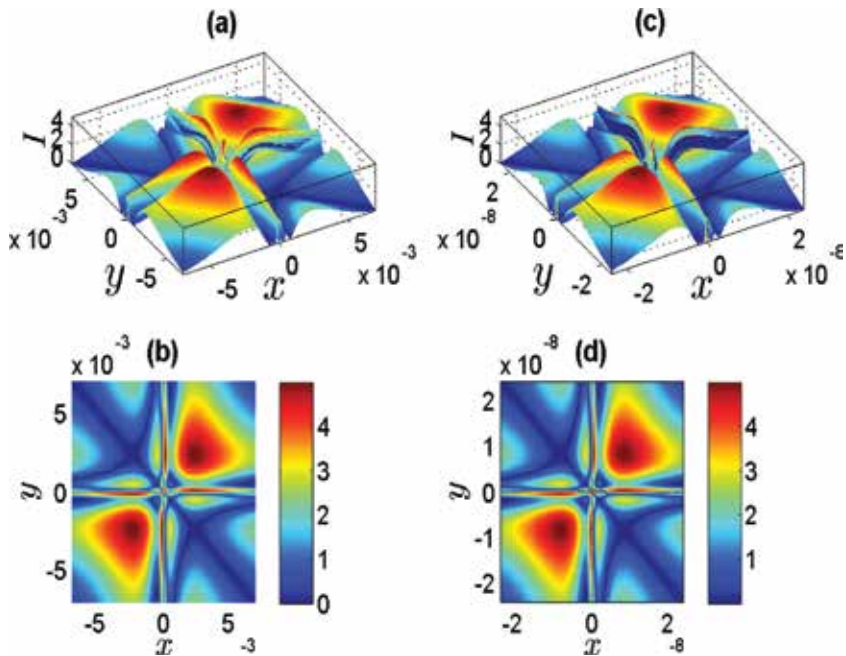**Figure 2.**
Fractal dromiom excitations depicted at $t = 0$ by the observable $|B| \equiv I$ which expression is given by Eq. (40). In this case, the parameters are selected as $a_0 = 1$, $a_1 = 1$, $a_2 = 1$, and $a_3 = 1$ such that: For $p(x,t) = \Theta(x,t)$, $r = 3/2$, $s = 1$, $w = 0$, $N = 1$, $\theta_{01} = 0$, $k_1 = 1$, and $v_1 = 1$. For $q(y,t) = \Theta(y,t)$, $\theta_{02} = 0$, $k_2 = 1$, and $v_2 = 1$. Panels (a) and (c) represent the pattern formations depicted in 3D-perspective, and the two others (b) and (d) are their corresponding densities represented within the square regions $\left[-7 \cdot 10^{-3}, 7 \cdot 10^{-3}\right]^2$ and $\left[-2.8 \cdot 10^{-8}, 2.8 \cdot 10^{-8}\right]^2$, respectively.
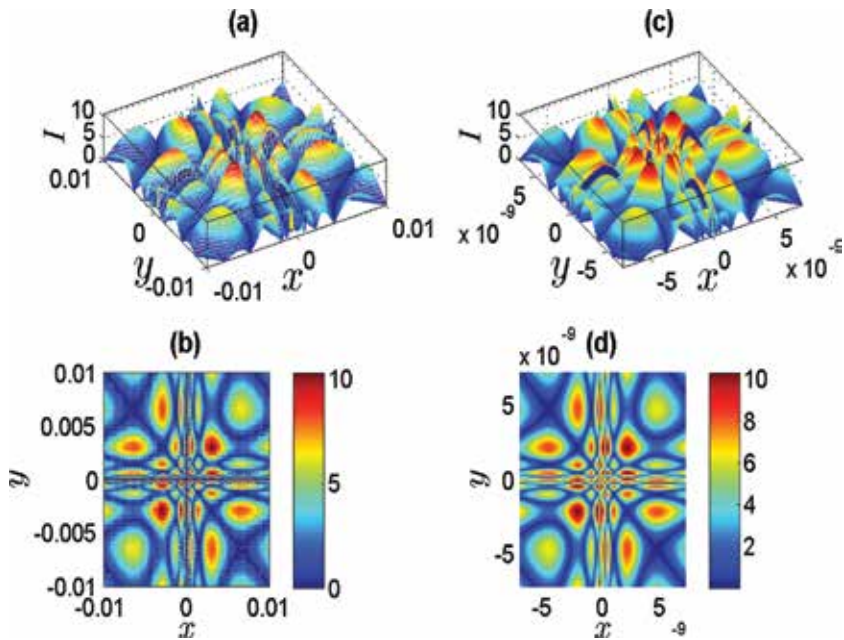
Figure 3.
Fractal lump excitations depicted at $t = 0$ by the observable $|\mathbf{B}| \equiv I$ which expression is given by Eq. (40). In this case, the parameters are selected as $a_0 = 1$, $a_1 = 1$, $a_2 = 1$, and $a_3 = 2$ such that: For $p(x,t) = \Theta(x,t)$, $\theta_{01} = 0$, $k_1 = 1$, and $v_1 = 1$. For $q(y,t) = \Theta(y,t)$, $\theta_{02} = 0$, $k_2 = 1$, and $v_2 = 1$. Note that $\bar{\alpha} = 1$, and $\bar{\beta} = 0$. Panels (a) and (c) represent the pattern formations depicted in 3D-perspective, and the two others (b) and (d) are their corresponding densities represented within the square regions $\left[-3.6 \cdot 10^{-2}, 3.6 \cdot 10^{-2}\right]^2$ and $\left[-2.32 \cdot 10^{-10}, 2.32 \cdot 10^{-10}\right]^2$, respectively.
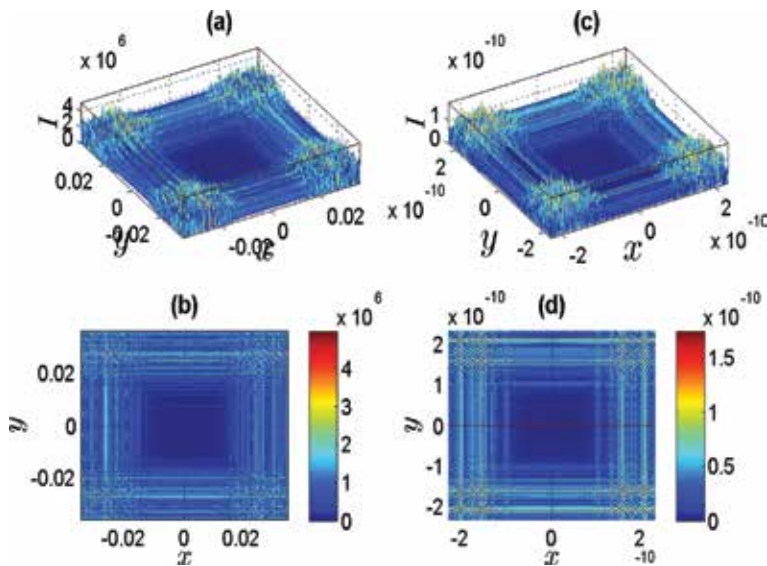

Figure 4.
Fractal stochastic nonlocal excitations depicted at $t = 0$ by the observable $|\mathbf{B}| \equiv I$ which expression is given by Eq. (40). In this case, the parameters are selected as $a_0 = 1$, $a_1 = 1$, $a_2 = 1$, and $a_3 = 1$ such that: For $p(x,t) = \Theta(x,t)$, $\lambda_1 = 1/4$, $\lambda_2 = 0$, $\theta_{01} = 0$, $k_1 = 1$, and $v_1 = 1$. For $q(y,t) = \Theta(y,t)$, $\lambda_1 = 1/4$, $\lambda_2 = 0$, $\theta_{02} = 0$, $k_2 = 1$, and $v_2 = 1$. Note that $\alpha = 3/2$, $\beta = 3/2$, and $N = 100$. Panels (a) and (c) represent the pattern formations depicted in 3D-perspective, and the two others (b) and (d) are their corresponding densities represented within the square regions $\left[-3.6 \cdot 10^{-2}, 3.6 \cdot 10^{-2}\right]^2$ and $\left[-2.32 \cdot 10^{-10}, 2.32 \cdot 10^{-10}\right]^2$, respectively.

where $R_i = \wp(\theta_i) + \theta_i^2 + \mu_i$, with μ_i standing for arbitrary parameter.

Stochastic fractal dromion/solitoff excitations: such structures are obtained by including the Weierstrass function into the dromiom solution. Especially for solitoff excitations, we can try the following:

$$\Theta(\xi, t) = k + \sum_{j=0} \eta_j \wp(\theta_j) \tanh^{\mu_j}(\theta_j),\tag{52}$$

provided quantities k, η_j, and μ_j being arbitrary parameters.

Stochastic fractal lump pattern: Eq. (51) is reduced as

$$\Theta(\xi, t) = \sum_{i,j} \rho_j R_j(\theta_j),\tag{53}$$

where quantities η_j and ρ_j being arbitrary parameter.

Now, let us analyze different figures with respect to the previous classifications. Thus, in **Figure 1**, we depict the variations of the $|\mathbf{B}|$-observable with space at $t = 0$.

In a $3D-$representation, the features presented in panel 1(a) within the space region $[-3.6 \cdot 10^{-2}, 3.6 \cdot 10^{-2}]^2 \times |\mathbf{B}|$ and those depicted in (c) within region $[-2.32 \cdot 10^{-10}, 2.32 \cdot 10^{-10}]^2 \times |\mathbf{B}|$ are self-similar nonlocal. Such a similarity in the profiles is clearly shown in panels (b) and (d) standing for their density plots, respectively.

Following the above figure, in **Figure 2**, we generate the fractal dromiom depicting self-similar structure with density plots represented in panels (b) and (d), respectively. In comparison to the previous nonlocal fractal patterns, it appears that the fractal dromions have relatively high amplitudes.
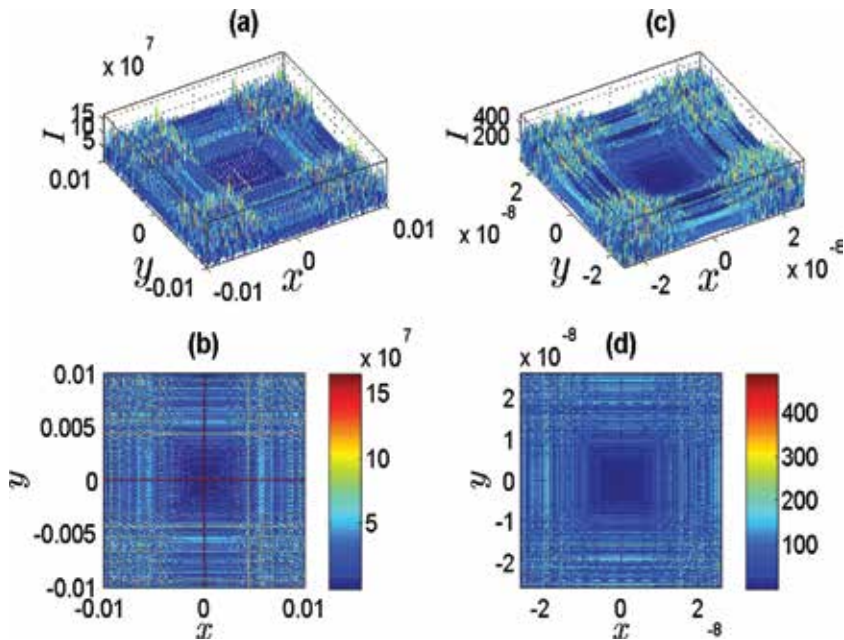

Figure 5.
Fractal stochastic dromion excitations depicted at $t = 0$ by the observable $|\mathbf{B}| \equiv I$ which expression is given by Eq. (40). In this case, the parameters are selected as $a_0 = 1$, $a_1 = 1$, $a_2 = 1$, and $a_3 = 1$ such that: For $p(x, t) = \Theta(x, t)$, $r = 3/2$, $s = 1$, $w = 0$, $\overline{N} = 1$, $\theta_{01} = 0$, $k_1 = 1$, and $v_1 = 1$. For $q(y, t) = \Theta(y, t)$, $\theta_{02} = 0$, $k_2 = 1$, and $v_2 = 1$. Note that $\alpha = 3/2$, $\beta = 3/2$, and $N = 100$. Panels (a) and (c) represent the pattern formations depicted in 3D-perspective, and the two others (b) and (d) are their corresponding densities represented within the square regions $[-1 \cdot 10^{-2}, 1 \cdot 10^{-2}]^2$ and $[-2.6 \cdot 10^{-8}, 2.6 \cdot 10^{-8}]^2$, respectively.

Next, in **Figure 3**, we obtain the fractal lump which shows self-similar structures in panels (c) and (d).

In addition to the above self-similar regular fractal dromion and lump excitations, by using the lower dimensional stochastic fractal functions, we construct some other higher dimensional stochastic fractal patterns. Thus, in **Figure 4**, we generate a typical stochastic fractal nonlocal pattern with self-similarity in structure.

Besides, in **Figure 5**, with the selecting parameters and suitable choices of lower dimensional arbitrary stochastic fractal dromion function as presented in the captions of these figures, we obtain higher dimensional stochastic dromion excitations. The self-similarity in structure of the observable $I \equiv |\mathbf{B}|$ shows how the peaks are distributed stochastically within the regions $\left[-1 \cdot 10^{-2}, 1 \cdot 10^{-2}\right]^2$ and $\left[-2.6 \cdot 10^{-8}, 2.6 \cdot 10^{-8}\right]^2$ for stochastic fractal dromion.

In **Figure 6**, we construct the fractal solitoff excitations. By reducing the region $\left[-1.2 \cdot 10^{-2}, 1.2 \cdot 10^{-2}\right] \times [-5, 10]$ of panel 6(a) to $\left[-1.5 \cdot 10^{-8}, 1.5 \cdot 10^{-8}\right] \times [-5, 10]$ of panel 6(c), we obtain a totally similar structure with density plots represented in panels (b) and (d), respectively.

In **Figure 7** with the selecting parameters and suitable choices of lower dimensional arbitrary stochastic fractal lump function as presented in the captions of the figure, we obtain higher dimensional stochastic lump excitations. Through the panels (7(a) and 7(b)) depicting the variations of $|\mathbf{B}|-$observable, at $t = 0$, the self-similarity in structure of this observable shows how the peaks are distributed stochastically within the regions $\left[-7 \cdot 10^{-3}, 7 \cdot 10^{-3}\right]^2$ and $\left[-2.1 \cdot 10^{-10}, 2.1 \cdot 10^{-10}\right]^2$. In the above configurations, the stochastic fractal solitoff
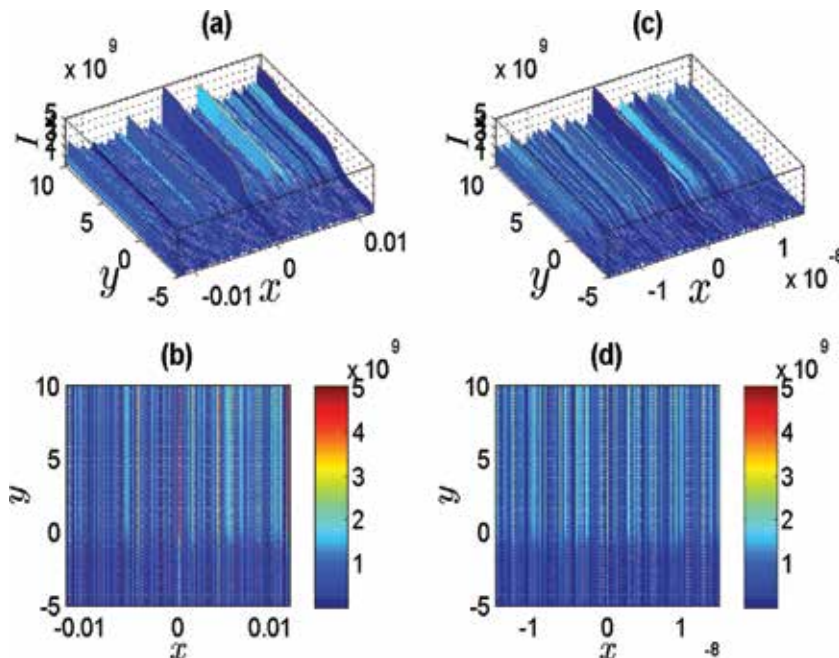

Figure 6.
Fractal stochastic solitoff excitations depicted at $t = 0$ by the observable $|\mathbf{B}| \equiv I$ which expression is given by Eq. (40). In this case, the parameters are selected as $a_0 = 1$, $a_1 = 1$, $a_2 = 1$, and $a_3 = 1$ such that: For $p(x, t) = \Theta(x, t)$, $\kappa = 2$, $M = 1$, $\eta_0 = 0$, $\eta_1 = 1/2$, $\eta_m = 0 (m \geq 2)$, $\mu_1 = 1$, $\theta_{01} = -20$, $k_1 = 4$, and $v_1 = 1$. For $q(y, t) = \Theta(y, t)$, $\kappa = 0$, $M = 2$, $\eta_0 = 0$, $\eta_1 = 1/5$, $\eta_2 = 1/4$, $\eta_m = 0 (m \geq 3)$, $\mu_1 = \mu_1 = 1$, $\theta_{02} = -15$, $k_2 = 2$, and $v_2 = 2$. Note that $\alpha = 3/2$, $\beta = 3/2$, and $N = 100$. Panels (a) and (c) represent the pattern formations depicted in 3D-perspective, and the two others (b) and (d) are their corresponding densities represented within the square regions $\left[-1.2 \cdot 10^{-2}, 1.2 \cdot 10^{-2}\right] \times [-5, 10]$ and $\left[-1.5 \cdot 10^{-8}, 1.5 \cdot 10^{-8}\right] \times [-5, 10]$, respectively.
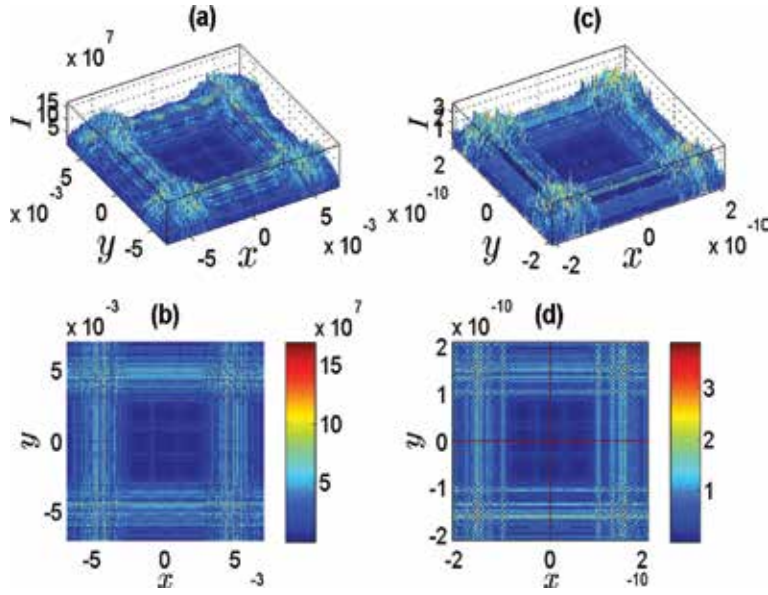
Figure 7.
Fractal stochastic lump excitations depicted at $t = 0$ by the observable $|B| \equiv I$ which expression is given by Eq. (40). In this case, the parameters are selected as $a_0 = 1$, $a_1 = 1$, $a_2 = 1$, and $a_3 = 2$ such that: For $p(x,t) = \Theta(x,t)$, $\theta_{01} = 0$, $k_1 = 1$, and $v_1 = 1$. For $q(y,t) = \Theta(y,t)$, $\theta_{02} = 0$, $k_2 = 1$, and $v_2 = 1$. Note that $\bar{\alpha} = 1$, $\bar{\beta} = 0$, $\tilde{N} = 2$ associated to $\alpha = 3/2$, $\beta = 3/2$, and $N = 100$. Panels (a) and (c) represent the pattern formations depicted in 3D-perspective, and the two others (b) and (d) are their corresponding densities represented within the square regions $\left[-7 \cdot 10^{-3}, 7 \cdot 10^{-3}\right]^2$ and $\left[-2.1 \cdot 10^{-10}, 2.1 \cdot 10^{-10}\right]^2$, respectively.

and stochastic fractal lump excitations appear to be the waves with greater amplitudes in comparison to the previous ones.

From a physical viewpoint, the observable B which has the meaning of the dimensionless electric field shows that its intensity $|B|$ can be nonlocal or rather self-confined. Actually, the intensity of the electromagnetic wave propagating along the carbon nanotube arrays is compact within the arrays. The previous study has revealed that the light bullet intensity describes a fractal-like excitation which provides more insights into the structural dynamics of the system under investigation.

5. Summary

Throughout the present work, we investigated the formation of fractal ultra-short spatiotemporal optical waveforms in arrays of carbon nanotubes. We followed the short-wave approximation to derive a generic (2+1)-dimensional coupled system. Such a coupled system was constructed via the use of the reductive perturbation analysis for the Maxwell equations and for the corresponding Boltzmann kinetic equation of the distribution function of electrons in the carbon nanotubes. Prior to the construction of different solutions to the previous coupled equations, we first studied the integrability of the governing system within the viewpoint of WTC formalism [15]. Thus, we investigated the singularity structure of the system. In this analysis, we expanded the different observables in the form of the Laurent series. Therefore, we found the leading order terms useful to solve the recurrent system. Solving this last system, we unearthed the different resonances of the governing equations. At the end, we found that the number of resonances balances seemingly the number of arbitrary functions in such a way that the governing system has sufficient and enough arbitrary functions. Hence, we derived that the

system is Painlevé integrable [15]. We derived another important properties, namely the Bäcklund transformation and the Hirota bilinearization [27–30] while establishing the complete integrability of the system.

In the wake of the result obtained from the WTC approach of integrability, we took advantage of the existence of some arbitrary functions to construct some interesting solutions such as fractals. Actually, following the investigation of fractals in many physical systems [31–33], we constructed some localized nonlinear excitations with some fractal support. As a result, we found the following typical features: the fractal dromion, the fractal lump, the stochastic and nonlocal fractal excitations.

One of the advantages of the WTC method discussed in this work is the generation of arbitrary functions useful in constructing many kinds and different solutions to the governing system. From such property endowing the method with the powerfulness, it would be rather interesting again to construct other types of nonlinear excitations such as the bubbles, the solitoffs, the dromions, the peakons, the fractals, among others [34–37]. These typical excitations would be useful in the understanding, more deeply, of the interaction between light incident excitations and carbon nanotubes for some practical issues in nanomechanical, nanoelectronic, and nanophotonic devices, alongside some emerging applications exploiting the good thermal and electronic conductivities of carbon nanotubes in some flat panel displays and field-effect transistors, among others.

Also, we intend using the WTC method in order to discover more other interesting properties still unknown in the carbon nanotube arrays. Previously, we discovered the properties of compactons in CNT [38]. The different properties will allow us in the future to improve the different uses of carbon nanotube in different areas of life. Moreover, because of these electrical and mechanical properties (very resistant, flexible, and lightweight), they are very suitable for the design of pressure sensors. These could be used by engineers to prevent structural collapses in civil engineering. They will have to measure either the pressure or the shear. Similarly, these sensors can be used in medicine while incorporating the system in textiles for better follow-up of patients or in a shoe sole. In another view, the sensors will have to be able to perform a good measure of the desired size. So to refine the design of these sensors, it will be essential to get even more information about this material. By discovering more properties of the material, we will know more how to exploit it in a safe way in all the various disciplines combining research and innovation.

Author details

Raïssa S. Noule and Victor K. Kuetche*
National Advanced School of Engineering, University of Yaounde I, Cameroon

*Address all correspondence to: vkuetche@yahoo.fr

IntechOpen

References

[1] Saito R, Dresselhaus G, Dresselhaus MS. Physical Properties of Carbon Nanotubes. London: Imperial College Press; 1998

[2] Dresselhaus S, Dresselhaus G, Eklund PC. Science of Fullerenes and Carbon Nanotubes. New York: Academic; 1996

[3] Charlier J-C, Blase X, Roche S. Reviews of Modern Physics. 2007;**79**:677

[4] Iijima S. Nature (London). 1991;**354**:56

[5] Ebbesen TW, Ajayan PM. Nature (London). 1992;**358**:220

[6] Iijima S, Ichihashi T. Nature (London). 1993;**363**:603

[7] Flach S, Willis CR. Physics Reports. 1998;**295**:182

[8] Campbell DK, Flach S, Kivshar YS. Physics Today. 2004;**57**:43

[9] Savin AV, Kivshar YS. Europhysics Letters. 2008;**82**:66002

[10] Leblond H, Veerakumar V. Physical Review B. 2004;**70**:134413

[11] Yanyushkina NN, Belonenko MB, Lebedev NG. Optika i Spektroskopiya. 2011;**111**:92 [Optics and Spectroscopy. 2011;**111**:85]

[12] Belonenko MV, Lebedev NG, Yanyushkina NN. Fizika Tverdogo Tela. 2012;**54**:162 [Physics of the Solid State. 2012;**54**:174]

[13] Harris P. Carbon Nanotubes and Related Structures. New Materials for the Twenty-First Century. New York: Cambridge University; 1999 and Moscow: Tekhnosfera; 2003

[14] Leblond H, Mihalache D. Physical Review A. 2012;**86**:043832

[15] Weiss J, Tabor M, Carnevale G. Journal of Mathematical Physics. 1983; **24**:522

[16] Ramani A, Grammaticos B, Bountis T. Physics Reports. 1989;**180**:159

[17] Jimbo M, Kruskal MD, Miwa T. Physics Letters A. 1982;**92**:59

[18] Fordy AP, Pickering A. Physics Letters A. 1991;**160**:347

[19] Conte R. Physics Letters A. 1989; **140**:383

[20] Lou S-y. Physical Review Letters. 1998;**80**:5027

[21] Lou S-y. Zeitschrift für Naturforschung. 1998;**53a**:251

[22] Belonenko MB, Demushkina EV, Lebedev NG. Journal of Russian Laser Research. 2006;**27**:457

[23] Belonenko MB, Lebedev NG, Popov AS. Pis'ma Zhurnal Eksperimental'noi i Teoreticheskoi Fiziki. 2010;**91**:506 [JETP Letters. 2010;**91**:461]

[24] Landau LD, Lifshitz EM. Field Theory [in Russian]. Moscow: Fizmatlit; 1988

[25] Landau LD, Lifshitz EM. Physical Kinetics [in Russian]. Moscow: Nauka; 1979

[26] Tans SJ, Devoret MH, Dai H, et al. Nature. 1997;**386**:474

[27] Manna MA, Merle V. Physical Review E. 1998;**57**:6206

[28] Hirota R. Direct Method in Soliton Theory. Cambridge, UK: Cambridge University Press; 2004

[29] Hirota R. Physical Review Letters. 1971;**27**:1192

[30] Hirota R, Satsuma J. Journal of the Physical Society of Japan. 1980;**40**:611

[31] Tang XY, Lou SY. Journal of Mathematical Physics. 2003;**44**:4000

[32] Kuetche VK, Bouetou TB, Kofane TC. Dynamics of miscellaneous fractal structures in higher-dimensional evolution model systems. In: Classification and Application of Fractals. New York: Nova Science Publishers; 2011

[33] Lou SY. Journal of Physics A: Mathematical and General. 2002;**35**: 10619

[34] Victor KK, Thomas BB, Kofane TC. Physical Review E. 2009;**79**:056605

[35] Kuetche VK, Bouetou TB, Kofane TC, Moubissi AB, Porsezian K. Physical Review E. 2010;**82**:053619

[36] Thomas BB, Victor KK, Crepin KT. Journal of Physics A: Mathematical and Theoretical. 2008;**41**:135208

[37] Kuetche VK, Bouetou TB, Kofane TC. Journal of Mathematical Physics. 2011;**52**:092903

[38] Noule RS, Kuetche VK. Compactons in carbon nanotube arrays. In: Advances in Nonlinear Dynamics Research. New-York: Nova Science Publishers; 2016

Edited by Sid-Ali Ouadfeul

The aim of this book is to show some applications of fractal analysis in the fields of sciences. The first chapter introduces the readers to the book, while the second chapter shows the methods and challenges of fractal analysis of time-series data sets. The third chapter demonstrates fractal geometry as an attractive choice for miniaturized planar microwave filter design. The fourth chapter presents fractal antennas for wearable applications. The objective of the fifth chapter is to show some Parrondian games in discrete dynamic systems, while the last chapter reveals fractal structures of carbon nanotube system arrays.

IntechOpen